AN ABSTRACT OF THE DISSERTATION OF

Lalita Attanatho for the degree of Doctor of Philosophy in Chemical Engineering presented on August 6, 2012

Title: Performances and Kinetic Studies of Hydrotreating of Bio-Oils in Microreactor

Abstract approved:

Goran N. Jovanovic

Hydrotreating reaction of vegetable oil is an alternative method for the production of renewable biodiesel fuel. This reaction involves conversion of triglycerides into normal alkanes, leads to a deoxygenated and stable product, which is fully compatible with petroleum derived diesel fuel. The hydrotreating process uses hydrogen to remove oxygen from triglyceride molecules at elevated temperature in the presence of a solid catalyst.

This work focused on the development of microtechnology-based chemical reaction process for liquid biofuel production from oil-based biofuel feedstock. A hydrotreating reaction of oleic acid and triolein as model compounds and jatropha oil as real feedstock was studied in a continuous flow microchannel reactor of inner diameter 500 μm and of varied length; 1.5 - 5 m. The microchannel reactor was fabricated from SS-316. The walls of the microreactor were coated with a thin Al_2O_3 film, which was then impregnated with Ni-Mo catalyst containing phosphorus as promoter. The reactions were carried out in the temperature range of 275-325 °C, residence time in the range of 11-40 s and at constant system pressure of 500 psig.

The results showed that the microchannel reactor was suitable for the hydrotreating process. Complete conversion of the fatty acid hydrotreating reaction was achieved at a reaction temperature of 325 °C. Hydrotreating of fatty acids occurred primarily via hydrodeoxygenation and the main liquid products were octadecane and heptadecane. Fatty alcohol, fatty acid and long chain esters were formed as reaction intermediates. Hydrotreating of triglycerides proceeded via the hydrocracking of triglycerides into diglycerides, monoglycerides and fatty acids. Then fatty acids were subsequently deoxygenated to hydrocarbons. The conversion of fatty acids and triglycerides increased with increasing temperatures.

A detailed mathematical model was developed to represent this two-phase chemical reaction process. The mathematical model was entirely based on first principles, i.e. no adjustable or correlation parameters were used. Kinetic parameter estimation was performed and the predicted results were in good agreement with experimental results.

Performances and Kinetic Studies of Hydrotreating of Bio-Oils in Microreactor

by
Lalita Attanatho

A DISSERTATION

Submitted to

Oregon State University

in partial fulfillment of
the requirements for the
degree of

Doctor of Philosophy

Presented August 6, 2012
Commencement June 2013

Doctor of Philosophy dissertation of Lalita Attanatho presented on August 6, 2012

APPROVED:

Major Professor, representing Chemical Engineering

Head of the School of Chemical, Biological and Environmental Engineering

---

Dean of the Graduate School

I understand that my dissertation will become part of the permanent collection of Oregon State University libraries. My signature below authorizes release of my dissertation to any reader upon request.

Lalita Attanatho, Author

ACKNOWLEDGEMENTS

I wish to thank all the people who have helped me during the course of this work.

First of all I would like to thank my major advisor, Dr. Goran Jovanovic, for his valuable help and guidance and for being very supportive.

I would like to extend my appreciation to Dr. Alexandre Yokochi, Dr. John Simonsen, Dr. Brian Paul and Dr. Enrique A. Thomann, for their time and commitment to serve in my academic graduate committee.

I also would like to acknowledge the Royal Thai Government for financial support and thank all the staffs at the Royal Thai Embassy in Washington DC for taking care of me during my stay in at OSU.

I wish to thank my fellow grad students in Dr. Jovanovic group for helping me during this work. Thank for sharing both joy and frustrations with me.

I would like to thank my family and friends for always supporting me throughout the years. Finally, I would like to dedicate this thesis to my parents, Weera and Jiraporn, for their love and support while I was far away from home during my Ph.D. program.

TABLE OF CONTENTS

Page

TABLE OF CONTENTS (Continued)

Page

TABLE OF CONTENTS (Continued)

Page

TABLE OF CONTENTS (Continued)

Page

LIST OF FIGURES

LIST OF FIGURES (Continued)

Figure Page

LIST OF FIGURES (Continued)

LIST OF FIGURES (Continued)

Figure Page

LIST OF FIGURES (Continued)

LIST OF FIGURES (Continued)

Figure Page

LIST OF TABLES

LIST OF TABLES (Continued)

Performances and Kinetic Studies of Hydrotreating of Bio-Oils in Microreactor

CHAPTER 1

INTRODUCTION

The depletion of global fossil fuels including increasing energy demand and concern over the deterioration of the environment due to excessive combustion of fossil fuel has motivated recent research, to focus on the production and utilization of renewable energy. Biofuel exist either as liquid or gaseous fuel produced from renewable sources. It is considered as a carbon-neutral energy source, because the overall amount of carbon dioxide in atmosphere is neither increased nor decreased by the combustion of biofuel. Biofuel can be produced by several methods depending on the types of feedstock and final products required [1].

1.1 Bio-oils

Oil-based feedstock or bio-oil is divided into four categories including edible oil (i.e. palm oil, soybean oil and sunflower oil), waste oil (i.e. waste cooking oil and trap grease), oil from algae and non-edible oil (i.e. jatropha oil, tung oil) [2]. Oil-based feedstock is common feedstock for the production of liquid biofuel because they consist primarily of triglycerides. Each triglyceride is composed of three long chain fatty acids attached to a glycerol backbone. The carbon chain length and number of double bonds in the fatty acids vary depending on the source of vegetable oil as shown in Table 1.1. Most of the oil-based feedstock generally consists of three main fatty acids: palmitic acid (C16:0), oleic acid (C18:1) and linoleic acid (C18:2). Palmitic acid is the common name for a straight-chained carboxylic acid containing sixteen carbon atoms. Oleic acid and linoleic acid are straight-chained carboxylic acids

containing eighteen carbon atoms with one and two carbon-carbon double bonds, respectively.

Triglycerides are easier to convert into liquid transportation fuels when compared to others biofuel feedstock, because they are high-energy liquids that contain less oxygen [3]. However, the use of edible oil feedstock, such as soybean oils, rapeseed oil and palm oil, for biofuel production has recently been of great concern due to the global conflict of interest between energy and food supply. Thus, the contribution of non-food oil such as oil from microalgae and jatropha oil will be significant as a source for biofuel production.

Table 1.1 Fatty acid compositions of vegetable oil (wt. %) [4], [5].

Crop oil	**Fatty acid (wt.%)**							
	C12:0	**C14:0**	**C16:0**	**C18:0**	**C18:1**	**C18:2**	**C18:3**	**C20:0**
Corn oil	-	-	12.2	2.2	27.5	57.0	0.9	0.1
Linseed oil	-	-	7.0	4.0	39.0	15.0	35.0	-
Peanut oil	-	0.1	11.6	3.1	46.5	31.4	-	1.5
Soybean oil	-	0.1	11.0	4.0	23.4	53.2	7.8	0.3
Sunflower oil	-	0.2	6.8	4.7	18.6	68.2	0.5	0.4
Rapeseed oil	-	0.1	5.1	2.1	57.9	24.7	7.9	0.2
Tung oil	-	-	5.5	0	4.2	8.5	82.0	-
Jatropha oil	-	-	12.5	7.5	42.1	37	-	-
Palm oil	0.35	0.92	44.11	4.36	38.97	11.21	-	0.09

Jatropha oil is one of the non-edible oil feedstock that has been recognized as a potential feedstock for biofuel production due to its high oil content and ability to be planted and grown in non-fertile or waste lands, with zero conflict to land use for food production [6]. It is a product of Jatropha curcas plant, which originated in Central

America. The current worldwide plantation for jatropha is about 1 million hectares but the plantation is expected to reach about 13 million hectares by 2015 worldwide. Jatropha oil production ranges from 300-1,200 gallons per acre [5]. The oil content in jatropha seed is reported to be in the range of 30 to 50% by weight of the seed and from 45 to 60% weight of the kernel itself [6]. Jatropha oil consists mainly of oleic acid and linoleic acid.

The overall concept of biofuel production from oil-based biofuel feedstock is shown in Figure 1.1. Plant oil and algae need water, sunlight and CO_2 for growing and producing lipids. After the oil extraction process, oil can be converted into renewable diesel by hydrotreating process. The hydrogen used in hydrotreating process can also be produced by the gasification reaction of solid biomass from the oil-extracting step. In addition, the use of concentrated solar radiation as the energy source for the high temperature thermo chemical process can eliminate the high energy consumption required in the conventional system. Thus, the hybrid solar and endothermic chemical reaction process will offer both viable and efficient routes for biofuel production system.

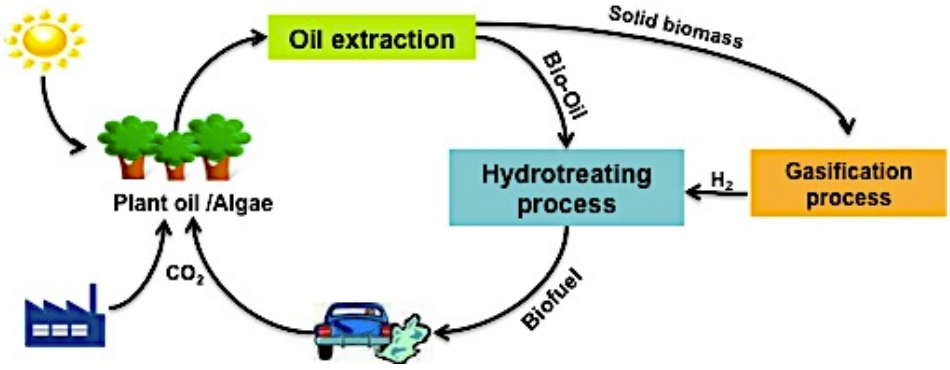

Figure 1.1 Concept of converting oil-based feedstock to biofuel.

1.2 Hydrotreating process of bio-oils

Current methods for producing biofuel from oil-based feedstock have been largely centered on biodiesel (fatty acid methyl esters) production by transesterification process [7], [8]. In 2005, microtechnology-based process for biodiesel production was successfully developed at Oregon State University [9]. Nevertheless, transesterification process does not produce biofuel identical to conventional diesel. There are some concern when using biodiesel such as instability, poor cold flow properties and high solvency leading to filter plugging problems [10]. Consequently, there is interest in the conversion of oil-based feedstock into a high quality biofuel that is fully compatible with petroleum diesel as an alternative process to transesterification.

Hydrotreating reaction of oil-based feedstock is an alternative method for producing renewable diesel. It involves the conversion of triglycerides into normal alkanes and leads to a deoxygenated and stable product that is fully compatible with petroleum derived diesel fuel. The hydrotreating process uses hydrogen to remove oxygen from triglyceride molecules at elevated temperature and pressure in the presence of a catalyst. The oxygen contained in the feed is removed as water [8], [10]. The chemical reaction of hydrogenation (full reduction) of a triglyceride to yield propane, water and long chain alkanes is illustrated below.

$$Triglyceride + 12H_2 \xrightarrow{catalyst} 3(n-alkanes) + 6H_2O + C_3H_8 \qquad (1.1)$$

The experimental results from literature [2] showed that not only a full reduction of triglyceride is possible but other reactions compete as well. The mechanism of the reaction for conversion of triglyceride into alkanes is complex and consists of series of consecutive steps. Various reaction pathways are taking place during the process including: hydrogenation, decarbonylation, decarboxylation, hydrodeoxygenation and hydrocracking as shown in Figure 1.2. The first step is hydrogenation, in which

hydrogen reacts with unsaturated fatty acid components in vegetable oil, and hydrocracking of triglyceride into various intermediates such as diglycerides, monoglycerides and carboxylic acids. These intermediates are then converted into normal alkanes by three different pathways: decarbonylation, decarboxylation, hydrodeoxygenation. The intermediates can form waxes if they are not converted into alkanes. These waxes can cause plugging problem in the reactor. Moreover, straight chain alkanes undergo isomerization and cracking to produce lighter and isomerized alkanes, respectively. If the straight chain alkanes are the desired product, the isomerization and cracking reaction should be minimized [2].

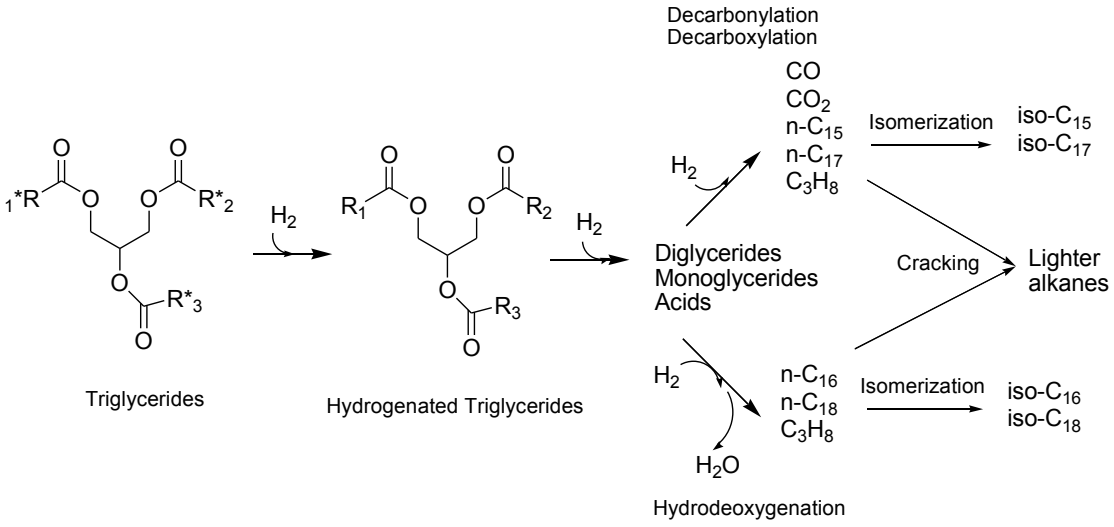

Figure 1.2 Scheme for hydrotreating of triglycerides [2].

Reactions for alkane production from carboxylic acid can be written as followed;

Decarbonylation reaction, involving the reaction with hydrogen to produce alkane, CO and water.

$$C_nH_{2n+1}COOH + H_2 \longrightarrow C_nH_{2n+2} + H_2O + CO \qquad (1.2)$$

Decarboxylation reaction, in which part of oxygen in vegetable oil is released in the form of CO_2

$$C_nH_{2n+1}COOH \longrightarrow C_nH_{2n+2} + CO_2 \quad (1.3)$$

Hydrodeoxygenation reaction involves the breakup of C-O bonds.

$$C_nH_{2n+1}COOH + 3H_2 \longrightarrow C_{n+1}H_{2n+4} + 2H_2O \quad (1.4)$$

In hydrogenation via hydrodeoxygenation, n-paraffins with an even number of carbon atoms, same as the fatty acids source in the vegetable oils, are formed. Mainly n-C16 and n-C18 are formed along with water and propane. In the case of hydrogenation via decarboxylation and decarbonylation, the products contain CO, H_2O, CO_2, propane and n-paraffins with an odd number of carbon atoms (mainly n-C15 and n-C17). The formation of CO and CO_2 lower by one the carbon atoms as compared to the source fatty acids in feedstock. The relative rate of the decarbonylation versus decarboxylation can be compared by the ratio of CO and CO_2 in gas product. The relative rate of decarbonylation and decarboxylation versus hydrodeoxygenation can be compared by the ratio of n-C17 and n-C18. The extent for each deoxygenation reaction depends on the catalyst and process conditions [11], [12].

Published literature shows that the temperatures required are in the range of 300-450 °C and pressure in the range of 10-110 bars in order to achieve the reasonable deoxygenation activity. Recently, considerable research has been done on the hydrotreating of fatty acids and various types of vegetable oils. The summary of recent studies on the hydrotreating of fatty acids and vegetable oils are shown in Table 1.2. The studies were carried out in a batch reactor, a tubular reactor and a fixed bed flow reactor and included the effect of different type of catalyst and operating conditions [11]-[23].

Table 1.2 Summary of recent studied on hydrotreating process of fatty acids and vegetable oils

Liquid Feed	Reactor	Catalyst	T (°C)	P (Bar)	LSHV (h^{-1})	Ref.
6.5 vol.% Rapeseed oil Sunflower oil Palm oil Lard in atmospheric gas oil	Tubular reactor	$NiMo/Al_2O_3$ $NiMo/TiO_2$ NiW/NaY NiW/TiO_2 NiW/ZrO_2	330-380	30-55	0.6-1	[11]
Rapeseed oil in light gas oil	-	$NiMo/Al_2O_3$	320-380	30-50	2	[13]
Waste cooking oil	Fixed bed reactor	-	330-398	82.7	1	[14]
Sunflower oil	-	$CoMo/Al_2O_3$	300-380	20-80	1-3	[15]
Oleic acid Canola oil	Tubular reactor	$Mo_2N/\gamma\text{-}Al_2O_3$ $WN/\gamma\text{-}Al_2O_3$ $VN/\gamma\text{-}Al_2O_3$	380-410	71.5-83	0.45	[16]
Refined rapeseed oil	Fixed bed reactor	CoMo/ MCM-41	300-320	20-110	1-4	[17]
0.15-0.6 mol/L Tall oil fatty acid in dodecane	Batch reactor	Pd/C	300-350	17	5-360 min[a]	[18]
5-100 wt.% Sunflower oil in heavy vacuum oil	Fixed bed reactor	$NiMo/Al_2O_3$	300-450	50	4.97	[19]
10 wt.% refined cotton oil in desulphurized diesel	Trickle-bed reactor	$CoMo/Al_2O_3$	305-345	30	WHSV = 5-25 h^{-1}	[20]
Stearic acid/ Tristearine +Dodecane	Parr autoclave (300 ml)	Pd/C	300-360	17-40	300-360 min[a]	[21]
Waste cooking oil	Batch reactor	Sulfated Zirconia	400-430	10-30	45-90 min[a]	[22]
Oleic acid and tripalmitin	Batch reactor	$Pt/\gamma\text{-}Al_2O_3$	325	20	5-20 h[a]	[23]

[a] Retention time for batch process

1.3 Microtechnology-based biofuel production

Hydrotreating reaction process of triglyceride is a gas-liquid-solid catalytic reaction. The overall rate of this chemical reaction depends on several parameters such as mass transfer rates by diffusion and convection, heat transfer and the intrinsic chemical reaction rate at catalyst surface. Several research works have been reported on hydrotreating of vegetable oil and model compounds in fixed bed, tubular and batch reactors but there is little information available on kinetic parameters of hydrotreating process of vegetable oil [12]-[17]. A kinetic model of hydrotreating of vegetable oils needs to be developed to find the optimal condition for efficient hydrotreating process.

Microtechnology offers substantially different approach in designing and performing all three aspects of the chemical reaction process outlined above. Since microtechnology and use of microreactors is relatively novel approach in chemical reaction technology, very little data exists on performance, benefits and disadvantages of microtechnology based biofuel production processes.

A micro-reactor is a small-scale reaction system fabricated by micro-technology and precision engineering. Small channels with dimensions ranging from ten microns to approximately 1 mm are the common design feature of the majority of micro-channel reactors. Microreactor offers several advantages when compared with any conventional macroscale reactor due to their small characteristic dimensions, resulting in high surface to volume ratios, which leads to the improvement of both heat and mass transfers [24], [25]. Consequently, microreactor is well suited for the hydrotreating process of vegetable oil. Performing hydrotreating of vegetable oil in microreactor will be able to eliminate mass transport limitations from the immiscibility of hydrogen gas and vegetable oil, making them an extremely useful tool for determining the intrinsic chemical reaction kinetics. Moreover, faster transfer of research results into commercial production is another prospected advantage of

performing the chemical reaction process in a microreactor. An increase in throughput of the microreactor can be easily achieved by a numbering-up approach, rather than by a scaling-up approach. Thus, identical quality products obtain from a microreactor could be increased by increasing the number of microreactors.

1.4 Research goal and objectives

The overall goal of this research is to develop a microtechnology-based chemical reaction process for liquid biofuel production from oil-based biofuel feedstock, which has potential for expanding to the industrial scale.

To control and improve this process, it is necessary to have a better understanding of mechanisms of transport and reaction processes that take place in microreactor. This knowledge will enable us to model mass transport and to predict the conversion of products in microreactors. Therefore, this work aims to explore two fundamental issues:

1. Intrinsic kinetics of hydrotreating reaction of oil
2. Reaction performance of oil hydrotreating process in microreactor

To achieve the research goal, the following objectives have to be accomplished.

1. Developing a mathematical model of oil hydrotreating
2. Preparing and depositing the catalyst in microchannel reactor
3. Investigating the effect of process parameters on the performance of microtechnology based chemical reaction process. Three different types of test will be performed: (1) model compounds test with oleic acid, (2) triolein and (3) jatropha oil
4. Determination of the intrinsic kinetics by analyzing the experimental data

1.5 Contribution to science

The present research focuses particularly on the experimental and theoretical characterization of biofuel feedstock chemical reaction process, which could be considered as the core of the future process for production of energy from biofuel feedstock. There are two contributions to science emerging from this work.

The first scientific contribution is to provide scientific data on the conversion of oil into liquid fuel as a result of hydrotreating process. Information on the conversion rate and kinetic data would be provided. The second scientific contribution is to provide new tool for scientific investigation, which is the mathematical model of the microreactor based chemical reaction process. The mathematical model developed in this work can be used as analytical and design tool for analyzing the experimental data and designing future chemical reaction processes for biofuel production.

1.6 Dissertation Overview

Chapter 1 describes the background, research goals and objectives, contribution to science and dissertation overview.

Chapter 2 provides a review of literature related to gas-liquid-solid reaction in microchannel, chemical kinetics of hydrotreating of vegetable oil and kinetic rate equation.

Chapter 3 focuses on the catalyst for hydrotreating process. It includes the literature review of hydrotreating catalysts, catalyst deactivation/regeneration and catalyst deposition in microchannel. The procedure for preparing and coating the catalyst in stainless steel substrate and microchannel are described.

Chapter 4 focuses on gas-liquid flow in microchannel reactor. Mathematical model for two-phase flow in microchannel and model validation with experimental data are

provided in this chapter. It also includes the detail of mathematical model for two-phase flow hydrotreating reaction in microchannel.

Chapter 5 presents the experimental apparatus and method for hydrotreating reaction.

Chapter 6 presents the experimental result and discussion for hydrotreating reaction of oleic acid, triolein and jatropha oil at various operating condition

Chapter 7 presents the conclusions of this research and recommendations for future studies

1.7 References

[1] Demirbas, A., 2007, Progress and recent trends in biofuels, Progress in Energy and Combustion Science, 33 (1), 1–18.

[2] Hubber, GW. and Corma, A., 2007, Synergies between bio- and oil refineries for the production of fuels from biomass, Angewandte Chemie International Edition, 46(38), 7184–210.

[3] Ong, Y.K. and Bhatia, S., 2010, The current status and perspectives of biofuel production via catalytic cracking of edible and non-edible oils, Energy, 35, 111–119.

[4] Attanatho, L., 2006, Oxidation stability of biodiesel from potential crops in Thailand, Third Biomass Asia Workshop.

[5] Li, L., Coppola, E., Rine J., Miller J. L. and Walker D., 2010, Catalytic hydrothermal conversion of triglyceride to non-ester biofuels, Energy & Fuels, 24, 1305-1315.

[6] Chhetri, A.B., Tango M. S., Budge S. M., Watts K.C. and Islam M.R., 2008, Non-Edible Plant Oils as New Sources for Biodiesel Production, Int. J. Mol. Sci., 9, 169-180.

[7] Sun, J., Ji, L., Zhang, L. and Xu, N., 2008, Synthesis of biodiesel in capillary microreactor, Ind. Eng. Chem. Res, 47, 1398-1403.

[8] Olusola, J.O., Adediran, M.M., Oluseyi, A.K. and Ajao, U.L., 2009, Processing of triglycerides to diesel range hydrocarbon fuels: easily practicable small-scale approach, Energy & Environment, 20(8), 1325-1341.

[9] Al-Dhubabian, Ahmad A., 2005, Production of biodiesel from soybean oil in a micro scale reactor, Master thesis. Chemcial engineering department. Oregon State University.

[10] Holmgren, J., Gosling, C., Marinangeli, R., Marker, T., Faraci, G. and Perego, C., 2007, New developments in renewable fuels offer more choices, Hydrocarbon processing, September, 67-71.

[11] Mikulec, J., Cvengros, J., Jorikova, L. and Kleinova, A., 2009, Production of diesel fuels from waste triacylglycerols by hydrodeoxygenation, 44th International petroleum conference, Bratislava, Slovak Republic, September 21-22.

[12] Donnis, B., Egeberg, R.G., Blom, P., Knudsen, K.G., 2009, Hydroprocessing of Bio-Oils and Oxygenates to Hydrocarbons. Understanding the Reaction Routes, Top Catal, 52, 229–240.

[13] Walendziewski, J.J., Stolarski, M., Luzny, R., Klimek, B., 2009, Hydroprocesssing of light gas oil-rape oil mixtures, Fuel Processing Technology, 90(5), 686–691.

[14] Bezergianni, S., Dimitriadis, A., Kalogianni, A. and Pilavachi, P.A., 2010, Hydrotreating of waste cooking oil for biodiesel production. Part I: Effect of temperature on product yields and heteroatom removal, Bioresource technology, 101, 6651-6656.

[15] Krar, M., Kovacs, S., Kallo, D. and Hancsok, J., 2010, Fuel propose hydrotreating of sunflower oil on CoMo/Al2O3 catalyst, Bioresource technology, 101, 9287-9293.

[16] Monnie, J., Sulimma, H., Dalai, A. and Caravaggio, G., 2010, Hydrodeoxygenation of oleic acid and canola oil over alumina-supported metal nitrides, Applied catalysis A:General, 382, 176-180.

[17] Kubicka, D., Bejblova, M. and Vlk, J., 2010, Conversion of vegetable oils into hydrocarbons over CoMo/MCM-41 catalysts, Top Catal, 53, 168-178.

[18] Rozmysłowicz, B., Maki-Arvela, P., Lestari, S., Simakova, O.A., Eranen, K., Simakova, I.L., Murzin, D.Y. and Salmi, T.O., 2010, Catalytic deoxygenation of tall oil fatty acids over a palladium-mesoporous carbon catalyst: a new source of biofuels, Top Catal, 53, 1274-1277.

[19] Hubber, G.W., Connor, P.O. and Corma, A., 2007, Processing in conventional oil refineries: Production of high quality diesel by hydrotreating vegetable oils in heavy vacuum oil mixtures, Applied catalysis A: General, 329, 120-129.

[20] Sebos, I., Matsoukas, A., Apostolopoulos, V. and Papayannakos, N., 2009, Catalytic hydroprocessing of cottoned oil in petroleum diesel mixtures for production of renewable diesel, Fuel, 88, 145-149.

[21] Kubickova, I., Snare, M., Eranen, K., Maki-Arvela, P. and Murzin, D.Y., 2005, Hydrocarbons for diesel fuel via decarboxylation of vegetable oils, Catalysis today, 106, 197-200.

[22] Charusiri, W. and Vitidsant, T., 2005, Kinetic study of used vegetable oil to liquid fuels over sulfated zirconia, Energy & Fuels, 19, 1783-1789.

[23] Madsen, A.D., Ahmed, E.D., Christensen, C.H., Fehrmann, R. and Riisager, A., 2011, Hydrodeoxygenation of waste fat for diesel production: Study on model feed with Pt/alumina catalyst, Fuel, 90 (11), 3433-3438.

[24] McGovern, S., Harish, G., Pai, C.S., Manfiels, W., Taylor, J.A., Pau, S. and Besser, R.S., 2009, Investigation of multiphase hydrogenation in catalyst-trap microreactor, J. Chem Technol Biotechnol, 84, 382-390.

[25] Taghavi-Moghadam, S., Kleemann, A., and Golbig, K.G., 2001, Microreaction Technology as a Novel Approach to Drug Design, Process Development and Reliability, Organic Process Research & Development, 5, 652-658.

CHAPTER 2

LITERATURE REVIEW

A literature review was carried out with the objective to study the various areas of interest that are influential to the hydrotreating of vegetable oil in a microchannel reactor. The review of gas-liquid multiphase reaction flow in a microchannel reactor was presented in the first section. The following is a review of previous work done on the topic of hydrotreating reaction mechanism, as well as the kinetic rate equation that was considered.

2.1 Literature review on gas-liquid multiphase reaction flow in microchannel reactors

2.1.1 Gas-liquid-solid catalytic reaction in microreactor

Microreactors are miniature reactors for carrying out chemical reactions, which have a channel diameter in the range of 10-1,000 μm. The main feature of microreactor is their high surface to volume ratio in the range of 10,000–50,000 m^2/m^3, while the specific surface in conventional macro scale reactor is typically in the range of 100-1,000 m^2/m^3. The high surface to volume ratio of a microreactor leads to the improvement of both heat and mass transfer compared to the conventional macro scale reactor [1].

Hydrotreating reactions are multiphase reactions that involve reactions of liquid phase reactants with hydrogen gas over a solid catalyst. These reactions are typically performed in batch and fixed bed reactors, which are operating under gas-liquid mass transfer limited conditions due to the immiscibility of hydrogen gas and vegetable oil. As microreactors offer high surface to volume ratio, the influence of transfer

phenomena on the overall reaction can be eliminated. The overall rate of reaction for gas-liquid-solid catalytic system depends on many parameters including mass transfer rates, due to diffusion and convection, and the intrinsic reaction rate at the catalyst surface. The external mass transfer limitation can be avoided resulting in highly efficient use of catalyst in the microreactor.

The effectiveness of gas and liquid phase mass transfer is a function of the gas-liquid interfacial area and the driving force for transport, both of which depend on the gas-liquid flow regimes. Two critical characteristics in evaluating the advantages and disadvantages of a particular flow regime are

- Good mass transport between gas and liquid, which depends on the driving force for mass transport and the gas-liquid interfacial area created.
- High liquid-solid interfacial area to effectively utilize the catalyst for rate of production.

The highest liquid-solid interfacial area will be achieved when liquid is the continuous phase.

2.1.2 Gas-liquid flow pattern in microchannel

The flow pattern of gas-liquid two-phase flow in microchannel depends on the fluid properties, the velocity and inlet geometry [2,3]. The original formation process of a bubble determines its geometric characteristics such as length and shape, and normally remains unchanged even far downstream at steady conditions. The consistent bubble geometry is a result of the bubbles tendency to avoid coalescing or breaking in the microchannel, which is contrary to macro scale equipment.

A variety of flow patterns such as bubble flow, slug flow and annular flow were reported and shown in Figure 2.1, where U_{GS} and U_{LS} are the gas and liquid superficial velocities, respectively [2]. Bubble flow is characterized by liquid as the continuous

phase, with bubbles of gas dispersed into a fully wetted channel. As the ratio of gas-to-liquid velocity increases, the Taylor flow regime (also referred as slug and segmented flow), where gas bubbles flow alternatively with liquid slugs, occurs in the channel. The relative lengths of each segment are constant for a given set of inlet conditions. As gas-to-liquid velocity further increases, annular flow occurs. In annular flow, gas is the continuous phase, and the liquid flows as a thin film along the channel walls.

Gas-liquid solid catalytic reactions are generally operated under slug flow regime because it provides the best gas-liquid mass transport due to recirculation within the liquid plugs and the reduction of axial mixing between liquid plugs [3]. The thin liquid film surrounding the gas bubble provides the short diffusion length for gas transfer to the catalytic wall.

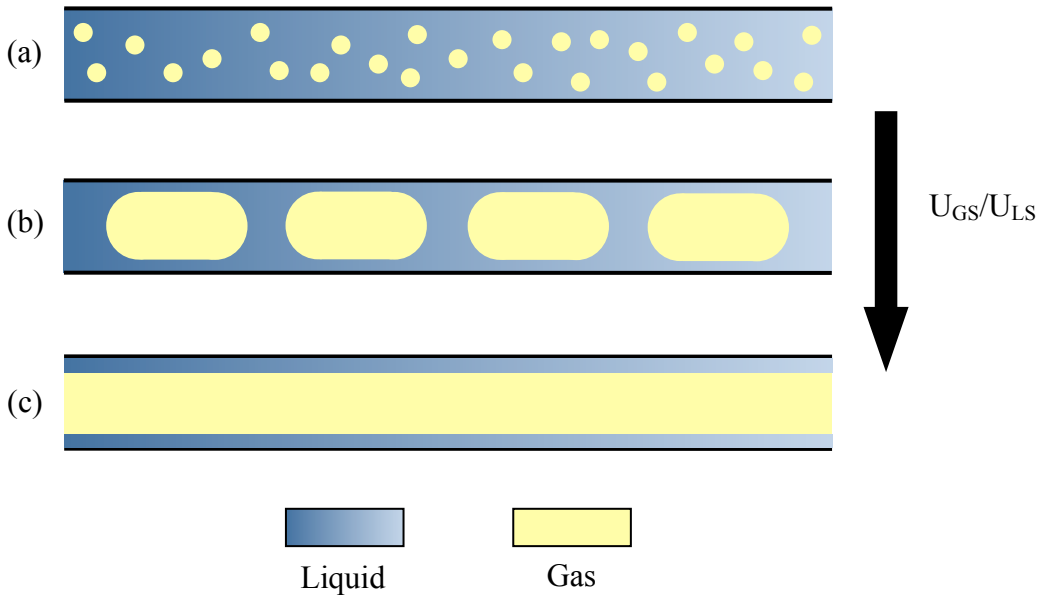

Figure 2.1 Illustration of gas-liquid flow regimes
(a) Bubble flow, (b) Slug flow and (c) Annular flow [2].

2.1.3 Bubble formation mechanism

Several inlet designs have been used to produce gas-liquid slug flow in microchannel and are reported in the literature [4, 5]. A T-mixer creates gas-liquid slug flow by introducing the gas into liquid flow at 90° angles with respect to the direction of liquid flow, whereas in Y-mixer, gas is introduced into liquid flow at non-90° angles with respect to the direction of liquid flow. In cross-flow mixer, gas-liquid slug flow is created by introducing two liquid streams into gas stream at an angle of 90° respect to the direction of gas flow. In co-flow mixer, gas stream is introduced through the microchannel in the same direction as the liquid stream [4, 5].

Single bubble formation from gas nozzle surrounded by flowing liquid has been studied both experimentally and theoretically. Most theoretical works are based on a balance of forces acting on the spherical bubble. Two sets of forces, namely detaching force (positive force) and attaching forces (negative force) were identified. Factor affecting bubble formation as proposed by the literatures includes buoyancy force, surface tension force at nozzle, gas momentum flux, bubble inertia and liquid drag force [6].

Various bubble formation models have been developed and bubble volume was defined. In the single stage model [7], the detaching force was considered to be in a continuous balance with the attaching force. Bhunia et al. [8] used two-stage model to describe the bubble formation from a single nozzle in a co-flowing fluid configuration. The bubble formation consists of two stages, the expansion stage and detachment stage. During the expansion stage, the bubble grows spherically due to the incoming gas flux but the bubble remains attached to the nozzle. During the detachment stage, additional gas is fed into the bubble that continues to grow in size and then bubble lift off and form a neck connecting them to the nozzle tip. The neck pinches off and the bubble detaches at the end of the detachment stage.

Bubble volume can be calculated by equating the detaching and attaching forces. However, models based on force balance cannot predict gas bubble size in microchannels accurately. The bubbles deform significantly as they grow and approach the channel wall, deviating from the spherical shape assumed by most force balance models.

The effect of inlet condition on slug flow was studied by Amador et al. [9]. Bubble formed at T- and Y- junction and co-flow configurations with various gas/liquid inlet dimensions were found to depend significantly on the ratio of gas to liquid superficial velocities and gas inlet diameter for any given geometry. All the investigations reported that the bubble volume decreased with an increase of superficial liquid velocity [4].

2.1.4 Bubble and liquid slug length

Correlations based on both experimental data and numerical simulations on the bubble and liquid slug length have been reported in the literature and lists in Table 2.1. These correlations show the dependence of bubble and slug sizes on operating conditions and fluid properties.

Laborie et al. [10] correlated experimental bubble and slug length in 1-4 mm capillaries. In this correlation, important physical parameters such as the inertial force, viscosity force and gravity force play significant roles. However, the geometry of gas inlet has not been considered. Kreutzer [11] suggested the correlation for slug length in square channel. Akbar et al. [12] used the volume of fluid method to predict the liquid slug length in circular capillaries and included the gas holdup term to the correlation. The results agree well with experimental data obtained in Laborie et al. Qian and Lawal [5] proposed the correlations for liquid slug length and gas bubble length as a function of Re, Ca and phase holdup. They found significant dependence

Table 2.1 Literature correlations on bubble and liquid slug length under slug flow.

Gas-Liquid inlet	Main channel dimension (mm)	Superficial velocity (m/s)	Correlation	Reference
T-junction	1	U_{GS} = 0.01-0.25 U_{LS} = 0.01-0.25	$\frac{L_s}{d} = 1.637\,\varepsilon^{-0.893}(1-\varepsilon)^{-0.05}Re^{-0.075}Ca^{-0.0687}$ $\frac{L_g}{d} = 1.637\,\varepsilon^{0.107}(1-\varepsilon)^{-1.05}Re^{-0.075}Ca^{-0.0687}$ $Re = \frac{\rho_{lig} u_{TP} d}{\mu_{liq}}$ $\varepsilon = \frac{u_{gas}}{u_{gas}+\mu_{liq}}$	[5]
Porous membrane	1-4	U_{GS} = 0.1-0.74 U_{LS} = 0.1-1	$\frac{L_B}{d_c} = 0.0878\frac{\mathrm{Re}_B^{0.63}}{Eo^{1.26}}$, $\mathrm{Re}_B = \frac{\rho_L U_B d_c}{\mu_L}$, $Eo = \frac{(\rho_L-\rho_G)d_c^2 g}{\sigma}$ $\frac{L_S}{d_c} = 3451\left(\frac{1}{\mathrm{Re}'_G\, Eo}\right)^{1.27}$, $\mathrm{Re}'_G = \frac{\rho_L U_{GS} d_c}{\mu_L}$	[10]
Liquid distributor	1.56	$U_{GS} + U_{LS} < 0.75$	$\frac{L_S}{d_c} = \frac{\varepsilon_L}{-0.00141 - 1.55\,\varepsilon_L^2 \ln(\varepsilon_L)}$, $\varepsilon_L = \frac{U_{LS}}{U_{GS}+U_{LS}}$	[11]
N/A	0.1-1	$0.5 < U_{GS} + U_{LS} < 1.6$	$\frac{U_{TP}^{-0.33}}{\sqrt{L_S}} = 142.6\,\varepsilon_G^{0.56}\left(\frac{d_c}{L_{UC}}\right)^{0.42}\mathrm{Re}_G^{-0.252}$, $\varepsilon_G = \frac{U_{GS}}{U_B}$	[12]

of bubble and slug lengths on the inlet geometry. By varying T-junction orientation and size of inlet channels as well as the degree of premixing of the two fluids in their numerical simulations, the slug length was found to vary up to 300% under the same operating conditions.

2.1.5 Liquid film thickness

In gas-liquid slug flow, the bubble is separated from the wall by a thin liquid film. The circulating vortex in liquid slug is not in direct contact with the wall and mass can only be transferred to the wall by diffusion through the film. Thus the thickness of this liquid film is needed to model the mass transfer in the system.

Bretherton [13] analytically derived an expression for the liquid film thickness in channel with a circular cross-section as a function of capillary number. He used the lubrication theory for the transition region where the film is formed, i.e., between the spherical front of bubble and the flat film far behind the front.

The front of bubble may be regarded as spherical with radius, r, so the Laplace pressure difference across the gas-liquid interface is given by $\Delta p = 2\gamma / r$ provided the film thickness is small, $\delta << r$. In the region of constant film thickness, the curvature in the axial direction vanishes, and the Laplace pressure difference is given by $\Delta p = \gamma / r$. A balance of the viscous force and the pressure gradient in the transition region yields

$$\frac{\mu u}{\delta^2} \approx \frac{1}{\lambda}\frac{\gamma}{r} \qquad (2.1)$$

Where λ is the length of the transitional region between the spherical and flat surface. The length λ is unknown, but it can be estimate by requiring that the Laplace pressure is continuous at the interface or in the other words, that the curvature at the end of the transition region.

$$-\frac{\gamma}{r}-\frac{\gamma\delta}{\lambda^2}\approx\frac{-2\gamma}{r} \tag{2.2}$$

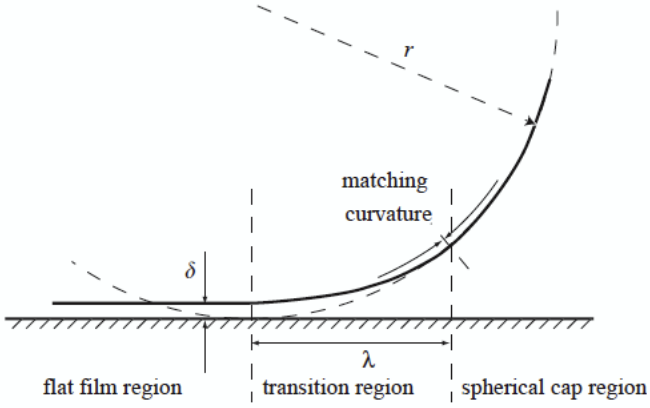

Fig. 2.2 Schematic representation of the transition region between the flat film and the spherical front of the bubble [3].

Thus we have $\lambda\approx\sqrt{\delta r}$, from which the classical Bretherton law can be deduced:

$$\frac{\delta}{r}\approx Ca^{2/3} \tag{2.3}$$

Where Ca is capillary number, $Ca=\frac{\mu U_b}{\sigma}$. The more rigorous analysis of the full Navier-Stokes equations in the transition region at the front and back of the bubble by Bretherton results in

$$\frac{\delta}{r}=1.34\left(Ca\right)^{2/3} \tag{2.4}$$

Which is valid in the range of δ below 0.04r and in the absence of significant inertial and gravitational force. For round capillaries, numerous experimental correlations of the film thickness are available and all these correlations give the same order of magnitude for the film thickness. Fairbrother and Stubbs [14] measured the film thickness by direct measurement of velocity difference between the gas bubble and the

liquid, assuming that the film was at rest. They fitted their experimental data into equation.

$$\frac{\delta}{r} = 0.5(Ca)^{1/2} \tag{2.5}$$

Other experimental methods for measuring liquid film thickness are based on spectrometric method with a photocell as described by Irandoust and Andersson [15]. The basic principle of the film-thickness measurements lies in comparing the extent of light absorption in the liquid slug with that of bubbles at a selected wavelength. Hence, the liquid phase was colored with a suitable color substance in such a way that the flow pattern was not disturbed. The fraction of light intensity detected by the photodiode was proportional to the thickness of the liquid layer and the concentration of the absorbing substance in the solution. The film thickness was fitted to the empirical formula

$$\frac{\delta}{r} = 0.36\left(1 - \exp(-3.1Ca^{0.54})\right) \tag{2.6}$$

Aussilous and Quere [16] have applied the scaling analysis to Bretherton's result for the liquid film thickness. They fitted the result of their scaling analysis to Taylor's data [17] for round capillaries to obtain:

$$\frac{\delta}{r} = \left[\frac{1.34Ca^{2/3}}{1+3.33Ca^{2/3}}\right] \tag{2.7}$$

The result from Aussilous and Quere's correlation is consistent with Bretherton's result, since this equation approaches Bretherton's equation for Ca approaches 0. The experimentally correlations for the liquid film thickness are summarized in Table 2.2.

Table 2.2 Liquid film thickness correlation

Dimensionless liquid film thickness, δ/r	Range of Ca	Reference
$1.34(Ca)^{2/3}$	$10^{-3} \le Ca \le 10^{-2}$	[13]
$0.5(Ca)^{1/2}$	$5x10^{-5} \le Ca \le 3x10^{-1}$	[14]
$0.36(1-\exp(-3.1Ca^{0.54}))$	$9.5x10^{-4} \le Ca \le 1.9$	[15]
$\left[\frac{1.34Ca^{2/3}}{1+3.33Ca^{2/3}}\right]$	$10^{-3} \le Ca \le 1$	[16]

2.1.6 Mass transfer

Gas to liquid mass transfer is often the rate-determining step for the reaction in slug flow system. Assuming the gas side mass transfer resistance is negligible. Three mass transfer steps for gas component mass transfer to catalyst wall are:

(1) Gas transfer from bubble to liquid slug

(2) The transfer of dissolved gas from liquid slug to catalyst

(3) Mass transfer from gas bubble through the liquid film to catalyst

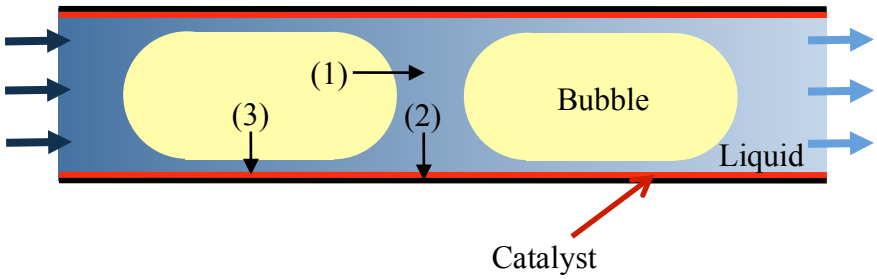

Figure 2.3 Mass transfers in gas-liquid slug flow system.

Important parameters influencing the mass transfer for gas-liquid slug flow are the length of the gas bubble, length of liquid slug and the film thickness. For a given liquid hold-up, slug flow with short liquid slugs will have a higher mass transfer rate than flow in which larger liquid slugs occurs. This is caused by the increased interfacial area and the more intense mixing for short liquid slugs [3].

2.2 Literature review on kinetics of hydrotreating reaction

Reaction mechanism and reaction kinetics are necessary for any reactor design, process development and process optimization. Reaction mechanism is the understanding of the reaction on the molecular level. Reaction kinetics is the translation of the understanding of the chemical processes into a mathematical expression that can be used to predict the extent of the reaction at any time under particular conditions.

2.2.1 Reaction mechanism

Several chemical reaction mechanisms for hydrotreating reaction of vegetable oil and model compound were purposed in the literatures [18-21]. The mechanism of hydrotreating reaction for conversion of triglyceride, which is the main components of vegetable oils, into alkanes is complex and consists of series of consecutive steps as proposed by Huber et al. [18]. Various reaction pathways are taking place during the process including: hydrogenation, decarbonylation, decarboxylation, hydrodeoxygenation and hydrocracking as shown in Figure 2.4.

The first step is hydrogenation, in which hydrogen reacts with unsaturated fatty acid components in vegetable oil, and hydrocracking of triglyceride into various intermediates such as monoglycerides, diglycerides and carboxylic acids. These intermediates are then converted into normal alkanes by three different pathways: decarbonylation, decarboxylation, hydrodeoxygenation.

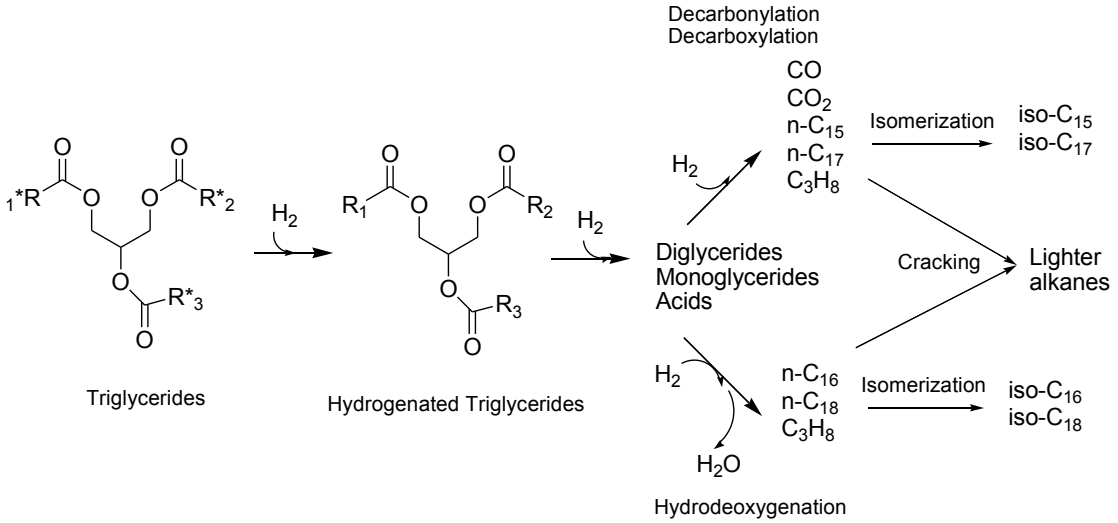

Figure 2.4 Reaction pathways for hydrotreating of triglycerides [18].

The intermediates can form waxes if they are not converted into alkanes. These waxes can cause plugging problem in the reactor. Moreover, straight chain alkanes undergo isomerization and cracking to produce lighter and isomerized alkanes, respectively. If the straight chain alkanes are the desired product, the isomerization and cracking reaction should be minimized. In addition, the three-carbon backbone in the process to produce alkanes yields propane [18]. Reaction of alkane production from stearic acid and tristearin as model compounds representing triglycerides and fatty acids can be written as followed; [22]

Decarbonylation reaction and Decarboxylation reaction

$$CH_3-(CH_2)_{16}-COOH \longrightarrow CH_3-(CH_2)_{15}-CH_3+CO_2$$

$$\Delta G_{573} = -83.5 \quad KJ/mol \qquad (2.8)$$

$$CH_3-(CH_2)_{16}-COOH \longrightarrow CH_3-(CH_2)_{14}-CH=CH_2+CO+H_2O$$

$$\Delta G_{573} = -17.0 \quad KJ/mol \qquad (2.9)$$

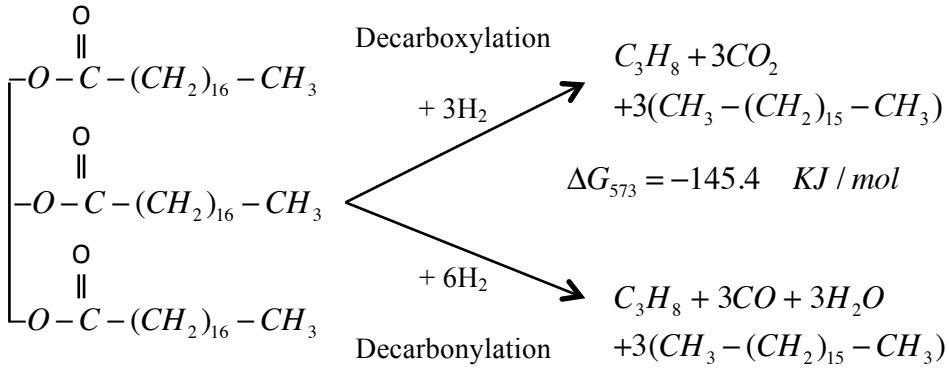

$$C_3H_8 + 3CO_2 \quad +3(CH_3-(CH_2)_{15}-CH_3) \qquad \Delta G_{573} = -145.4 \quad KJ/mol$$

$$C_3H_8 + 3CO + 3H_2O \quad +3(CH_3-(CH_2)_{15}-CH_3) \qquad \Delta G_{573} = -99.9 \quad KJ/mol \quad (2.10)$$

Hydrodeoxygenation reaction

$$CH_3-(CH_2)_{16}-COOH + 3H_2 \longrightarrow CH_3-(CH_2)_{16}-CH_3 + 2H_2O$$

$$\Delta G_{573} = -86.1 \quad KJ/mol \quad (2.11)$$

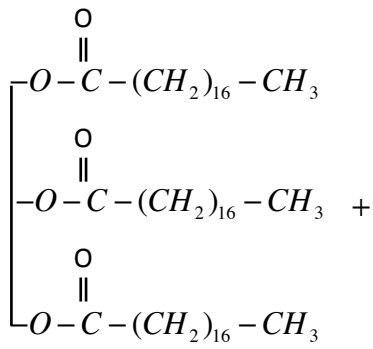

$$+12H_2 \longrightarrow C_3H_8 + 6H_2O + 3(CH_3-(CH_2)_{16}-CH_3)$$

$$\Delta G_{573} = -17.0 \quad KJ/mol \quad (2.12)$$

In hydrogenation-hydrodeoxygenation, n-paraffins with an even number of carbon atoms corresponding to related fatty acids in the vegetable oils, mainly n-C16 and n-C18 are formed along with water and propane. In case of hydrogenation-decarboxylation, the products comprise of CO_2, propane and n-paraffins with an odd number of carbon atoms in molecules (mainly n-C15 and n-C17), usually lower by one than that in the carbon atoms corresponding to related fatty acids in feedstock. The

relative rate of the decarbonylation versus decarboxylation can be compared by the ratio of CO and CO_2 in gas product. The relative rate of decarbonylation and decarboxylation versus hydrodeoxygenation can be compared by the ratio of n-C17 and n-C18. The extent for each deoxygenates reaction depends on the catalyst and process conditions [18, 19].

Kubicka et al. [19] have reported evidence of fatty acid, fatty alcohol and long chain ester generation as the intermediates during the vegetable oil hydrotreating over three sulfide catalysts, namely Ni/Al_2O_3, Mo/Al_2O_3 and $NiMo/Al_2O_3$. They proposed the reaction pathway of triglyceride transformation into hydrocarbons from the experimental data of vegetable oil and the scheme is schematically illustrated in Figure 2.5. The double bonds in triglycerides are at first saturated. Then they are converted into fatty acids by hydrogenolysis of the C–O bond between the fatty acid chain and the propane (glycerol) backbone of triglycerides. Fatty acid can either (i) undergo further hydrogenation steps to yield fatty alcohols and ultimately saturated n-alkanes with an even carbon atoms number (hydrodeoxygenation) or (ii) undergo decarboxylation to yield hydrocarbons directly, i.e. hydrocarbons with an odd number of carbon atoms (hydrodecarboxylation).

The simultaneous presence of both fatty acids and alcohols leads to formation of fatty esters from esterification reaction of fatty acids with fatty alcohols. These esters are, nevertheless, subsequently converted into hydrocarbons. Hydrodeoxygenation leads to elimination of water from triglycerides, fatty acids, fatty alcohols and fatty esters as a result of reaction with hydrogen. It has been proposed that this reaction occurs via adsorbed enol intermediate [23]. Hydrodecarboxylation consists of decarboxylation (CO_2 elimination) of compounds containing carboxylic functional group and hydrogenation of the unsaturated intermediates of CO_2 elimination. CO_2 is a primary product of this reaction and it may undergo further reactions, particularly hydrogenation, which is undesired since it causes significant increase in hydrogen consumption.

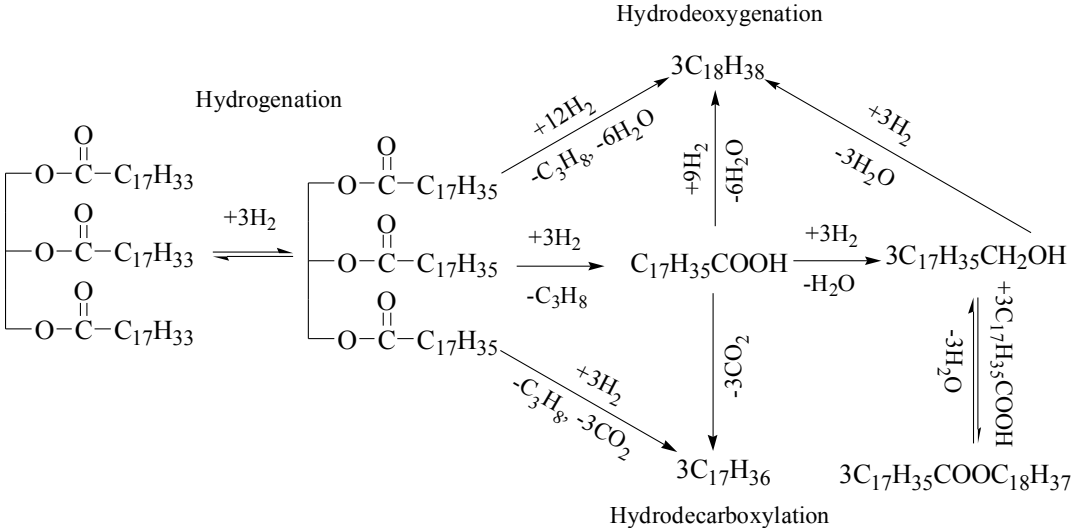

Figure 2.5 Reaction pathways for hydrotreating of triglycerides with fatty acid, fatty alcohol and long chain ester intermediates [19].

The reaction mechanism for the deoxygenation of oleic acid over Pd/C catalyst was proposed by Snare et al. [20] and presented in Figure 2.6. Oleic acid is either direct deoxygenation to olefins or reacted via hydrogenation of double bonds and further through deoxygenation of stearic acid. Positional and geometrical isomerization of oleic acid, e.g. to elaidic and vaccenic acid seems to be the intermediate reactions prior to the hydrogenation step. Thereafter the deoxygenation reaction is taking place and the main deoxygenation product is n-heptadecane.

Boda et al. [21] studied catalytic hydrotreating of triglycerides for biofuel production by using tricaprylin and caprylic acid as model compounds. The hydrotreating reaction of tricaprylin was found to proceed in consecutive steps: hydrogenolysis of tricaprylin to caprylic acid and propane, followed by hydrodeoxygenation of the caprylic acid intermediate. The overall reaction rate was governed by the rate of the hydrodeoxygenation reaction that is the rate-determining step. Thus, in the process of tricaprylin conversion to hydrocarbons, the caprylic acid is an intermediate that, as a

consequence of the slow hydrodeoxygenation reaction, has a high steady-state concentration in the product mixture. The catalytic hydrodeoxygenation of carboxylic acids was modeled by the hydrodeoxygenation of caprylic acid. Liquid product contained mainly octane (n-C8) over the commercial NiMo/γ-Al_2O_3 catalyst, whereas over the Pd/C catalyst heptane (n-C7) was the major product. Two distinct hydrodeoxygenation routes were distinguished: (1) hydrodecabonylation and (2) reduction of oxygen.

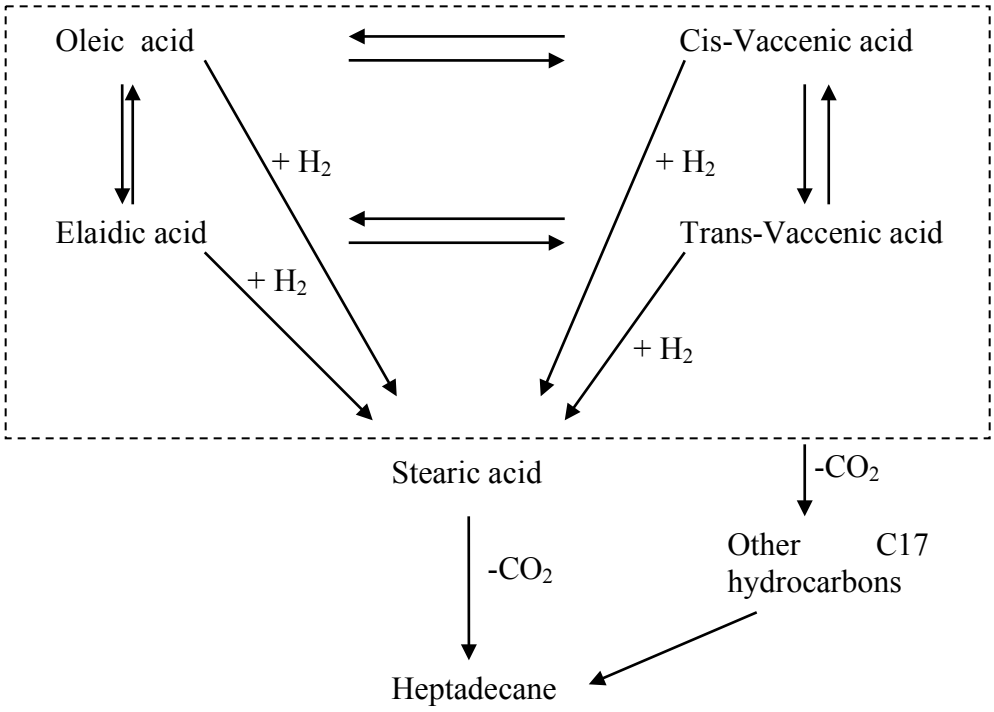

Figure 2.6 Reaction scheme of oleic acid deoxygenation by Snare et al. [20].

Hydrogenolysis

$$TG + 3H_2 \longrightarrow 3(R - CH_2 - COOH) + C_3H_8$$

Hydrodeoxygenation

$$R - CH_2 - COOH + H_2 \longrightarrow R - CH_2 - CHO + H_2O$$

$$\left[R - CH_2 - CHO \longleftrightarrow R - CH = CH - OH\right]$$

$$+H_2 \qquad +H_2\ ,\ -H_2O$$

$$R - CH_2 - CH_2 - OH \xrightarrow{H_2O} R - CH = CH_2$$

$$R - CH = CH_2 \xrightarrow{H_2} R - CH_2 - CH_3$$

Figure 2.7 Reaction mechanism of triglyceride hydrotreating reaction proposed by Boda et al. [21].

2.2.2 Reaction kinetics

Despite the enormous amount of literature on triglyceride hydrotreating reaction, only a few studies deal with the kinetics of this reaction. Detailed kinetic studies of triglyceride, fatty acid and their derivatives hydrotreating reaction to obtain kinetic parameters such as activation energies, reaction orders and rate constants have been reported in the literature. Langmuir-Hinshelwood kinetic expression was used by Boda et al. [21] to explain the effect of pressure on the hydrodeoxygenation of fatty acid when the adsorption and reactions of fatty acids with surface hydrogen determine the kinetic rates.

$$r = \frac{k K_{H_2} p_{H_2} K_{acid} C_{acid}}{(1 + K_{H_2} p_{H_2} + K_{acid} C_{acid})^2} \tag{2.13}$$

Where k is the reaction rate constant and K_{H2} and K_{acid} are the equilibrium adsorption coefficients of H_2 and fatty acid respectively. However, they did not determine the reaction rate constant for this system.

Snare et al. [24] studied the kinetics of ethyl stearate decarboxylation and the decarboxylation of the stearic acid reaction intermediate over a 5%Pd/C catalyst in semi-batch reactor. A kinetic model was developed based on a proposed reaction network and the assumption of a Langmuir–Hinshelwood-type mechanism.

$$r_i = \frac{(k_i K_j) C_j}{1 + \sum_{j=1}^{n} K_j C_j} \tag{2.14}$$

The adsorption steps were assumed to be rapid compared to surface reactions. Thus, surface reactions were assumed to be rate-determining step. The adsorption constant for gaseous products was disregarded in the denominator. Their results showed that the equilibrium constants could be neglected and the denominator is equal to 1. Thus the kinetic model was reduced to first order reaction and it was found to show good agreement with the experimental data.

In general, the use of Langmuir-Hinshelwood type of rate equation for representing the hydrotreating kinetics is complicated, and there are too many coefficients that are difficult to determine [25]. So, the power law model is often use by most researchers to fit kinetic data and to obtain kinetic parameters. However, it should be noted that the power law model is not reliable to predict the system out of the range of studied experimental conditions.

Kinetic parameters for methyl stearate deoxygenation on alumina-supported Pt catalyst in semi-batch reactor were estimated using a general power law rate expression [26].

$$Rate = -\frac{dC_{ms}}{dt} = ke^{-E/RT}C_{ms}^{n} \tag{2.15}$$

Where k is the rate constant, C_{ms} the concentration of methyl stearate, and n the reaction order. The experimental data at temperature in the range of 573-623 K and at constant system pressure of 0.69 MPa were fitted simultaneously, using common kinetic parameters. The rate constant k resulting from the fit is 2.08×10^4 1/s. The activation energy, based on this rate expression, was 106.53 kJ/mol. The order of the reaction obtained in the fitting is 0.31.

Sebos et al. [27] examined the kinetics of the hydrodeoxygenation of triglyceride. The kinetics described in their work is the overall kinetics and not an intrinsic kinetics. The relative change of the saponification number between feedstock and product stream was used as a measure of the conversion of the ester group containing material that comes from triglycerides of the feedstock and can also be mono- and di-ester in the partly converted oils. It was assumed that the hydrodeoxygenation of the ester groups is a first-order reaction, proportional to the concentration of the ester content of the feedstock.

$$-r_{HDO} = k_{HDO}C_{est,0}(1-x) \tag{2.16}$$

$$k_{HDO} = -\ln(1-x)\cdot \dot{m} / m_{cat} \tag{2.17}$$

Where $-r_{HDO}$ is the rate of hydrodeoxygenation, k_{HDO} the reaction rate constant, $C_{est,0}$ the ester group content of the feedstock, m the mass feed rate and m_{cat} the catalyst mass.

Kumar et al. [28] studied the hydrotreating reaction of jatropha oil over NiMo catalyst at different reaction temperatures. They evaluated the rate of disappearance of triglycerides by using the pseudo-first order kinetics to fit the relevant experimental data. The rate constants k_{HDO} resulting from the fit are 1.23 and 4.22 1/s at 300 and 325 °C respectively. The activation energy, based on this rate expression, was 132.3 kJ/mol.

Most of the kinetic studies published to date have been performed in batch or semi-batch reactors. Given that the separation of reaction kinetics and catalyst deactivation is challenging when a batch reactor is employed. The results of these studies should be approached with some caution and the need for detailed kinetic work involving the use of continuous reactors is indicated.

2.3 References

[1] Kiwi-Minsker, L. and Renken, A., 2005, Microstructured reacors for catalytic reactions, Catalysis today, 110, 2-14.

[2] McGovern, S., Harish, G., Pai, C.S., Manfiels, W., Taylor, J.A., Pau, S. and. Besser, R.S., 2009, Investigation of multiphase hydrogenation in catalyst-trap microreactor. J. Chem Technol Biotechnol, 84, 382-390.

[3] Kreutzer, M.T., Kapteijn, F., Moulijin, J.A. and Heiszwolf, J.J., 2005, Multiphase monolith reactors: Chemical reaction engineering of segmented flow in microchannels, Chemical Engineering Science, 60, 5895-5916.

[4] Shao, N., Salman W., Gavriilidis, A., Angeli, P, 2008, CFD simulations of the effect of inlet conditions on Taylor flow formation, International Journal of Heat and Fluid Flow, 29, 1603-1611.

[5] Qian, D. and Lawal, A., 2006, Numerical study on gas and liquid slugs for Taylor flow in a T-junction microchannel, Chem. Eng. Sci., 61, 7609-7625.

[6] Nahra, H.K. and Kamotani, Y., 2000, Bubble formation from wall orifice in liquid cross-flow under low gravity, Chemical Engineering Science, 55, 4653-4665.

[7] Walters, J.K., Davidson, J.F., 1963, The initial motion of a gas formed in an invisid liquid, Part 2. The three-dimensional bubble and totoidal bubble, Fluid Mech, 17, 321-226.

[8] Bhunia, A., Paris, S.C., Kamotami, Y. and Kim, L.H., 1998, Bubble formation in a coflow configuration in normal and reduced gravity, AIChE J., 44, 1495-1509.

[9] Amador, C., Salman, W., Sanguanpiyaporn, S., Gavriilidis, A., Angeli, P., 2004, Effect of gas inlet conditions on the mechanism of Taylor flow formation, ICMF04, Report SP-515, Yokohama.

[10] Laborie, S., Cabassud, C., Durand-Bourlier, L. and Laine, J.M., 1999, Chaacterization of gas-liquid two-phase flow inside capillaries. Chem. Eng. Sci., 54 (23), 5723-5735.

[11] Kreutzer, M., 2003, Hydrodynamics of Taylor flow in capillaries and monolith reactors, Delft University Press, Delft.

[12] Akbar, M.K., Ghiaasiaan, S.M., 2006, Simulation of Taylor flow in capillaries based on the volume-of-fluid technique, Ind. Eng. Chem. Res, 45, 5396-5403.

[13] Bretherton, F.P., 1961, The motion of long bubbles in tubes, Journal of Fluid Mechanics, 10, 166–188.

[14] Fairbrother, F., and Stubbs, A.E., 1935, Studies in electro-endosmosis. Part VI. The bubble tube method of measurement, Journal of the Chemical Society1, 527-529.

[15] Irandoust, S., Andersson, B., 1989, Liquid film in Taylor flow through acapillary. Industrial and Engineering Chemistry Research, 28, 1684–1688.

[16] Aussillous, P. and Quere, D., 2000, Quick deposition of a fluid on the wall of a tube, Physics of Fluids, 12 (10), 2367-2371.

[17] Taylor, G., 1961, Deposition of a viscous fluid on the wall of a tube, J. Fluid Mech., 10, 161-196.

[18] Hubber G. W., Connor P. O and Corma A., 2007, Processing in conventional oil refineries: Production of high quality diesel by hydrotreating vegetable oils in heavy vacuum oil mixtures, Applied catalysis A: General, 329, 120-129.

[19] Kubicka D., Bejblova M. and Vlk J., 2010, Conversion of vegetable oils into hydrocarbons over CoMo/MCM-41 catalysts, Top Catal, 53, 168-178.

[20] Snare, M., Kubickova, I., Maki-Arvela, P., Chichova, D., Eranen, K., Murzin, D.Y., 2008, Catalytic deoxygenation of unsaturated renewable feedstocks for production of diesel fuel hydrocarbons, Fuel, 87, 933-945.

[21] Boda, L., Onyestyak, G., Solt, H., Lonyi, F., Valyon, J., and Thernesz, A., 2010, Catalytic hydroconversion of tricaprylin and caprylic acid as model reaction for biofuel production from triglycerides, Applied Catalysis A: General, 374, 158-169.

[22] Santillan-Jimenez, E., Crocker, M., 2012, Catalytic deoxygenation of fatty acids and derivatives to hydrocarbon fuels via decarboxylation/decarbonylation, J Chem Technol Biotechnol,

[23] Donnis B., Egeberg R.G., Blom P., Knudsen K.G., 2009, Hydroprocessing of Bio-Oils and Oxygenates to Hydrocarbons. Understanding the Reaction Routes, Top Catal, 52, 229–240.

[24] Snare, M., Kubickova, I., Maki-Arvela, P., Eranen, K., Warna, J., Murzin, D.Y., 2007, Production of diesel fuel from renewable feeds: Kinetics of ethyl stearate decarboxylation, Chemical Engineering Journal, 134, 29-34.

[25] Whitehurst, D. D., Takaaki, I. and Mochida, I., 1998, Present State of the Art and Future Challenges in the Hydrodesulfurization of Polyaromatic Sulfur Compounds, Adv. Catal, 42, 344.

[26] Do, P.T., Chiapperp, M., Lobban, L.L. and Resasco, D.E., 2009, Catalytic deoxygenation of Methyl-Octanoate and Methyl-Stearate on Pt/Al2O3, Catal Lett, 130, 9-18.

[27] Sebos, i., Matsoukas, A., Apostolopoulos, V., and Papayannakos, N., 2009, Catalytic hydroprocessing of cottonseed oil in petroleum diesel mixtures for production of renewable diesel, Fuel, 88, 145-149.

[28] Kumar, R., Rana, B.S., Tiwari, r., Verma, D., 2010, Hydroprocessing of jatropha oil and its mixtures with gas oil, Green Chemistry, 12, 2232-2239.

CHAPTER 3

HYDROTREATING CATALYST AND CATALYST DEPOSITION IN MICROCHANNEL

This chapter focuses on the catalysts used for hydrotreating process. It begins with a literature review of hydrotreating catalysts, catalyst deactivation/regeneration and catalyst deposition in microchannel. The knowledge gained from the literature review is used in the experiment for catalyst preparation and deposition in stainless steel microchannel, which is then presented in the last section of this chapter.

3.1 Catalyst for hydrotreating process

A catalyst is a substance that enhances the rate of a chemical reaction without being consumed by the reaction. A catalyst accelerates a chemical reaction by forming bonds with the reacting molecules (i.e. adsorption) that can react to a product. The product then detaches itself from the catalyst (i.e. desorption), and leaves the catalyst unaltered so that it is ready to interact with the next set of molecules. The catalytic reaction can be described as a cyclic event in which the catalyst participates and is recovered in its original form at the end of the cycle. A catalyst cannot alter the chemical equilibrium of a given reaction, but it only creates a favorable reaction pathway. This is done by decreasing the activation barrier and thus increasing the reaction rate. Furthermore, if for a certain reaction different paths are possible that lead to various products, the catalyst can selectively decrease the activation energy of one of the possible reaction paths, thus altering the selectivity of the reaction [1]. This can be seen in the graph contained in Figure 3.1.

Conventional hydrotreating catalyst, the sulfide form of $NiMo/Al_2O_3$ and $CoMo/Al_2O_3$, are usually used in vegetable oil hydrotreating studies [2,3]. Molybdenum (Mo) is considered to be the active ingredient, whereas nickel (Ni) and

cobalt (Co) are viewed as either promoters or active sites. Alumina oxide (Al_2O_3) is generally used as a catalyst support because of its high surface area and thermal stability [4]. The high hydrogenation activity and mild acidity make this catalyst appropriate for a hydrotreating reaction of vegetable oil. Using a sulfide catalyst for the hydrotreating reaction resulted in an excellent product yield. However, the sulfide catalyst introduces sulfur into the process, which is not a desirable compound in vegetable oils.

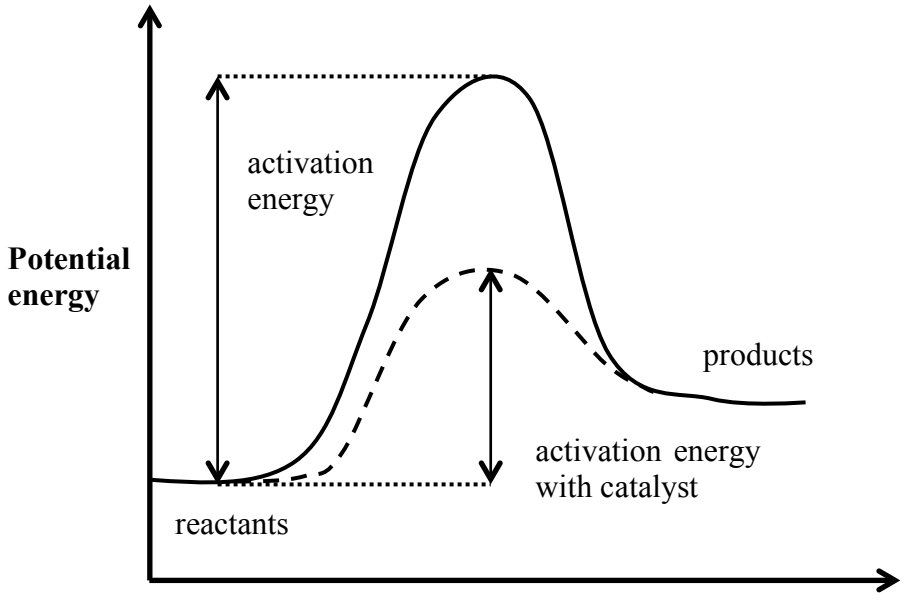

Figure 3.1 Potential energy graph for a catalytic reaction (dashed line) compared with a non-catalytic reaction (solid line). The presence of a catalyst lowers the activation energy.

The use of non-sulfide catalysts for the hydrotreating of fossil fuels has been studied [5,6]. It has been shown that non-sulfide catalysts can be successful in removing many impurities such as oxygen, sulfur, and nitrogen. The various catalysts that have been studied include $NiMo/Al_2O_3$ and $CoMo/Al_2O_3$ and other supported transition metal catalysts. Noble metal catalysts such as Ru, Pd, and Pt on activated carbon have been

tested for vegetable oil hydrotreating reactions. The non-sulfide catalysts in general showed similar or better performance than the conventional hydrotreating catalysts [6].

Numerous modifiers have been studied and special attention given to the influence of phosphorous, mainly on NiMo catalysts. The phosphorous addition to $NiMo/Al_2O_3$ sulfide catalysts is known to promote both hydrodesulfurization and hydrodenitrogenation in conventional hydrotreating processes. In addition, these catalysts are less susceptible to coking [7]. It has been demonstrated that phosphorus produces several positive effects including the modification of dispersion of the metal salt on the support and modification of acid sites [8, 9]. Phosphorous alters the acid strength distribution on alumina and improves thermal stability of alumina oxide with respect to sintering and phase transformation. Thus, it simplifies the preparation of the catalyst and extends its lifetime through an improvement of the mechanical and thermal properties. It also improves stability and increases metal solubility in impregnation solutions, which enables the preparation of catalysts with high Ni–Mo contents in just one impregnation step.

3.2 Catalyst deactivation and regeneration

Generally, catalyst deactivation may be caused by an aging phenomenon such as gradual change in surface crystal structure, or by the deposit of a foreign material on active portions of the catalyst surface. This is called poisoning or fouling of the catalyst [1]. The presence of coke deposits and poisons in the feedstock mainly deactivate the hydrotreating catalysts. Coke formation considerably reduces catalyst pore size and efficiency and the catalyst appears to become inactive after some time on stream.

Gevert and Ottersted found a rapid deactivation of NiMo and CoMo catalysts during the first hours of operation, but this became steady at prolonged reaction times [10]. The extent of coking is a function of the feed and processing conditions, and also the

structure and support of the catalyst [11, 12]. Usually, the loss of activity due to the blocking of active centers or pores by carbonaceous deposits is partially reversible [13, 14].

The soluble coke can be removed from the catalyst surface by solvent extraction using n-hexane, toluene and methylene chloride. The insoluble coke can be removed by burning off the deposits in an oxygen-rich stream. Coke removal via oxidation is highly exothermic and can easily result in overheating and thermal reorganization of the sample. This results in the loss of the catalyst surface area (sintering). Thus, it is necessary to avoid excessive temperature rises that may damage the catalyst. Brito et al., regenerated the spent $NiMo/Al_2O_3$ catalyst with 0.9-8% carbons by burning off coke deposits in 5-12 vol.% O_2 in N_2 stream at high temperature, in the range of 395-513 °C [14].

3.3 Alumina based catalyst deposition in microchannel

Microchannel reactors are commonly used for heterogeneous catalytic reactions. In coating the catalyst onto the inside walls of microchannel, it is important to obtain the following properties;

- Uniform thickness
- High surface area
- Good adhesion
- Good dispersion of active phase
- Long-term stability.

The deposition of a uniform thickness, good adhesion and good mechanical stability catalyst coating layer on the microchannel wall are important. This is a result of the detachment of small particles that can easily lead to blocking due to the small dimensions of the microchannels.

From the literature survey conducted, it was found that the most prominent way for coating alumina-based catalyst on the inner wall pre-assembled microchannel is the

washcoat route followed by impregnation. Sol-gel process is the main coating synthesis procedure in the washcoat route. Impregnation is often used to deposit a catalytic active phase on the catalysts support from washcoat route and it does not differ from powder impregnation. Apart from the coating process, the pretreatment of substrate to coat is also important because it allows increasing the adherence of the catalyst layer. Thermal treatment is often used as pretreatment step for metallic substrate. The details of substrate pretreatment, coating of support on pre-assembled microchannel and deposition of active phase on the support are presented in the following section.

3.3.1 Pretreatment of metallic substrate by thermal oxidation

Pretreatment of metallic substrate prior to coating have been shown to be important to produce well-adhered coatings. In most of the studies, aluminum containing metallic substrates has been used in order to take advantage of the formation of an Al_2O_3 layer on the surface of the substrate. A porous Al_2O_3 layer enhances the washcoat adhesion on microchannels mainly due to the segregation of a whisker-like alumina layer after thermal treatment at high temperature [15].

The coating of substrate with a composition lacking in aluminum is challenging because it is not possible to segregate an alumina layer to improve adherence. Cebollada et al. [16] studied the effect of thermal pretreatment of stainless steel substrate, which mainly consists of Fe, Ni and Cr. The thermal pre-treatment of this substrate at 800 °C for 2 h creates a surface with a grainy morphology and higher roughness than the original substrate, which is beneficial for the adhesion of the alumina coating. The formation of this morphology is due to the segregation of silica and chromium oxides to the surface, which was confirmed by scanning electron microscopy with energy-dispersive analysis of X-ray (SEM-EDX).

3.3.2 Alumina coating method

Three main coating methods for depositing alumina support material layer on the microchannel surfaces are sol–gel deposition, suspension deposition and hybrid method [17]. Table 3.1 shows the summary of recent works of support and catalyst deposition on various substrates.

Sol–gel deposition

Sol-gel process is the most frequently used method for depositing alumina support on the substrate. The starting reagent of alumina sol can be aluminum alkoxides or aluminum inorganic salt [18]. The hydroxyl groups on the colloid particles induce an increasing number of cross-links between the particles, resulting in the formation of a gel. The aging of the sols, the viscosity and the thermal treatment are the parameters governing sol-gel process. The ageing time, allowing the gelation (peptisation) of the sol can vary from a few minutes to several weeks, depending on the concentrations in the sol, degree of branching and the characteristic size of the object to coat. The wet gel films are converted into porous oxides by drying, followed by a heat treatment procedure [19]. Sol with high viscosities obtained after long ageing times, allow the depositing of a thicker layer but are exposed to cracks. The sol-gel method can produce layers up to 10 μm thick.

Alumina sol was usually prepared by the Yoldas process by hydrolyzing aluminum isopropoxide (Al $(OC_3H_7)_3$) in deionized water at 80–92 °C. Hydrogen chloride (HCl) or acetic acid (CH_3COOH) was used as a peptizing agent in the Yoldas process. Typically, a molar ratio of water, alkoxide and acetic acid was 100:1:0.15. In peptization, the transparency of a sol increased with an increase in a molar ratio of acetic acid up to about 0.15 and the transparency gradually decreased above a molar ratio of 0.15 [18]. Polyvinyl alcohol (PVA) was normally added as a drying control

chemical to reduce crack formation of the alumina layer and improve adhesion between the alumina layer and the substrate during drying and calcination processes.

The drying and calcination conditions used in the coating method can influence the coating properties, such as in the formation of cracks. Fei et al. [20], dip-coated Fecralloy rods in alumina sol, and dried the coatings at room temperature for 1 h, then in an oven at 100 °C for 2 h before finally calcining in a furnace at 500 °C for 3 h. They found that thicker coatings were achieved by dip coating several times, and that drying and calcining each layer separately could avoid cracks caused by large stresses.

Suspension deposition

The ready to use, commercially available catalyst can be directly deposited inside a microchannel utilizing a suspension method. The standard ingredients include powder (catalyst support or catalyst itself), binder, acid and water (or another solvent) [17]. The concentration of all ingredients depends on the nature of the surface being coated and on the desired layer thickness. The suspension method is capable of producing a thicker layer than sol gel method.

Hybrid method between sol-gel and suspension

A hybrid method between suspension and sol-gel can be used to prepare the support for a catalyst layer on the substrate. This method does not differ much from the suspension method. A sol acts as the binder but also participates in the chemical and textural properties of the final deposited layer. The wallcoat of non-porous pre-assembled microchannels with alumina based sol-gel catalyst slurry was studied by Bravo et al. [26]. They proved the viability of thick (up to 25 μm) wall coating of an alumina based sol–gel catalyst slurry within cylindrical geometries, and showed that there was sufficient adhesion on the non-porous surfaces.

Table 3.1 Summary of recent works of support and catalyst deposition on various substrates.

Deposition method	Coating technique	Deposited support or catalyst	Material of the structure	Channel size	Thickness of catalyst carrier	Reference
Sol-gel	A	Al_2O_3	Stainless steel microchannel platelets	-	1.1-3.5 **µ**m	[4]
Sol-gel*	B	Ni/Al_2O_3	Stainless steel microchannel platelets	285 **µ**m H x 430 **µ**m W	4.8-29.5 **µ**m	[16]
Sol-gel	A	Al_2O_3	Magnesium alloy AZ31 plate	20 mm x 20 mm x2 mm	30 **µ**m	[21]
Slurry*	-	Pt/Al_2O_3, Rh/Al_2O_3	Stainless steel microchannel platelets	250 **µ**m H x 500 **µ**m W	-	[22]
Slurry*	-	CuO/ZnO/ Al_2O_3	Stainless steel microchannel platelets	400 **µ**m H x 600 **µ**m W Platelets: 50×50×1 mm	24-40 **µ**m	[23]
Slurry	-	Ni/Al_2O_3	Stainless steel microchannel platelets	300 **µ**m H x 400 **µ**m W x 50 mm L Platelets:99.5×28×2 mm	25 **µ**m	[24]

A= Dip coating, B = Two-step, gas-assisted fluid displacement method,

C = Fill-and-dry coating method, * = Deposition method after thermal treatment process

Table 3.1 Summary of recent works of support and catalyst deposition on various substrates (continue).

Deposition method	Coating technique	Deposited support or catalyst	Material of the structure	Channel size	Thickness of catalyst carrier	Reference
Slurry	-	Al_2O_3	Stainless steel microchannel platelets	400 μm H x 500 μm W x 20 mm L	-	[25]
Hybrid	-	CuO/ZnO/ Al_2O_3	Quartz and fused silica capillaries	0.2-4 mm i.d. X 30 cm L	1-25 um	[26]
Hybrid	-	CuO/ZnO/ Al_2O_3	Stainless steel microchannel platelets	200 μm H x 300 μm W	-	[27]
Hybrid	A	CuO/ZnO/ Al_2O_3	Fused silica capillaries	530 μm diameter capillaries	75 μm	[28]
Slurry and hybrid	C	Cu/ZnO/ Al_2O_3	Silicon based microchannel	240 μm H x 600 μm W x 37.5 cm L	10-20 μm	[29]

A= Dip coating, B = Two-step, gas-assisted fluid displacement method,

C = Fill-and-dry coating method, * = Deposition method after thermal treatment process

3.3.3 Alumina coating technique

Wall coating of alumina can be done through a number of techniques including dip coating, spin coating and gas-assisted fluid displacement, as shown in Figure 3.2. The limitation of dip and spin coating is that these techniques can only be implemented on flat substrates prior to reactor assembly. For pre-assembled microchannel, two different approaches have been used for coating alumina on the support, flow coating and fill-and-dry coating. In the case of flow coating, microchannels were filled with the alumina slurry/sol, the excess solution was then removed by using an air flowing method. When gas displaces the liquid from the capillary, a layer of liquid is left on the capillary wall, and a continuous column of gas is formed extending from the inlet to the advancing gas/liquid interface. The coated microchannels were then dried and calcined. In the fill-and-dry coating technique, the microchannels filled with the catalyst slurry underwent drying and calcination without removing excess slurry by flowing air. It was reported that the fluid rheology, residence time and airflow rate during flow coating influenced the alumina layer thickness [17, 29].

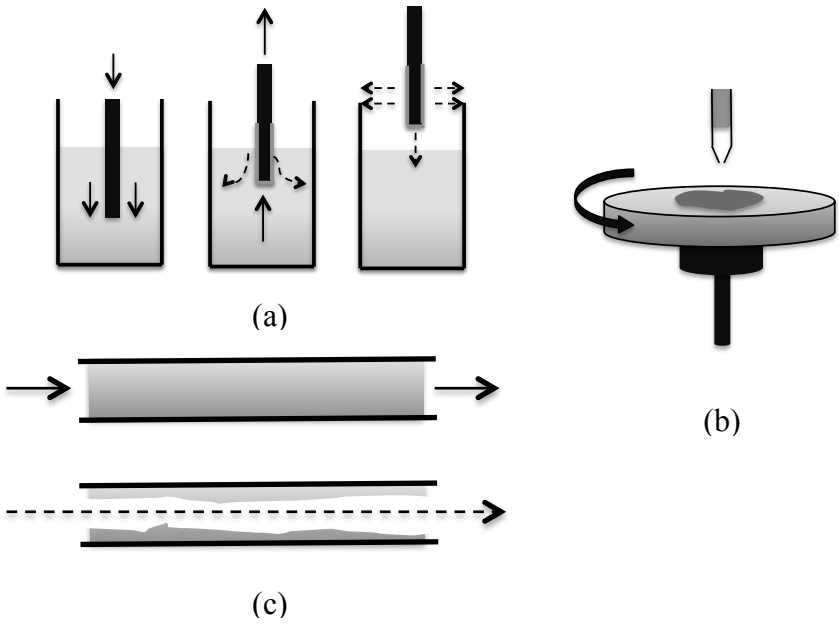

Figure 3.2 Coating technique. (a) dip coating, (b) spin coating and (c) gas-assisted fluid displacement.

3.3.4 Catalyst impregnation

Impregnation is the procedure in which the catalyst support is contacted with a solution containing a precursor of active phase in water or organic solvents. Generally, there are two different methods of impregnation: wet and dry methods. In wet impregnation, an excess of precursor solution is used. This is the simplest impregnation method, but it can result in the deposition of high amounts of the precursor material at the exterior parts of the support bodies during drying resulting in heterogeneous distribution of the active component. Nevertheless such a distribution may be beneficial, since it alleviates the need of reactant penetration deep inside the catalyst bodies. Another type of impregnation is dry impregnation; the amount of precursor solution added to the support material equals or is slightly less than the pore volume [30]. After impregnation, the support is removed from the solution and the excess solvent is eliminated by drying. As a result, the precursor of the active phase adheres to the surface of the support as shown in Figure 3.3.

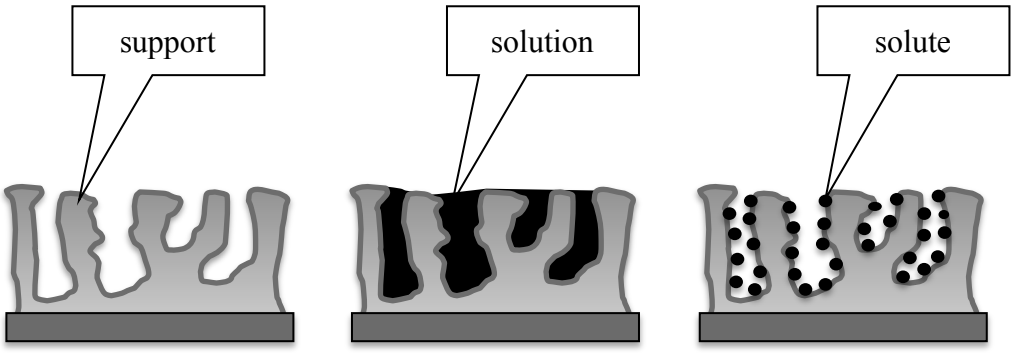

Figure 3.3 Catalyst impregnation.

The term co-impregnation is used when several precursors are present simultaneously in the impregnation solution. Generally, four steps occur during the impregnation process:

1. Transport of solute to the outer support surface

2. Transport of solute to the pore system of support
3. Diffusion of solute within the pore system
4. Uptake of solute by the pore wall

The conditions during drying can influence the distribution of the precursor compound over the support material. This change in distribution is caused by solvents flowing inside the pores of the support material during drying. As a result of these flows, the precursor material is entrained through the pores, which can lead to inhomogeneous distributions after drying. To prevent the redistribution of the precursor materials during drying, careful control of the drying rate of the impregnated bodies must be taken. Cervello et al. [31] investigated the impregnation of gamma alumina pellets with nickel solution. It was observed that short contacts time renders uniform or eggshell catalyst, while longer soaking time increases the surface concentration of the adsorbed nickel and produces a more uniform catalyst distribution. Fierro et al. [32] analyzed several Mo-profiles obtained either at shorter or longer impregnation times. It was concluded that irrespective of the initial solution concentration, the Mo-profiles almost leveled off at the longer impregnation time. Whereas a shorter soaking time resulted in profiles that decreased towards the interior of the pellet.

The procedure for preparing NiMo catalyst on alumina support by impregnation method was reported in the literature. Liu et al. [33] prepared NiMo on Al_2O_3 support (surface area 180 m^2/g) by incipient wetness impregnation of the Al_2O_3 support with aqueous solutions of molybdenum trioxide and nickel nitrate at room temperature. After an overnight drying at room temperature, the sample was further dried at 393 K for 12 h in air and then was calcined at 673 K for 2 h. The results demonstrate the inferior catalyst structure caused by this impregnation method. The catalyst prepared was partially comprised of aggregated crystals.

$NiMoP/Al_2O_3$ catalyst was prepared by Ferdous et al. using incipient wetness co-impregnation method. In this method, a solution containing ammonium

heptamolybdate [$(NH_4)_6Mo_7O_{24}\cdot 4H_2O$], nickel nitrate [Ni $(NO_3)_2\cdot 6H_2O$] and phosphoric acid (H_3PO_4) in water was impregnated onto an Al_2O_3 support. The pH of the solution was maintained at 3.5 using 28 wt.% concentrated NH_3 solution. Impregnation of the support was followed by drying for 12 h at 120 ˚C and calcination at 500 ˚C for 4 h [7].

In NiMoP impregnation solution, interactions between nickel cations and molybdenum containing anions yield insoluble compounds, such as molybdates. Phosphoric acid is added to the impregnation solution as a stabilizer in order to prevent the formation of a precipitate. Compounds with quite diverse structures can form in the solution, depending on the preparation conditions, components concentrations, and the molybdenum to phosphorus ratio. Interaction between ammonium paramolybdate and H_3PO_4 in the impregnating solution prepared by Klimov et al. [34] yields the $[P_2Mo_5O_{23}]^{6-}$ anion. The diphosphopentamolybdate ion has the shape of a planar ring formed by five MoO_6 octahedral linked together by five oxygen bridges and by two PO_4 groups, one over and the other under the ring plane.

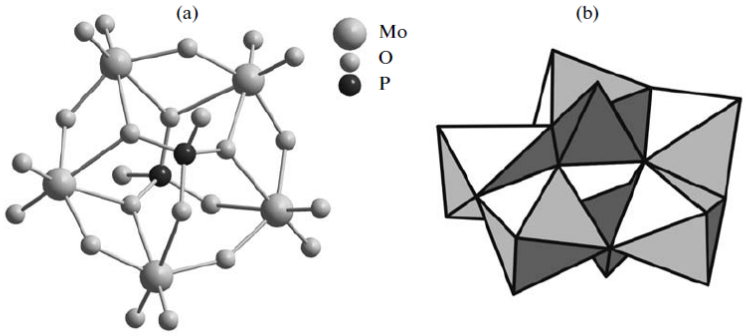

Figure 3.4 Structure of $[P^2Mo^5O^{23}]^{6-}$ anion: (a) atomic model and (b) model as octahedral and tetrahedral [34].

The solutions used in the preparation of catalysts that contained high molybdenum and nickel concentrations, can yield an undesired crystalline precipitate upon long storage time. This can be prevented by introducing carbamide as a stabilizer into the solution. Carbamide forms well with soluble complexes and also with other components of the

solution. Carbamide is coordinated to Ni ions through its nitrogen atoms. This compound consists of the $[P^2Mo^5O^{23}]^{6-}$ anion coordinated via its terminal oxygen atoms to outer oxygen atoms of the PO_4 moieties to Ni^{2+} ions stabilized in the solution by carbamide [34].

3.3.5 Coating adherence

Coating adherence is how strong the washcoat is attached to the substrate. It has been mainly based on the mass loss from sonication tests that involves the soaking of coating in the solvent under sonication. Petroleum ether, a non-polar solvent that contains mostly pentane, is usually used as a solvent and acts by weakening the attractive bonds in the coatings [16]. The treated sample is then dried and the mass loss is evaluated. Thermal shock and scratch test had been used for assessing coating adherence by Zhao et al. [35] and Germani et al. [23] respectively.

3.4 Experimental study on $NiMoP/Al_2O_3$ catalyst deposition on stainless steel microchannel

In this study, $NiMoP/Al_2O_3$ catalyst was prepared and deposited on a stainless steel coupon and inside the stainless steel microtube by sol–gel process of alumina support, followed by impregnation of the active metal. The 316 Stainless steel coupons with dimensions of 0.5 x 0.5 in, 2 x 2 in and microtubes with inner diameters of 500 micron and 50 cm long were chosen to model microreactor channels in coating experiments. Figure 3.5 shows the flow chart for the preparation and characterization of catalyst coating on the stainless steel substrate.

3.4.1 Substrate pretreatment

Experimental

Stainless steel coupons were submerged in a 1wt.% solution of alconox detergent for cleaning for 1 h. The coupons were rinsed by running deionized water, cleaned with

ethanol and then dried in an oven at 80 °C for 2 h. Thermal treatment was used to modify stainless steel surface to enhance coating adhesion by heating the coupon under static air. The effects of treatment temperatures were studied by heating the stainless steel coupon at 500 and 700 °C for 2 and 5 h, respectively. Optical microscope (DM LM, Leica Microsystems, Germany) and scanning electron microscopy (FEI Quanta 600F, FEI, U.S.A.) were used to study surface morphology of the pretreated substrate. Surface roughness of the substrate was obtained using an optical surface profiler (Optical Profiler ZeScope, Zemetrics, U.S.A.). Elemental composition of the substrate was determined by Energy-dispersive analysis of X-ray (EDX).

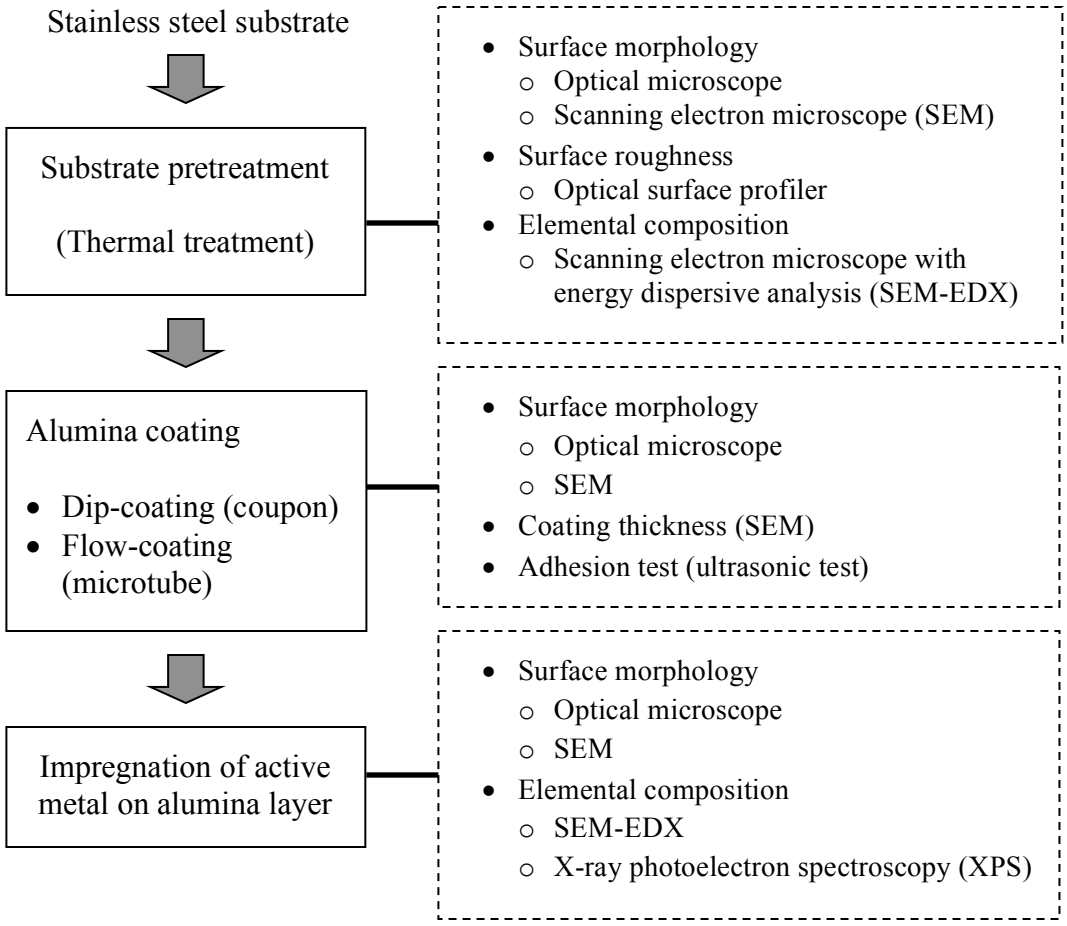

Figure 3.5 Flow chart for preparation and characterization of catalyst coating on stainless steel substrate.

Result and Discussion

The optical and SEM image of stainless steel substrate before and after thermal treatment are shown in Figure 3.6. It was observed that the untreated coupon has a plain surface while the heat-treated coupon has red and dark spots on the surface due to the formation of metal oxides. The surface became darker and the grainy structure increased as the thermal treatment temperature increased. The specific mass gain after thermal treatment process at 700 °C for 5 h was 0.035 mg/cm^2.

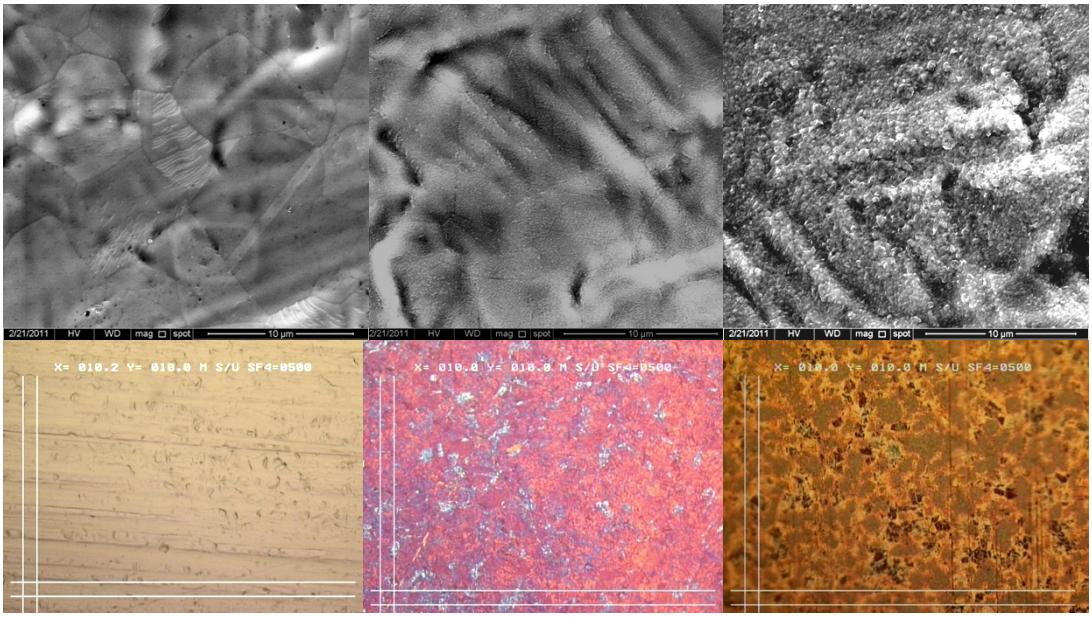

(a) **(b)** **(c)**

Figure 3.6 Optical and SEM image of (a) untreated stainless steel coupon, (b) after thermal treatment at 500 °C, 2 h and (c) after thermal treatment at 700 °C, 2 h.

The composition of stainless steel substrates were determined by SEM-EDX and it mainly consists of Fe, Cr and Ni as shown in Table 3.2. Figure 3.7 shows the EDX spectrum of untreated stainless steel and heat treated stainless steel at 700 °C for 5 h. After thermal treatment at 500 and 700 °C, higher oxygen content was detected on the surface. This result was consistent with Cebollada et al. [16], which reported the

increase of oxygen content in stainless steel substrate after thermal treatment. The presence of oxygen is related to the formation of metal oxides on the surface that helps to increase the adhesion of alumina layer.

Table 3.2 Elemental composition of stainless steel coupon surfaces by EDX.

Element	Untreated Stainless steel (wt. %)	Heat-treated Stainless steel (wt. %)		
		500 °C (2 h)	700 °C (2 h)	700 °C (5 h)
O	2.39	3.56	9.70	12.23
Si	0.68	0.78	0.65	0.73
Mo	2.48	2.28	1.96	2.24
Cr	16.96	16.84	15.68	15.50
Mn	1.64	1.61	1.15	1.33
Fe	65.99	65.23	61.70	59.36
Ni	9.86	9.70	9.16	8.60

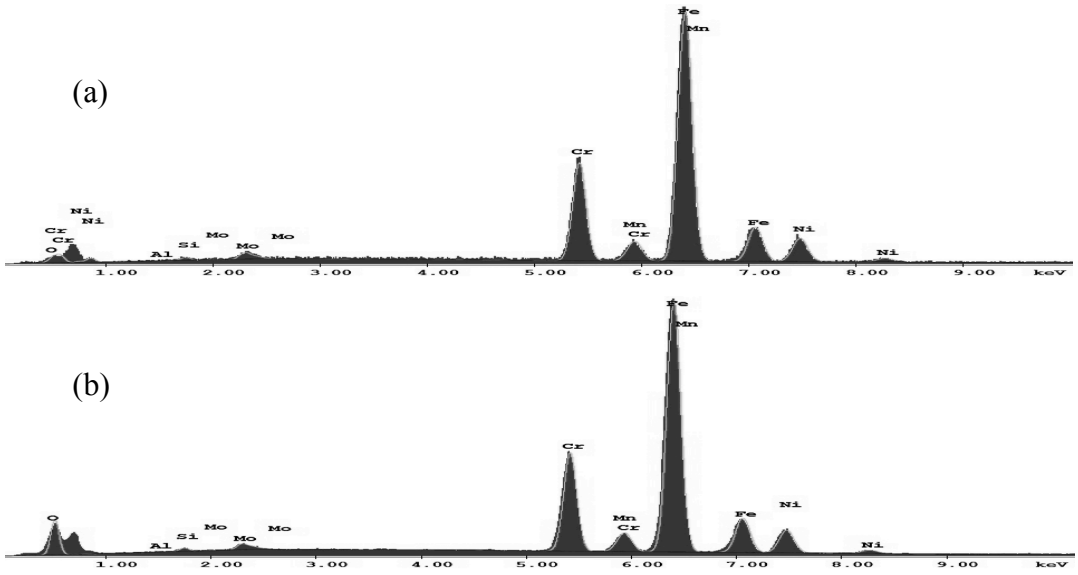

Figure 3.7 EDX spectrum of (a) untreated stainless steel coupon and (b) heat treated coupon at 700 °C for 5 h.

Surface roughness of the stainless steel coupons was quantified at three length scales. Mean roughness (S_a), root mean square roughness (S_q), and peak to valley roughness (S_{pv}) values were obtained using an optical surface profiler. Five measurements at random positions were taken then averaged and summarized in Table 3.3. The roughness defines the surface irregularities and asperities, while the topography profile describes the overall shape of the surface landscape. The topography profile and surface roughness differences of each side of the stainless steel coupon (namely side A and side B) are shown in Figure 3.8.

The roughness parameters, in terms of S_a for the untreated coupon, were 0.12 µm for side A (0.23 µm for side B). The roughness parameters slightly increased to 0.13 (0.28) and 0.15 (0.29) µm after 2 h thermal treatment at 500 and 700 °C respectively. The roughness parameters in terms of the maximum peak to valley value (S_{pv}) for the untreated coupon were 1.86 (2.35) µm. The roughness parameters increased to 2.05 (2.82) and 2.39 (3.20) µm after 2 h thermal treatment at 500 and 700 °C, respectively.

Table 3.3 Roughness parameters of untreated and heat treated stainless steel coupons.

Side	**Roughness parameter**	**Value (µm)**			
		Untreated	**500 °C, 2 h**	**700 °C, 2 h**	**700 °C, 5 h**
A	S_a	0.12 ± 0.01	0.13	0.15 ± 0.01	0.15
	S_q	0.16 ± 0.01	0.16	0.20 ± 0.02	0.19
	S_{pv}	1.86 ± 0.06	2.05 ± 0.17	2.39 ± 0.13	2.55 ± 0.25
B	S_a	0.23 ± 0.02	0.28 ± 0.02	0.29 ± 0.03	0.27 ± 0.02
	S_q	0.30 ± 0.03	0.35 ± 0.02	0.37 ± 0.03	0.34 ± 0.02
	S_{pv}	2.35 ± 0.22	2.82 ± 0.24	3.20 ± 0.31	3.35 ± 0.24

Side A Side B

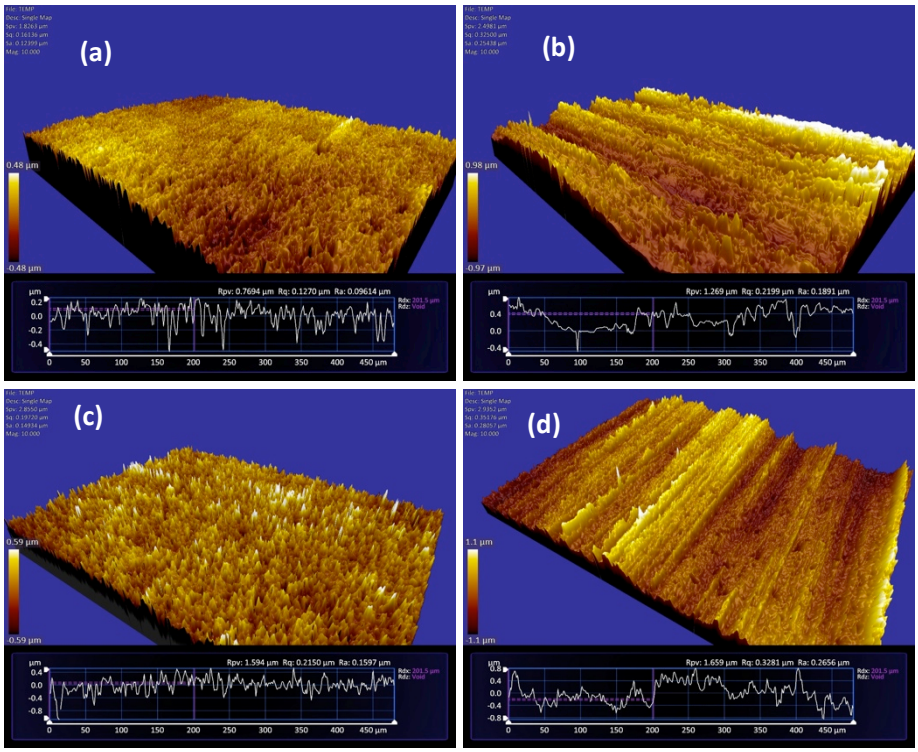

Figure 3.8 Topography profile of (a,b) untreated stainless steel coupon and (c,d) heat treated coupon at 700 °C for 5 h.

These differences in the roughness between the untreated and thermal treated substrate confirmed the development of a potential sticking point for coatings on the stainless steel surface. This sticking point will enable the coupon to be more effective for coating adherence.

3.4.2 Alumina coating on stainless steel substrate

Experimental

Alumina support was prepared with aluminum isopropoxide (Al $(iPrO)_3$) as the precursor in two steps: 1) preparation of alumina sol and, 2) coating of alumina sol on the substrate.

Alumina sols preparation

Alumina sol was prepared by mixing aluminum isopropoxide with water at 82-85 °C for 1 h. The resulted in aluminum hydroxide slurry was subsequently peptized by addition of acetic acid (HAc) and refluxed at 82-85°C for 48 h. The mixture of ethanol (EtOH) and P123, which is an amphiphilic surfactant with a formula of EO_{20}-PO_{70}-$EO_{20,}$ where EO = ethylene oxide and PO = propylene oxide, and a molecular weight of 5800: were then added to the above solution at room temperature followed by stirring for 15 h. P123 was added as a drying control chemical additive to reduce crack formation of the alumina layer and improve adhesion between the alumina layer and the substrate during drying and calcination. The formula of alumina sol is presented in Table 3.4. The sols were concentrated by boiling off ethanol at 45°C.

Coating of alumina sol on stainless steel coupon

The pretreated stainless steel coupon was submerged vertically in the alumina sol. The excess sols on the bottom edge of the coupon were towel-dried off. The coating was then dried in an oven at 120 °C for 2 h and finally calcined at 500 °C with a ramp of 5 °C /min and maintained for 5 h.

Table 3.4 Alumina sol composition.

Reagent	M.W. (g/mol)	Density (g/ml)	Volume (ml)	Mass (g)	Moles
$Al(iPrO)_3$	204.24	1.035	10.35	10	0.0490
H_2O	18.015	1.0	100	100	5.551
HAc	60.05	1.049	0.42	0.44	0.00733
P123	5,800	1.04	6.24	6	0.001034
EtOH	46.07	0.789	40.0	31.56	0.685
Total			157.01	148.0	

Coating of alumina sol on stainless steel microtube

The stainless steel microtube was first cleaned by flowing water followed by ethanol through the microtube and then dried in an oven with air flowing at 80 °C for 2 h. The thermal treatment of the stainless steel surface was accomplished by heating under air flowing at 700 °C for 5 h. The two-step, gas-assisted fluid displacement method was used for coating alumina sol in both untreated and heat-treated microtubes. The microtube was first completely filled with alumina sol prepared in the previous section. Excess fluid was removed from the channel by air flowing at 10 cm^3/min for 1 h. The coatings was then dried in an oven at 120 °C for 12 h and calcined in an air flowing through the microtube at 500 °C for 5 h. The masses of the empty, full, and coated microtube were measured throughout the coating procedure.

Alumina coating characterization

Samples of the coated coupons were analyzed using an optical microscope and scanning electron microscopy (SEM) for their surface morphology. The alumina thickness was measured from SEM image of cross sectional view of the coupon. Typical magnifications of the images were in the range of 200 to 20,000. The stainless

steel tube was cut to obtain cross-section samples and characterized for wall coating thickness with a scanning electron microscopy (SEM) at various parts of microtube.

Elemental analysis of alumina coated inside the microtube was accomplished using Energy-dispersive analysis of X-ray (EDX). The alumina sol sample for EDX analysis was collected at the exit of microtube during alumina sol coating process.

Adhesion test

The adhesion of alumina coating was determined by measuring mass loss as a function of time of treatment with sonication. The coated coupons were soaked into dodecane contained inside a beaker and then treated in an ultrasonic bath (Branson 1510 with operating frequency of 40 kHz and power rating of 80 W) and later dried in an oven at 120 °C for 2 h. The percentage of mass loss was calculated from

$$Mass\,loss = \frac{(w_c - w_s)}{(w_c - w_u)} x100\% \qquad (3.1)$$

where w_u = mass of stainless steel coupon before coating (g)

w_c = mass of stainless steel coupon after coating (g)

w_s = mass of stainless steel coupon after sonication treatment (g)

Result and Discussion

Optical micrograph and SEM micrograph of alumina coating on stainless steel coupons obtained after the dip-coating technique followed by calcination at 500 °C showed transparent, uniform and crack-free surfaces (Figure. 3.9). SEM image becomes blurred after coating with alumina because alumina is less electron-conductive.

The adhesion of alumina coating is an important key in the development of a catalyst coating in a microreactor and it is usually checked by a harsh treatment in an

ultrasonic bath. Figure 3.10 shows the mass loss of alumina coating as a function of time of treatment in an ultrasonic bath. A mass loss of 15 % was observed during the first 15 min and then the mass loss increased slowly and remained constant after 90 min. Around 22 % of the alumina coating was removed after 180 min.

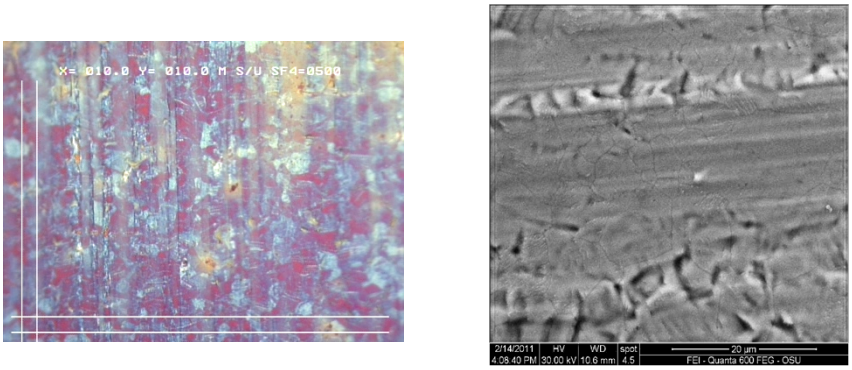

Figure 3.9 Surface view of an alumina coating layer by optical micrograph (left) and scanning electron micrographs (right).

The surface morphologies and cross sectional views for alumina coating in a microtube with a 10 cm^3/min purge air flow rate are shown in Figure 3.11. A rough surface coating was observed, which was probably caused by, the process of alumina sol flushing with air. However, no obvious cracks appear and the coating layer adheres to the microchannel firmly. The thickness of alumina coating was observed at three different points along the length of the microtube to determine the axial coating uniformity. SEM images show the overall axial uniformity of an alumina coating in microtube with 10 cm^3/min air flowrate (Figure 3.12). The actual thickness for alumina coating is between 1.02- 2.40 µm with an average value of 1.52±0.39 µm. For the determination of radial uniformity, the thickness was observed at four different points along the wall of microtube. The coating thickness is uniform along the wall of the microtube with an average thickness of 1.31±0.15 µm. These values are slightly larger than the theoretical thickness of 1.19±0.06 µm, which was calculated from alumina weight using a density for alumina of 4 g/ml, and assuming 25% of density.

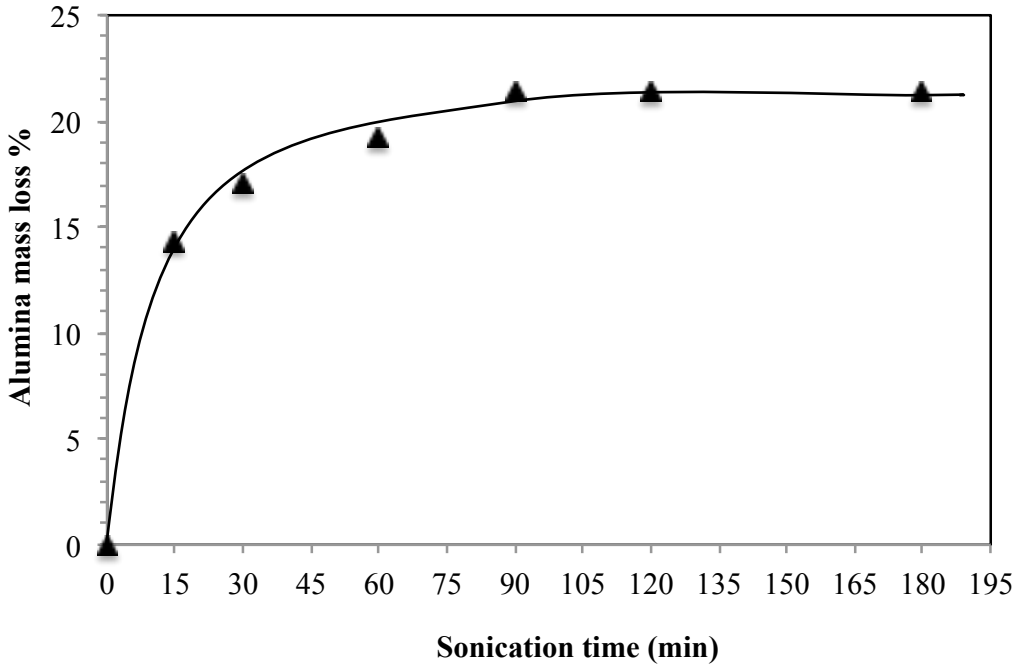

Figure 3.10 Alumina mass loss as a function of time of ultrasonic treatment.

The effect of the purge air flow rate on alumina coating thickness was studied with air flow rate of 10 and 200 cm^3/min. The results of coating studies of 500 μm diameter microtube that were 50 cm long are shown in Table 3.5. The coating thickness of the alumina layer slightly decreased with an increasing purge airflow rate from 10 to 200 cm^3/min.

The metal oxide was created on the top layer of pretreated stainless steel substrate, which is confirmed by EDX analysis as shown in Section 3.4.1. Due to the very thin layer of alumina support coating and small dimension of microtube, it is possible that some metal oxide might have dissolved into the alumina oxide layer during the flow coating process. Thus, alumina sol was collected at the exit of both untreated stainless steel microtube and heat-treated stainless steel microtube during the flow coating process. The alumina sol samples were then dried and analyzed by EDX technique for elemental composition. The results showed that alumina sol collected at the exit of

untreated stainless steel microtube mainly consists of Al and O. While Al, O, Fe, Mn, Cr and Ni were detected in the alumina sol sample, which was collected at the exit of pretreated stainless steel microtube. These results confirmed the assumption of dissolving metal oxide into the alumina support layer.

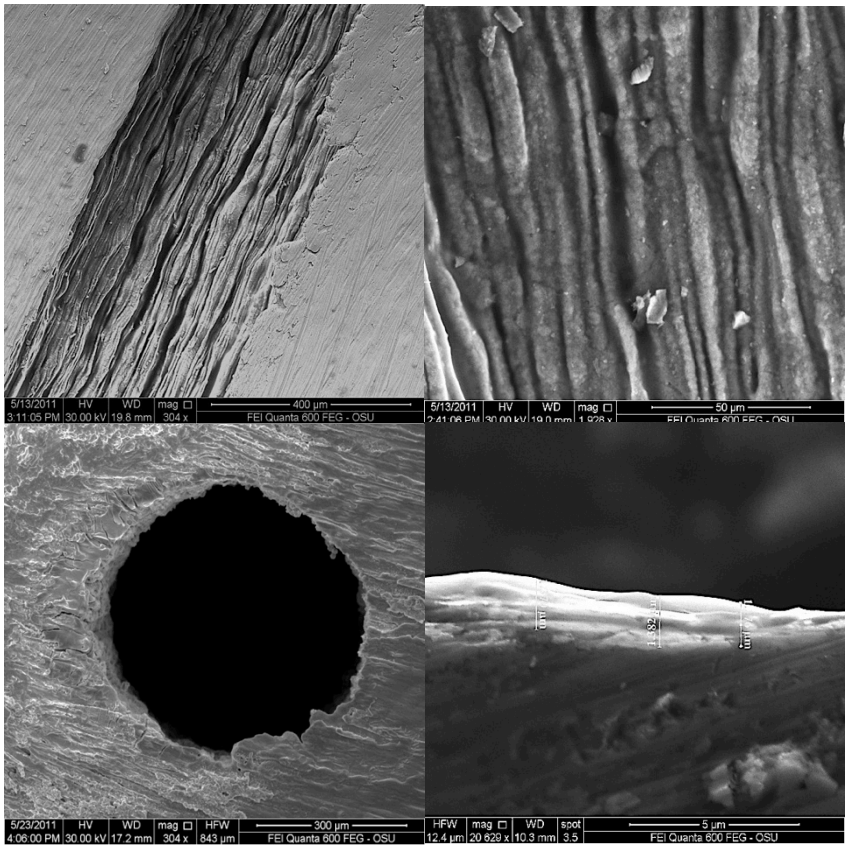

Figure 3.11 Scanning electron micrographs. Surface and cross sectional view of an alumina coating in microtube.

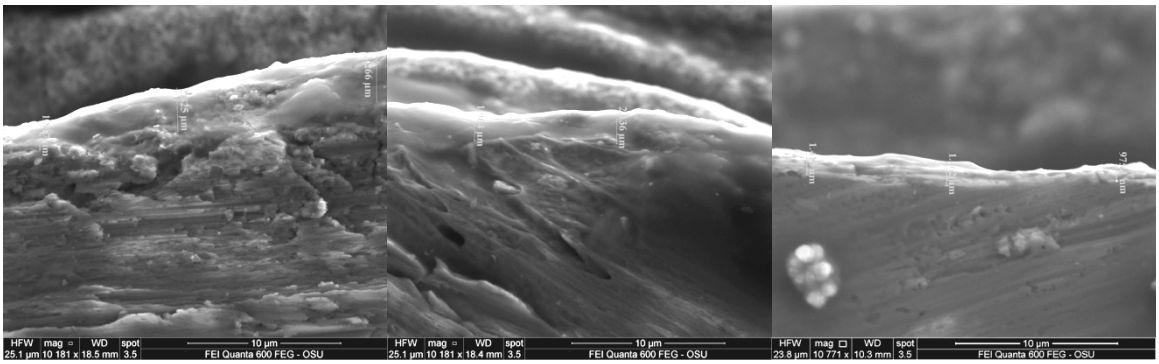

Figure 3.12 The scanning electron micrographs images of alumina coating from three different points along the length of microtube with 10 cm^3/min purging air flow rate.

Table 3.5 Effect of purging air flow rate on alumina coating thickness.

Purge flow (cm^3/min)	Coating thickness (µm)			
	Point A	Point B	Point C	Average
10	2.10±0.30	1.38±0.35	1.08±0.06	1.52±0.39
200	1.16±0.34	1.12±0.12	1.40±0.16	1.23±0.09

3.4.3 Impregnation of active metal catalyst on alumina Layer

Experimental

Impregnation solution preparation

The impregnation solution containing the required amount of ammonium heptamolybdate [$(NH_4)_6Mo_7O_{24}\cdot 4H_2O$, APM], nickel nitrate [Ni $(NO_3)_2\cdot 6H_2O$], phosphoric acid (H_3PO_4) and carbamide ($(NH_2)_2CO$) in water was prepared according to the method described by Klimov et al. [34]. Ammonium heptamolybdate was slowly added to the phosphoric acid solution with continuous stirring at room temperature. Nickel nitrate was added to the solution, resulting in a transparent green

solution. Finally, carbamide was added to the catalyst solution to prevent the precipitation during a prolong periods.

Catalyst impregnation procedure

The impregnation solution that was discussed in the previous section was used to impregnate the alumina layer on stainless steel coupons and inside the stainless steel microtubes. For stainless steel coupons, the coupon was submerged in impregnation solution at room temperature for 30 min. Then the samples were rinsed with DI water, followed by purging with pressurized air and drying in an oven at 120 °C for 2 h. After impregnation, the catalyst was calcined in a furnace by gradually increasing the temperature to 500 °C, which was then maintained for 4 h. The effect of multiple impregnation cycles with interim calcination on the active metal concentration was also studied.

For stainless steel microtube, the impregnation solution was first filled into the microtube at room temperature. After the end of a soaking time (30 min), the solution was purged from the microchannel using pressurized air at 20 cm^3/min for 30 min. Then the samples were rinsed by flowing DI water for 5 min, followed by air purging for 30 min and drying in an oven under air flow at 120 °C for 12 h. The impregnated support was finally calcined in a furnace by gradually increasing temperature to 500°C and maintaining it for 4 h.

Table 3.6 Component concentration in impregnation solution.

Reagent	**Component concentration (mol/dm^3)**
H_3PO_4	0.74
Mo (as APM)	1.47
$Ni(NO_3)_2$	0.74
$(NH_2)_2CO$	0.75

Catalyst characterization

The surface morphology of catalyst was studied using optical microscope and SEM. Elemental analysis of the coating was done using Energy-dispersive analysis of X-ray (EDX) and X-ray Photoelectron Spectroscopy (XPS), (ESCALAB 250, ThermoScientific, U.S.A.).

Result and Discussion

From the optical and SEM images, no crack was observed for the catalyst prepared in this study. The effects of the impregnation cycle on the amount of deposited metal on the alumina layer were studied by EDX. It should be noted that the thickness of the layer analyzed by EDX is about 1-5 μm. Therefore, EDX analysis of thin catalyst layer (i.e. less than 5 μm thickness) coated on stainless steel substrate will included the elemental composition of stainless steel substrate below the coating layer. Si/SiO_2 was used as a substrate for preparing the sample for surface composition analysis by EDX in this study and the effects of an impregnation cycle on the metal concentration in the alumina coated on Si/SiO_2 is summarized in Figure 3.13. Due to the high concentration of impregnation solution and very thin alumina support layer, the metal content in the coating layer was close to the target value after only one impregnation cycle. Ni and Mo concentration increased with the number of impregnation cycle, while P concentration was almost constant.

Bulk and surface concentrations of catalyst coatings on stainless steel substrate after 1-impregnation cycle was quantified by EDX and XPS technique respectively. The coating layer was carefully scrapped off from the stainless steel coupon to obtain a powder sample for EDX analysis. The thickness of the layer analyzed by these two techniques is different by orders of magnitude: about 5 μm by EDX but only 5 nm by XPS. Hence, EDX analysis is more global than XPS, which will analyze only the outermost surface of the coating layer. Table 3.7 lists the elemental composition of Ni,

Mo and P species after 1-impregnation cycle. XPS depth profiling was determined in order to study the distribution of the major component in the coating layer. A depth profile of the surface was obtained by sputtering the surface with Argon ions and the results are plotted in Figure 3.14.

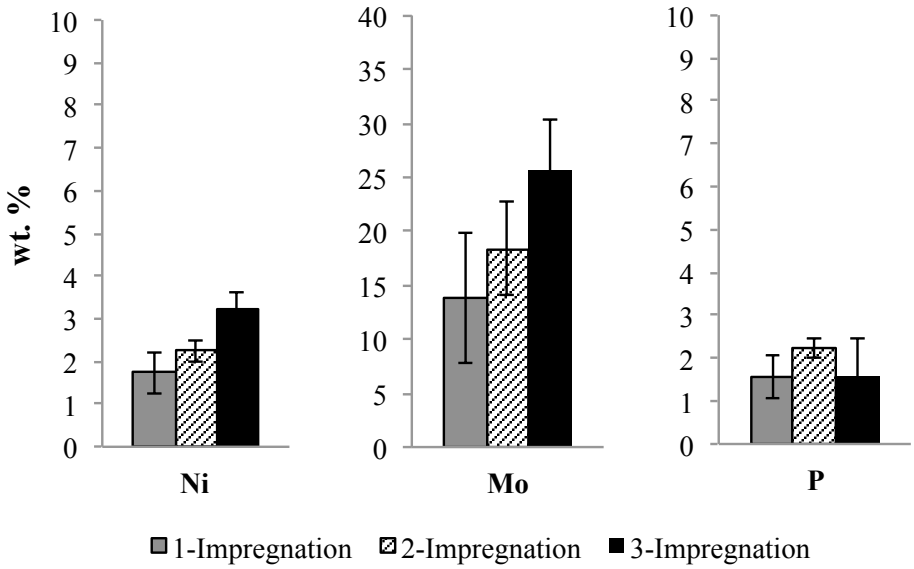

Figure 3.13 Effect of catalyst impregnation cycle on the metal composition.

Table 3.7 Bulk and surface concentrations (wt.%) for catalyst.

Element	Metal Concentration (wt.%)	
	Bulk composition by EDX	**Surface composition by XPS**
Ni	2.27	2.11
Mo	8.85	11.21
P	2.19	6.54

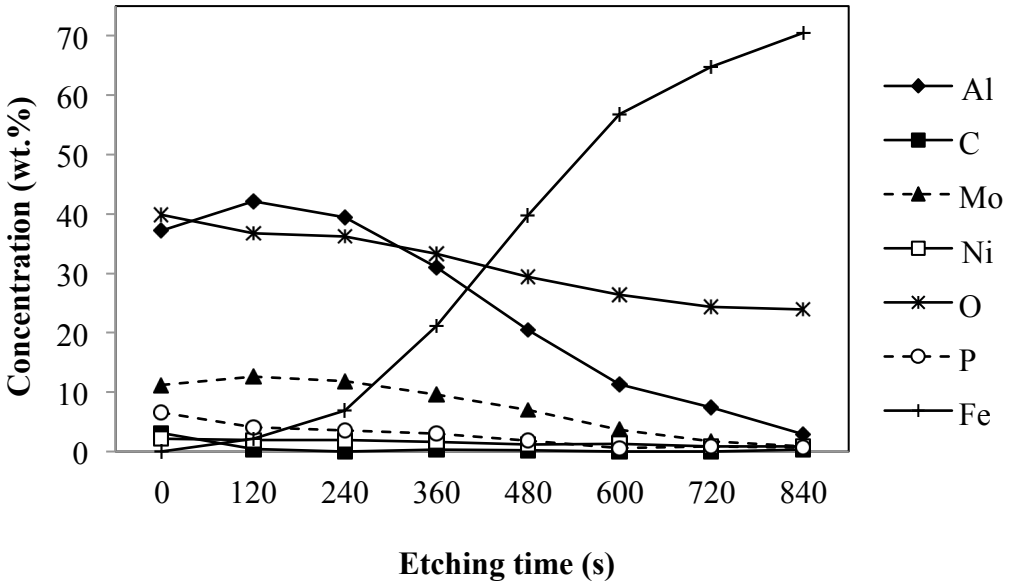

Figure 3.14 XPS depth profile of coating layer.

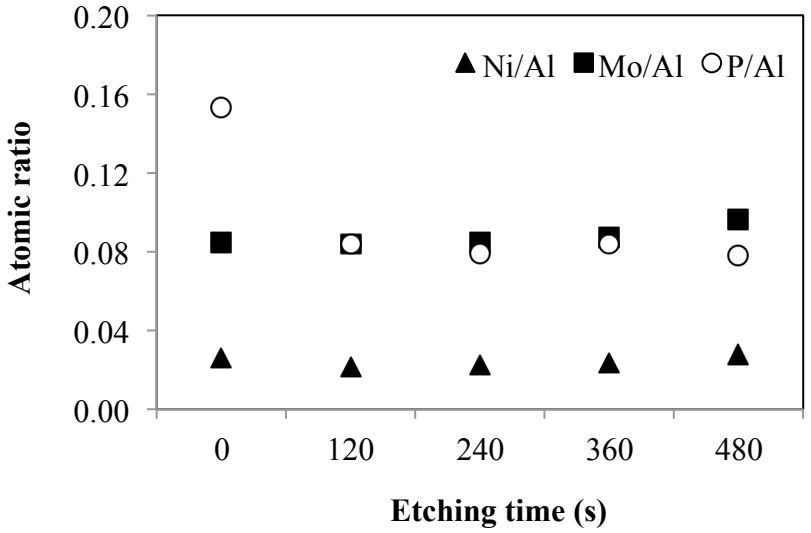

Figure 3.15 XPS atomic ratio for different etching time of coating layer.

The result indicated that the outermost surface of coating layer (etching time = 0 s) was composed mainly of Ni, Mo, P, C, Al and O. The surface concentration of elements measured by XPS is slightly different from that in the bulk determined by

EDX (powder sample). The Ni and Mo concentrations determined by XPS were close to the bulk composition, whereas the P concentration showed considerable differences between the surface and bulk value. This is probably due to the enrichment of P in the surface region, which was confirmed by XPS depth profiling analysis. The measured concentrations of Ni and Mo from both methods were close to the calculated value from starting material used in the catalyst preparation (3.25% Ni and 10.6% Mo).

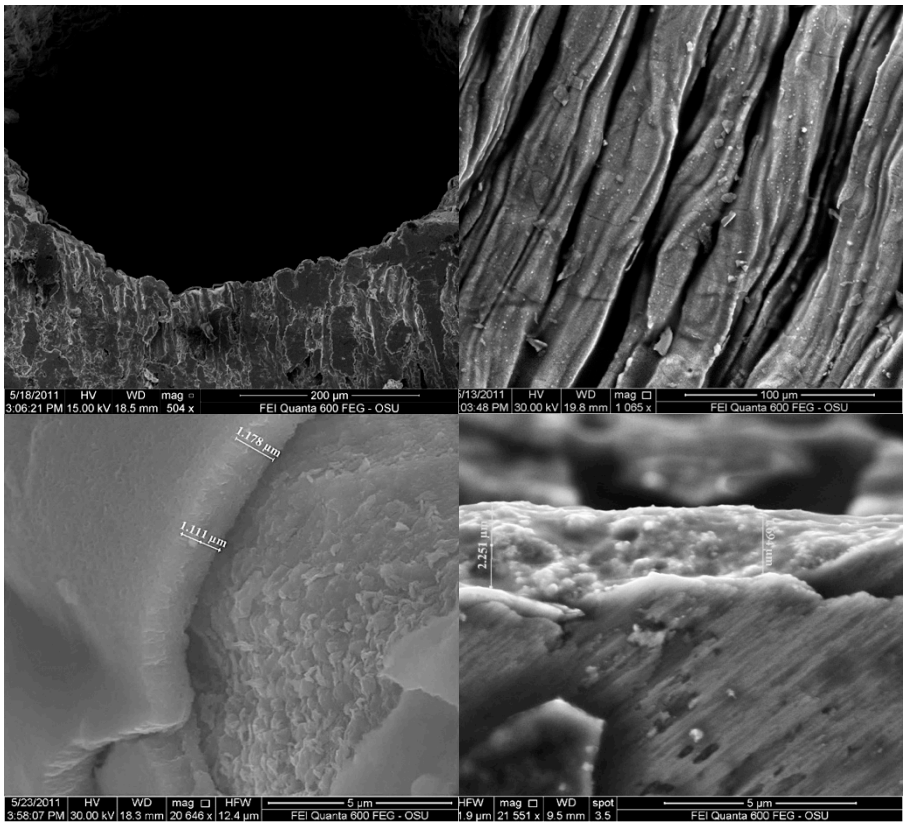

Figure. 3.16 Scanning electron micrographs. Surface and cross sectional view of NiMoP on alumina coating.

Figure 3.15 shows the results for XPS analysis in terms of the atomic ratios of Ni, Mo and P to Al at different etching times. It is observed that the Ni/Al and Mo/Al ratios are almost constant, whereas there is a noticeable drop in P/Al at the beginning of the

etching time. This result indicated that both Ni and Mo are well dispersed on alumina and the coating layer has a much greater preferential distribution of P towards the surface. Figure 3.16 shows the surface and cross- sectional view of NiMoP/Al_2O_3 catalyst layer in stainless steel microtubes. No significant morphological differences were observed between the alumina coating and NiMoP impregnated-alumina coating, according to the SEM image.

3.5 References

[1] Chorkendorff, I. and Niemantsverdriet, J. W., 2007, Concept of modern catalysis and kinetics, 2nd Edition, Wiley-Vch.

[2] Krar, M., Kovacs, S., Kallo D. and Hancsok, J., 2010, Fuel propose hydrotreating of sunflower oil on CoMo/Al2O3 catalyst, Bioresource technology, 101, 9287-9293.

[3] Donnis, B., Egeberg, R. G., Blom, P. and Knudsen, K. G., 2009, Hydroprocessing of Bio-Oils and Oxygenates to Hydrocarbons. Understanding the Reaction Routes, Top Catal, 52, 229–240.

[4] Truyen, D., Courty, M., Alphonse, P. and Ansart. F., 2006, Catalytic coatings on stainless steel prepared by sol–gel route, Thin Solid Films, 495, 257 – 261.

[5] Kubickova, I., Snare, M., Eranen, K., Maki-Arvela, P. and Murzin, D. Y., 2005, Hydrocarbons for diesel fuel via decarboxylation of vegetable oils, Catalysis today, 106, 197-200.

[6] Wildschut, J., Mahfud, F. H., Venderbosch, R. H. and Heeres, H. J., 2009, Hydrotreatment of Fast Pyrolysis Oil Using Heterogeneous Noble-Metal Catalysts. Ind. Eng. Chem. Res., 48, 10324–10334.

[7] Ferdous, D., Dalai, A.K. and Adjaye, J., 2004, Series of NiMo/Al_2O_3 catalysts containing boron and phosphorus Part I. Synthesis and characterization, Applied Catalysis A: General, 260,137–151.

[8] Kraus, H. and Prins, R., 1997, The Effect of Phosphorus on Oxidic NiMo(CoMo)/Al_2O_3 Catalysts: A Solid State NMR Investigation, Journal of Catalysis, 170, 20–28.

[9] Sundaramurthy, V., Dalai, A.K. and Adjaye, J., 2008, The effect of phosphorus on hydrotreating property of NiMo/γ-Al_2O_3 nitride catalyst, Appl. Catal. A: Gen., 335, 204–210.

[10] Otterstedt, J.E., Gevert, S.B., Jaras, S.G. and Menon, P.G., 1986, Fluid Catalytic Cracking of Heavy (Residual) Oil Fractions - A Review, Appl. Catal., 22(2), 159.

[11] Furimsky, E. and Massoth, F.E., 1999, Deactivation of Hydroprocessing catalysts, Catal.Today, 52(4), 381.

[12] Furimsky, E., 2000, Catalytic hydrodeoxygenation, Appl. Catal. A, 199(2), 147.37-38.

[13] Elliott, D.C., 2007, Historical Developments in Hydroprocessing Bio-oils. Energy, Fuel, 21(3), 1792.

[14] Brito, A., Arvelo, R., Gonzalez, A. R., Borges, M. E. and Fierro. J. L. G., 1998, Variation in Structural Characteristics of a Hydrotreatment, Catalyst with Deactivation/Regeneration Cycles, Ind. Eng. Chem. Res., 37, 374-379.

[15] Avila, P., Montes, M., Miro and E.E., 2005, Monolithic reactors for environmental applications A review on preparation technologies, Chemical Engineering Journal, 109, 11.

[16] Cebollada, P.A.R. and Garcia-Bordejé, E., 2009, Optimisation of physical properties of alumina coating microreactors used for the growth of a carbon nanofiber layer, Chemical Engineering Journal, 149, 447–454.

[17] Meille, V., 2006, Review on methods to deposit catalysts on structured surfaces, Applied Catalysis A: General, 315, 1–17.

[18] Kobayashi, Y., Ishizaka T. and Kurokawa, Y., 2005, Preparation of alumina films by the sol-gel method. Journal of Materials Science, 40, 263– 283.

[19] Haas-Santo, K., Fichtner, M., Schubert, K., 2001, Preparation of microstructure compatible porous supports by sol–gel synthesis for catalyst coatings, Applied Catalysis A: General, 220, 79–92.

[20] Fei, W., Kuiry, S. C., Sohn, Y. and Seal, S., 2003, Sol gel alumina coating on Fe-Cr-Al-Y fibre media for catalytic converters, Surface Engineering, 19 (3), 189-194.

[21] Zhen-lin, W. and Rong-chang, Z., 2010, Comparison in characterization of composite and sol-gel coating on AZ31 magnesium alloy, Trans. Nonferrous Met. Soc. China, 20, s665-s669.

[22] Zapf, R., Kolb, G., Pennemann, H. and Hessel, V., 2006, Basic study of adhesion of several Alumina-based washcoats deposited on stainless steel microchannels, Chem. Eng. Technol., 29(12), 1509-1512.

[23] Germani, G., Stefanescu, A., Schuurman, Y. and Van Veen, A.C., 2007, Preparation and characterization of porous alumina-based catalyst coatings in microchannels. Chemical Engineering Science, 62, 5084 – 5091.

[24] Stefanescu, A., van Veen, A.C., Duval-Brunel, E., and Mirodatos, C., 2007, Investigation of a Ni-based steam reforming catalyst developed for the coating of microstructures, Chemical Engineering Science, 62, 5092 – 5096.

[25] Peela, N. R., Mubayi, A.and Kunzru, D., 2009, Washcoating of alumina on stainless steel microchannels, Catalysis Today, 147S, S17–S23.

[26] Bravo, J., Karim, A., Conant, T., Lopez, G. P. and Datye, A., 2004, Wall coating of a $CuO/ZnO/Al_2O_3$ methanol steam reforming catalyst for micro-channel reformers, Chem. Eng. J., 101, 113-121.

[27] Park, G.G., Yim, S.D., Yoon, Y. G., Kim, C. S., Seo, D. J., and Eguchi, K., 2005, Hydrogen production with integrated microchannel fuel processor using methanol for portable fuel cell systems, Catalysis Today, 110, 108–113.

[28] Conant, T., Karim, A., and Datye, A., 2007, Coating of steam reforming catalysts in non-porous multi-channeled microreactors, Catalysis Today, 125, 11–15.

[29] Hwang, S. M., Kwon, O. J., and Kim, J. J., 2007, Method of catalyst coating in micro-reactors for methanol steam reforming, Applied Catalysis A: General, 316, 83–89.

[30] Vergunst, T., Kapteijn, F. and Moulijn, J.A., 2001, Monolithic catalysts: non-uniform active phase distribution by impregnation, Applied Catalysis A: General 213, 179–187.

[31] Cervello, J., Hermana, E., Jimenez, J. F. and Melo, F, 1976, In: *Preparation of catalysts* I. Eds. Delmon, B., Jacobs, P.A. and Poncelet, G., Elsevier, Amsterdam, 251.

[32] Fierro, J. L.G., Grange, P. and Delmon, B., 1987, Control of concentration profiles by rational preparation of pelted hydro-desulphurization catalysts, Stud. Surf. Sci. Catal, 31, 591-603.

[33] Liu, F., Xu, S., Cao, L., Chi, Y., Zhang, T. and Xue, D., 2007, Comparison of $NiMo/Al_2O_3$ Catalysts Prepared by Impregnation and Coprecipitation Methods for Hydrodesulfurization of Dibenzothiophene, J. Phys. Chem. C, 111, 7396-7402.

[34] Klimov, O. V., Fedotov, M. A., Pashigreva, A. V., Budukva, S. V., Kirichenko, E. N., Bukhtiyarova, G. A. and Noskov. A. S., 2009, Complexes Forming from Ammonium Paramolybdate, Orthophosphoric Acid, Cobalt or Nickel Nitrate, and Carbamide in Solution and Their Use in the Preparation of Diesel Fuel Hydrodesulfurization Catalysts, Kinetics and Catalysis, 50(6), 867–873.

[35] Zhao, S., Zhang, J., Weng, D. and Wu, X., 2003, A method to form well-adhered γ-Al_2O_3 layers on FeCrAl metallic supports, Surface and Coatings Technology, 167(1), 97-105.

CHAPTER 4

MODELING OF MULTIPHASE CHEMICAL REACTION FLOW IN MICROCHANNEL

A detailed mathematical model that describes the multiphase chemical reaction flow in a microchannel reactor was developed in this work. This model can be used as an analytical tool for kinetics parameter estimation and used as a design tool for optimal hydrotreating reactor design. The level set method was used to track the interface between the two fluids in order to model the gas-liquid slug flow formation phenomena in a microchannel and implemented in COMSOL Multiphysics software. However, using this approach to solve the complete gas-liquid slug flow system for mass transfer with chemical reaction requires extensive computational resources. The gas-liquid slug flow is an alternating flow of a gas bubble and liquid slug. Thus, only one period of the flow with a pair of stationary gas bubble and liquid slug was used for modeling mass transfer with chemical reaction in this study. The kinetic rate equations were combined with mass transport equations. COMSOL numerical simulation and MATLAB were used to estimate parameters of the process kinetics by adjusting the parameters until the mathematical model matches with the experimental data. Details of the kinetic parameters estimation will be presented later in Chapter 6.

4.1 Mathematical model for gas-liquid slug flow formation in microchannel

4.1.1 Governing equation

The flow of the two-phase fluid system is governed by the incompressible Navier-Stokes and continuity equations with surface tension.

$$\rho\left(\frac{\partial u}{\partial t}+u\cdot\nabla u\right)-\nabla\cdot\left[\mu\left(\nabla u+\nabla u^{T}\right)\right]+\nabla p=\rho g+F_{ST} \tag{4.1}$$

$$\nabla \cdot u = 0 \tag{4.2}$$

The surface tension comes from the strong intermolecular attractive forces between molecules in a fluid which holds the molecules strongly and minimizes the surface area of slug while the wall adhesion is due to the stronger attractive forces between liquid molecules and the wall and thus the fluid makes some contact angle with the wall. The addition of surface tension to the calculation results in a source term in the momentum equation.

With level set method models, the movement of gas-liquid interface is tracked by the isolines of a level set function φ, which represents the holdup of the second phase. Therefore, level set function changes from 0 to 1. The iso-contour φ = 0.5 determines the position of the interface. Level set equation is shown in equation (4.3) where u is the fluid velocity, γ is re-initialization parameter and ε represents the thickness of the layer around the interface [1]. Typically the interface thickness $\varepsilon=h_c$ was used, where h_c is the characteristic mesh size in the region passed by the interface. For numerical stability γ should be roughly equivalent to the maximum velocity of the flow in the system [2]. The first term on the right side, that is the divergence of $\varepsilon\nabla\varphi$, acts as an artificial diffusion in order to prevent discontinuities at the interface. The second term on the right is described as a compressive flux.

$$\frac{\partial\phi}{\partial t} + u \cdot \nabla\phi = \gamma\nabla \cdot \left(\varepsilon\nabla\phi - \phi(1-\phi)\frac{\nabla\phi}{|\nabla\phi|} \right) \tag{4.3}$$

Equation (4.1) and (4.2) are solved to obtain the velocity field u, which is then used in equation (4.3) for the level set function. The varying density and viscosity depend on the level set function. Given, the density and viscosity of the first phase (ρ_1, μ_1) and second phase (ρ_2, μ_2), and taking into account that the level set function is a smooth step function, the overall density ρ and viscosity μ are described by:

$$\rho = \rho_1 + (\rho_2 - \rho_1)\varphi \tag{4.4}$$

$$\mu = \mu_1 + (\mu_2 - \mu_1)\varphi \tag{4.5}$$

4.1.2 Model geometry, Initial and Boundary condition

Figure 4.1 shows the geometry of gas-liquid micromixer. Half of it was used in the simulation. The liquid flow was split into two equal flows and then contacted with the gas flow through the micro orifice. At the initial time the main channel and one of inlet channel were filled with liquid and the velocity set to zero. At time t, gas and liquid was fed into the channel at constant volumetric flow rates. Velocity of liquid and gas were used as the boundary condition at liquid inlet and gas inlet respectively, while normal stress boundary condition was used at the outlet. The wetted wall boundary condition was used at the wall.

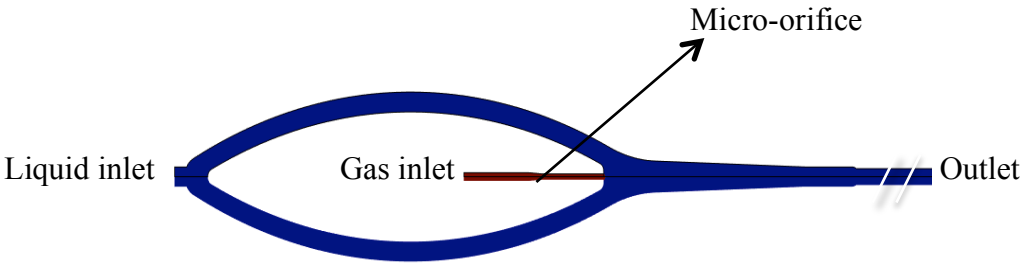

Figure 4.1 Microchannel model used in the simulation (dimension not to scale).

Table 4.1 Value of parameters used in the simulation.

Parameter	Value
Fluid pair	5wt% oleic acid in dodecane / N_2 Jatropha oil/N_2 5wt% triolein in dodecane /H_2 5wt% oleic acid in dodecane/H_2
Gas nozzle size	178 μm
Microchannel size	500 μm
Channel thickness	700 μm
Gas flow rate	0.2-0.8 ml/min
Liquid flow rate	0.1-0.4 ml/min

Table 4.2 Fluid properties used in the simulation.

Fluid	Density (kg/m^3)	Viscosity (Pa·s)	Surface tension (N/m)
N_2 at 20 °C, 1 atm	1.1648	1.7580e-5	-
H_2 at 50 °C, 34 atm	2.5359	9.493e-6	-
5 wt% oleic acid in dodecane at 20 °C, 1 atm	756.0	0.0028	0.026
5 wt% oleic acid in dodecane at 50 °C, 34 atm	737.4	0.0014	0.026
Jatropha oil at 20 °C, 1 atm	903.2	0.0526	0.030
5 wt% triolein in dodecane at 50 °C, 34 atm	738.0	0.0019	0.026

4.1.3 Experimental apparatus

Two-phase flow visualization experiments were run to validate the accuracy of the numerical model. The experimental set-up consists of an HPLC (high performance liquid chromatography) pump (SeriesIII pump, Chrom Tech, Inc., U.S.A.) for feeding the liquid phase. A Nitrogen gas cylinder equipped with a pressure regulator, electronic gas mass flowmeter (FMA 1802, Omega, U.S.A.) and 3-μm hole micro orifice for feeding the gas phase. A gas-liquid micromixer for generating the slug flow and a digital camera for capturing the images (Figure 4.2). 5 wt% oleic acid in dodecane and jatropha oil were used to determine the hydrodynamic parameters of slug flow at 20 °C. Volumetric gas flow rate was varied between 0.2 and 0.8 ml/min. Liquid feed flow rate was varied between 0.1 and 0.4 ml/min.

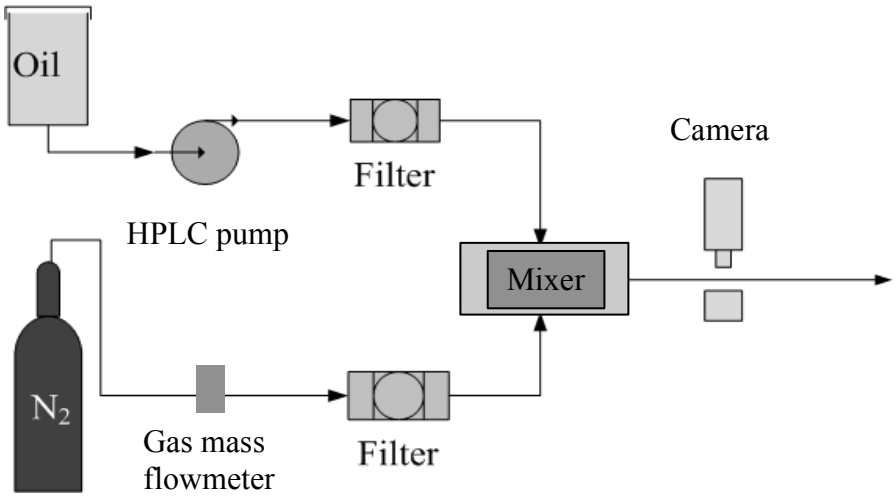

Figure 4.2 Experimental set-up for two phases flow visualization experiment.

For gas-liquid micromixer, the liquid flow was split into two equal flows and then contacted with the gas flow through the micro orifice. The mixer then focuses the flow into 500 μm circular cross sectional tubing. Transparent polyphenylsulfone tubing, with inner diameter of 500 μm and 100 cm long, was connected to micromixer via a threaded port. Images of the slug flows were photographed by a camera connected to a

computer. Liquid slug and gas bubble lengths were measured by counting pixels in the images using image-processing software (Image-j, NIH). Gas bubble and liquid slug volume were then calculated from the average value of gas bubble and liquid slug length obtained from the images.

4.1.4 Experimental results: Gas bubble and liquid slug volume

Effect of gas and liquid flow rate

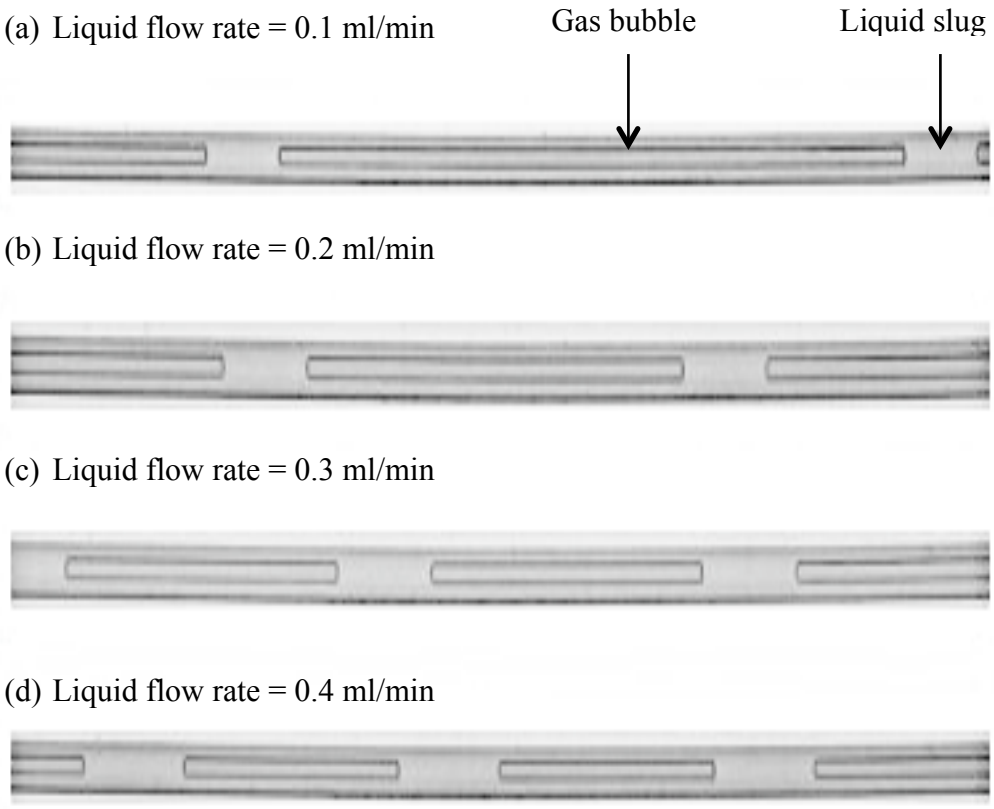

Figure 4.3 Experimental results for 5 wt% oleic acid in dodecane/ N_2 system at 0.8 ml/min gas flow rate and 20 °C.

The influence of gas and liquid flow rate on the bubble and liquid slug length was investigated for 5 wt% oleic acid in dodecane/N_2 system at 20 °C. The pictures obtained from the experiments are shown in Figure 4.3. It can be seen that gas and liquid slugs were generated in a steady and periodic manner at regular intervals in the range of liquid flow rate (0.1-0.4 ml/min) and gas flow rate (0.8 ml/min) used.

Gas bubble volume decreases and liquid slug volume slightly increases with increasing liquid flow rate as shown in Figure 4.4 and 4.5. By increasing the liquid flow rate, the detaching effect of liquid drag force increases and smaller bubbles are formed. At constant liquid flow rate, gas bubble volume increases and liquid slug volume slightly decreases with increasing gas flow rate. Gas to liquid volume ratio was slightly higher than the volume flow rate ratio because of the existence of the thin film between gas bubble and channel wall, and the fact that the slug length was computed across the central line, with the shape of the interface affecting the values.

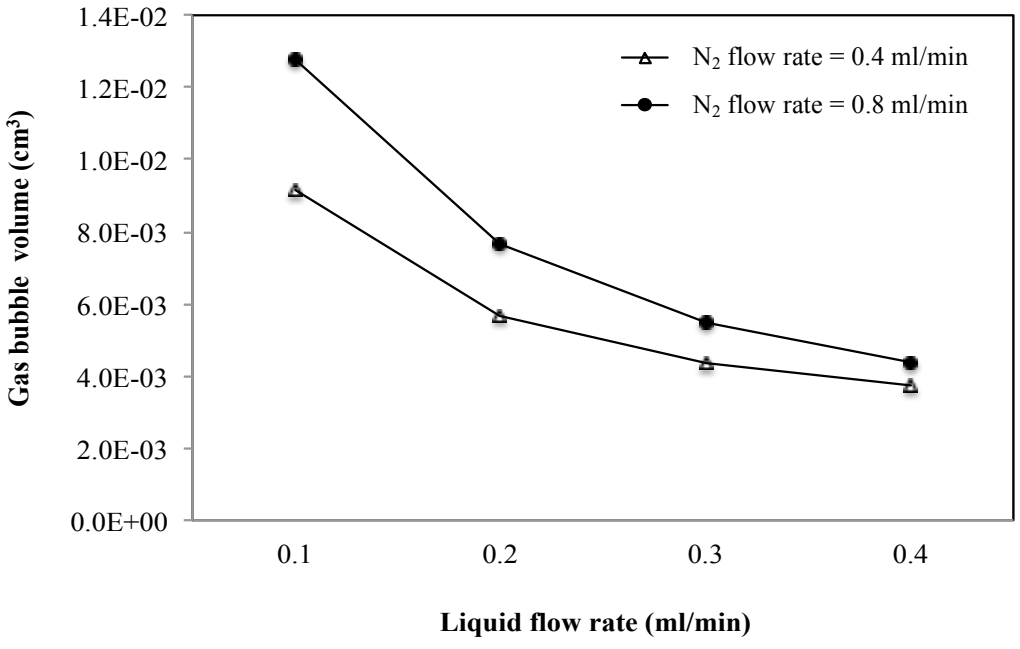

Figure 4.4 Experimental gas bubble volume as function of gas and liquid flow rate. 5 wt% oleic acid/N_2 system at 20 °C.

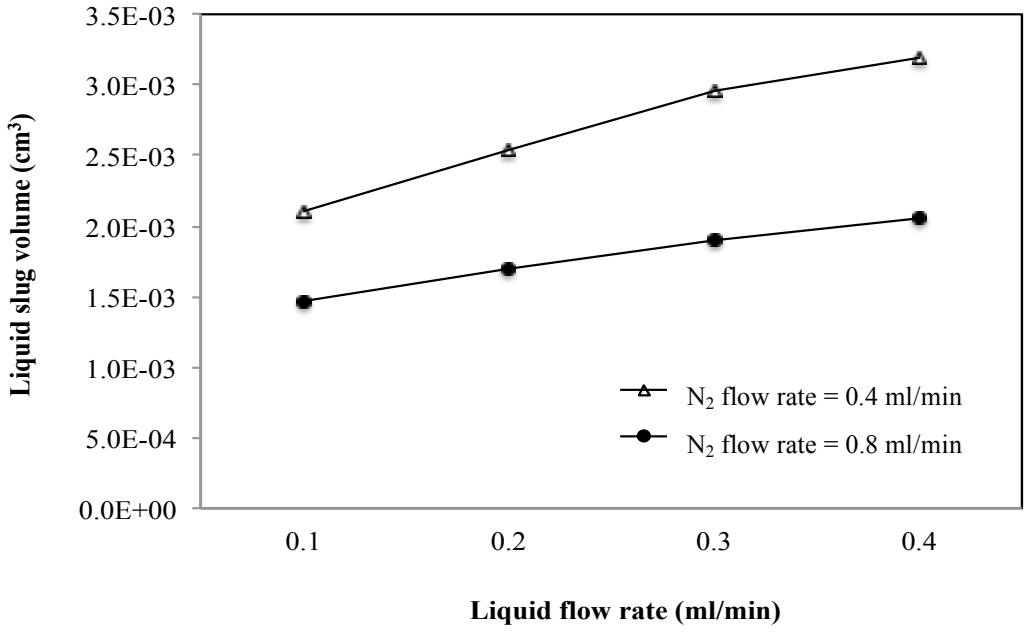

Figure 4.5 Experimental liquid slug volume as function of gas and liquid flow rate. 5 wt% oleic acid in dodecane/N_2 system, 20 °C.

Effect of liquid properties

5 wt% oleic acid in dodecane and pure jatropha oil were used to study the effect of liquid properties on the gas bubble volume and the results are shown in Figure 4.6. Gas bubble volume in jatropha oil system is smaller than 5wt% oleic acid in dodecane, which have a lower viscosity value, at the same conditions. This result suggests that the liquid viscosity affects gas bubble size. The increase of the shearing force on the gas phase caused the bubble to detach earlier and form smaller gas bubble.

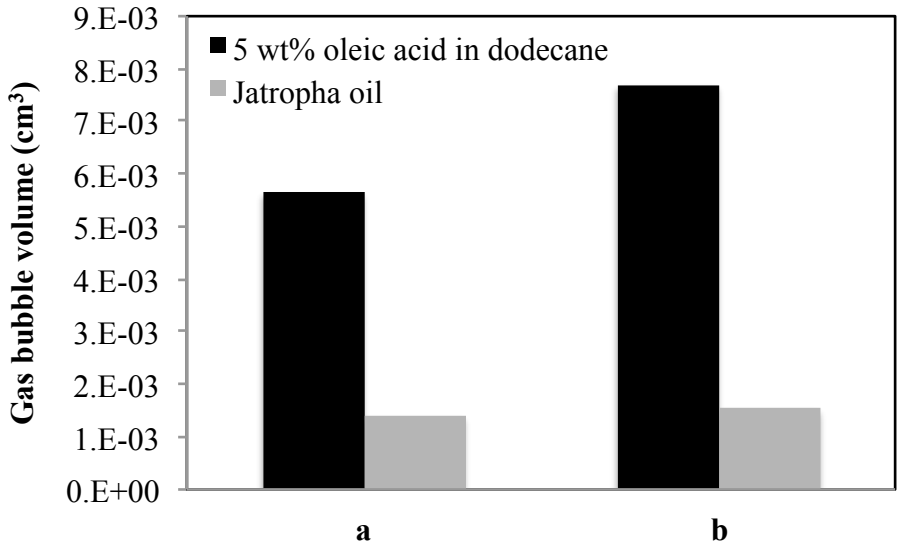

Figure 4.6 Effect of liquid properties on gas bubble volume for 5 wt% oleic acid in dodecane/N_2 and Jatropha oil/N_2 system at 20 °C, liquid flow rate = 0.2 ml/min; (a) gas flow rate = 0.4 ml/min and (b) gas flow rate = 0.8 ml/min.

4.1.5 Simulation results:

Bubble formation mechanism

Bubble formation from gas nozzle in microchannel for jatropha oil/N_2 system at 0.2 ml/min gas flow rate and 0.3 ml/min liquid flow rate is shown in Figure 4.7. The bubble formation process in Figure 4.7 can be divided into three stages: expanding, contracting and necking stage. In the initial expanding stage, gas bubble grows spherically at the top of gas nozzle due to the incoming gas flux and presence of the interfacial tension between the gas and liquid (Figure 4.7 B-D). The second stage is contracting stage (Figure 4.7 E-G) in which the bubble is pushed forward in the channel and the interface retracts back towards the channel axis. Additional gas is fed into the bubble that continues to grow further in radial direction and approach the channel wall, deviating from the spherical shape. The liquid phase starts to squeeze the gas bubble and then gas bubble forms a neck connecting them to the tip of gas nozzle

(Figure 4.7 H). Finally, the neck is detached from the gas nozzle and a bubble is formed (Figure 4.7 I).

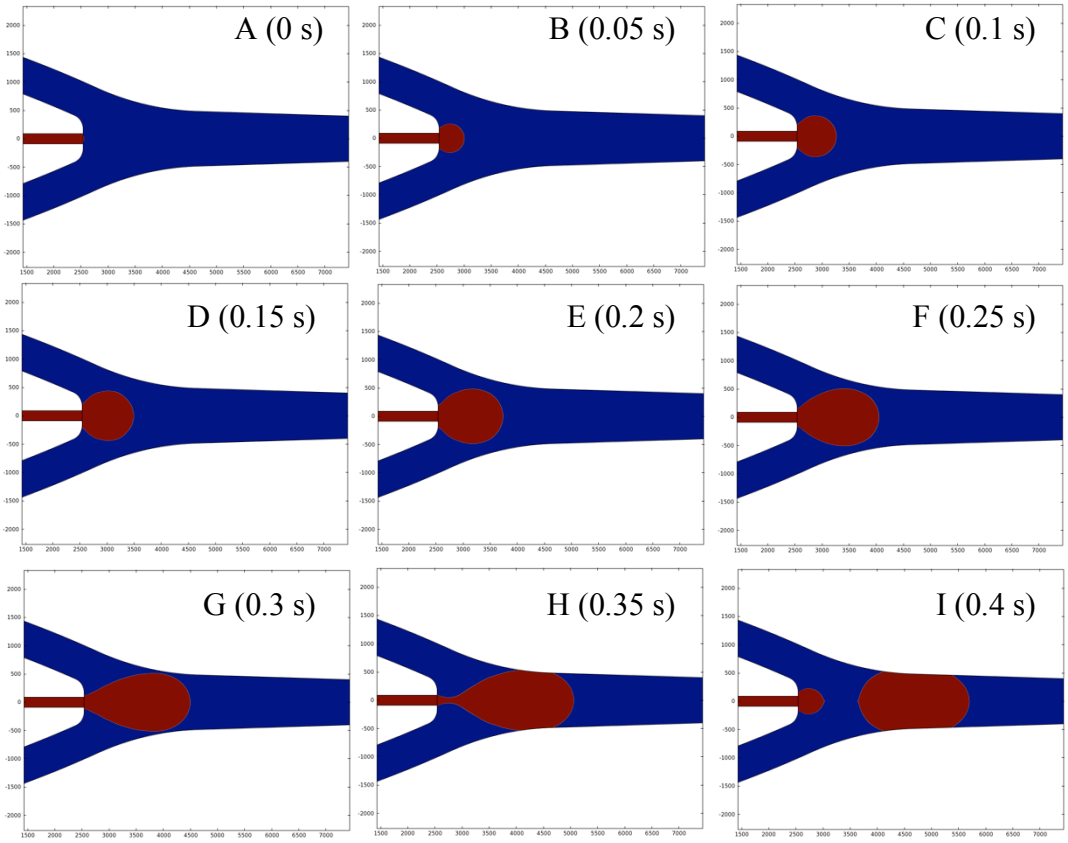

Figure 4.7 Bubble formation mechanism for Jatropha oil/N_2 system at gas flow rate = 0.2 ml/min and liquid flow rate = 0.3 ml/min; Red = Gas phase, Blue = Liquid phase.

Gas bubble and liquid slug volume

The pictures obtained from experiments and simulations are shown in Figure 4.8. It was found that the experimental values were in closer agreement with numerical predictions as shown in Figure 4.9 and 4.10. There is 25 % difference for bubble volume and liquid slug volume between experimental and numerical data. Thus this simulation method will be used to predict the bubble and liquid slug volume for gas/liquid slug flow system at high pressure and temperature, which is difficult to measure experimentally.

(a) Gas flow rate = 0.2 ml/min, liquid flow rate = 0.2 ml/min

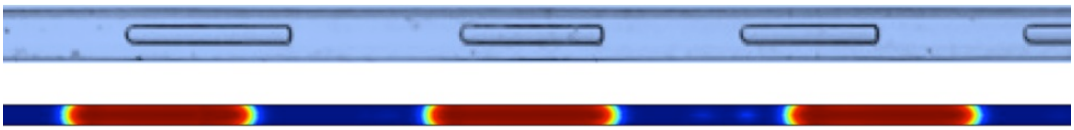

(b) Gas flow rate = 0.2 ml/min, liquid flow rate = 0.3 ml/min

Figure 4.8 Experimental results (upper) and simulation results (lower) for Jatropha oil/N_2. Red = Gas phase, Blue = Liquid phase.

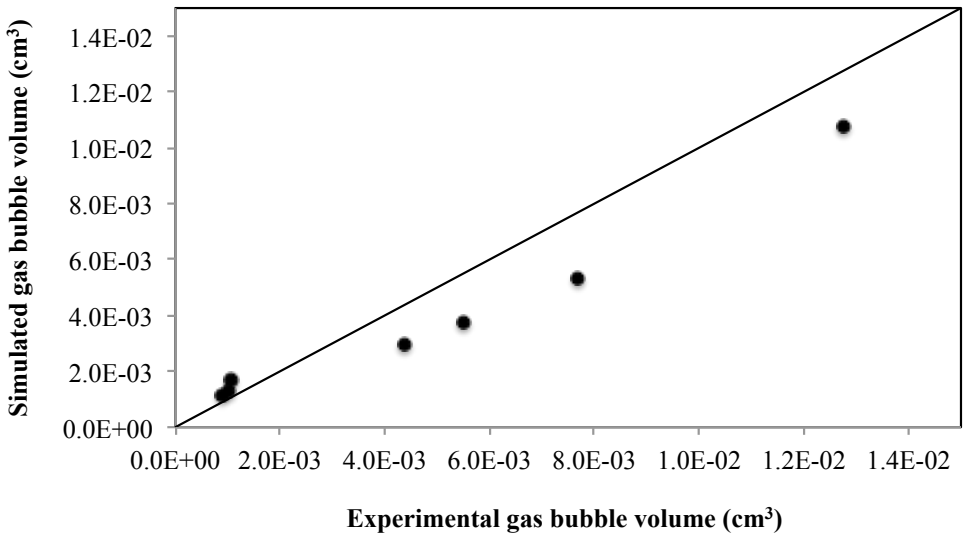

Figure 4.9 Comparison of simulation and experimental results for gas bubble volume.

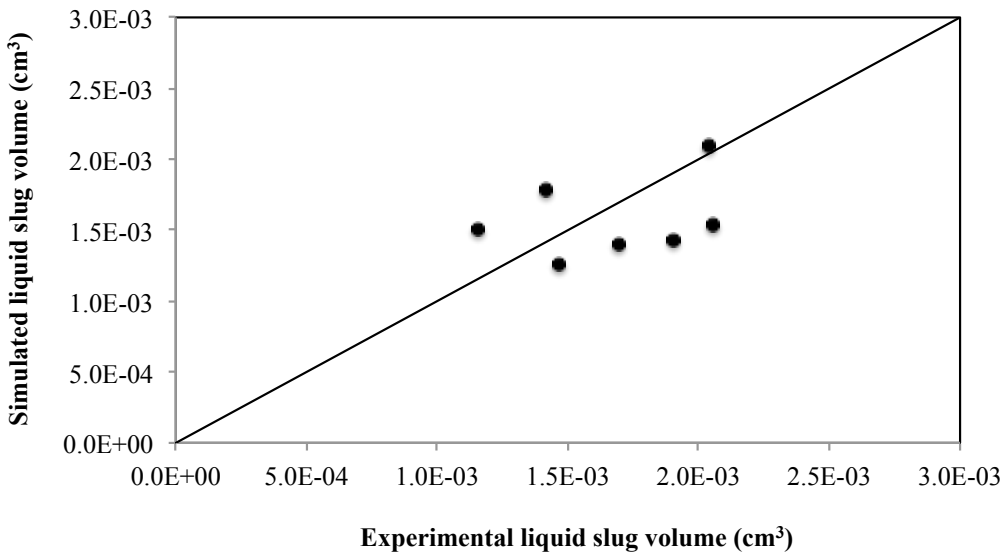

Figure 4.10 Comparison of simulation and experimental results for liquid slug volume.

4.2 Mathematical model for two-phase chemical reaction flow in microchannel

4.2.1 Model illustration

Gas-liquid slug flow system consists of two regions, white (gas) and gray (liquid) areas. The flow is assumed to be periodic with constant gas and liquid slug lengths. Thus, only one period of the flow is simulated with a pair of gas and liquid slugs. In addition, the flow is assumed to be axisymmetric, so a 2-d (r, z) computational domain was used, and geometry of the computational domain is shown in Figure 4.11.

4.2.2 Assumptions

To simplify analytical model, a model is developed using the following assumptions

1. Fluid is Newtonian, flow is incompressible.
2. The gravity in the microchannel is neglected.
3. Two-dimensional, fully developed laminar flow.

4. Mass transfer and reaction does not affect the hydrodynamics in the liquid phase.
5. Equilibrium condition at the gas-liquid interface.
6. The lengths of all bubbles and of all liquid slugs are equal, but the length of a bubble can differ from the length of a liquid slug.
7. Bubble is assumed to have a cylindrical body with spherical caps at the ends, as shown in Figure 4.11.
8. The shape and volume of both phases remain constant.
9. Isothermal conditions.
10. For triglyceride hydrotreating, there are 13 components involved in system: triglyceride (TG), diglyceride (DG), monoglyceride (MG), fatty acid (FFA), fatty alcohol (FA), long chain ester (ET), C17 hydrocarbon (C17HC), C18 hydrocarbon (C18HC), water, propane, CO, CO_2 and H_2.
11. Hydrotreating reaction can only take place on the catalyst surface.

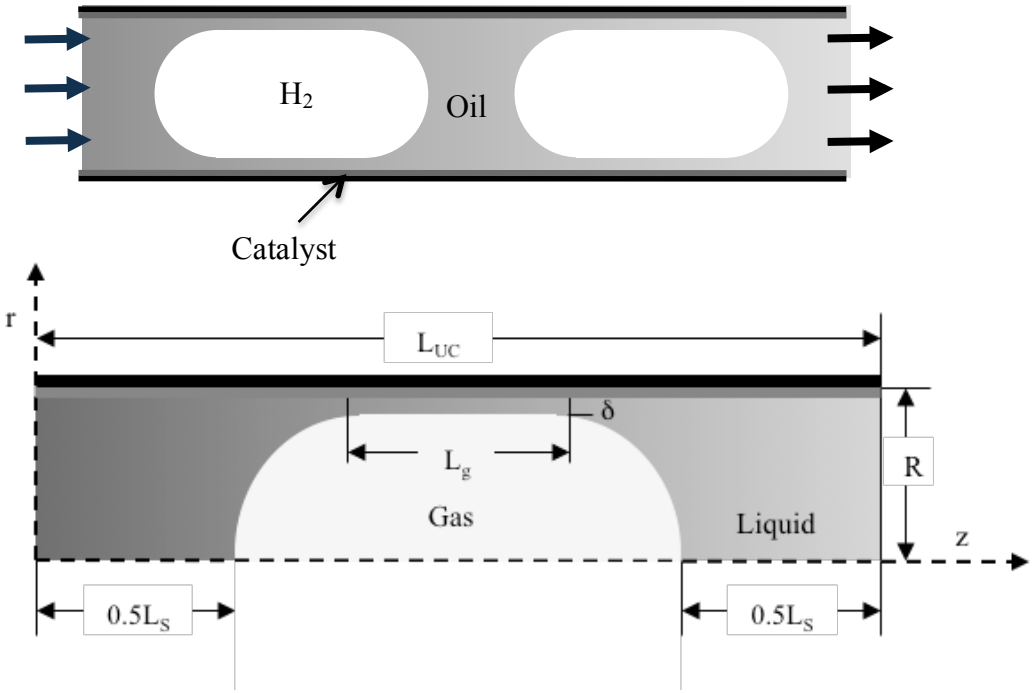

Figure 4.11 Geometry of computational domain.

4.2.3 Chemical reaction and rate equations

Several chemical reaction pathways for hydrotreating reaction of triglyceride have been proposed in literature [3,4]. The present work involves using a simplified reaction mechanism and focusing on the kinetics describing the formation of major liquid intermediate products from the hydrotreating reaction of triglyceride. The hydrotreating reaction is assumed to proceed in consecutive steps: hydrogenolysis of triglyceride to diglyceride, monoglyceride, fatty acid and propane (Reaction no. r1-r3), followed by hydrodeoxygenation(Reaction no. r4-r5), decarbonylation and decarboxylation (Reaction no. r6-r7) of the fatty acid to hydrocarbon and esterification of fatty acid and fatty alcohol (Reaction no. r8) as shown in Figure 4.12. Reactions no r1-r7 are assumed to be irreversible and reaction no. r8 a reversible reaction. First order reaction expression was used to describe the heterogeneous reaction. Esterification reaction was described by a second order reaction expression. Reaction and rate equations for hydrotreating are summarized in Table 4.3.

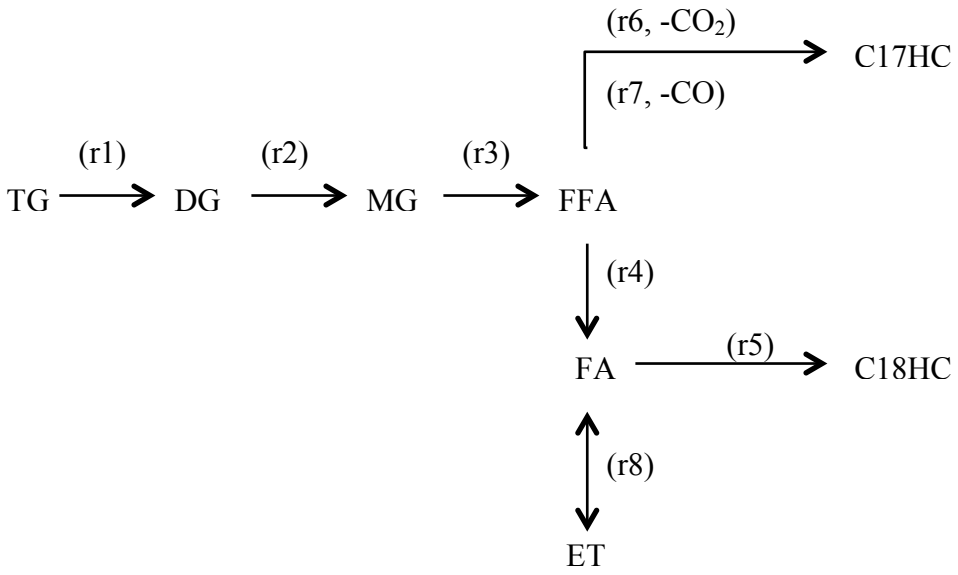

Figure 4.12 Reaction pathway for hydrotreating reaction of triglyceride.

Table 4.3 Reaction and rate equations for hydrotreating of triglyceride.

Reaction no.	Stoichiometry	Reaction rate
r1	$TG + H_2 \xrightarrow{k1} FFA + DG$	$r_1 = k_1 C_{TG}$ (4.6)
r2	$DG + H_2 \xrightarrow{k2} FFA + MG$	$r_2 = k_2 C_{DG}$ (4.7)
r3	$MG + H_2 \xrightarrow{k3} FFA + C_3H_8$	$r_3 = k_3 C_{MG}$ (4.8)
r4	$FFA + 2H_2 \xrightarrow{k4} FA + H_2O$	$r_4 = k_4 C_{FFA}$ (4.9)
r5	$FA + H_2 \xrightarrow{k5} C18HC + H_2O$	$r_5 = k_5 C_{FA}$ (4.10)
r6	$FFA \xrightarrow{k6} C17HC + CO_2$	$r_6 = k_6 C_{FFA}$ (4.11)
r7	$FFA + H_2 \xrightarrow{k7} C17HC + CO + H_2O$	$r_7 = k_7 C_{FFA}$ (4.12)
r8	$FA + FFA \underset{k9}{\overset{k8}{\rightleftharpoons}} ET + H_2O$	$r_8 = k_8 C_{FFA} C_{FA} - k_9 C_{ET} C_{H2O}$ (4.13)

The concentration of each component i as a function of time can be expressed in terms of the following differential equations for each of the 13 species.

$$\frac{dC_{TG}}{dt} = -r_1 \quad (4.14)$$

$$\frac{dC_{DG}}{dt} = r_1 - r_2 \quad (4.15)$$

$$\frac{dC_{MG}}{dt} = r_2 - r_3 \quad (4.16)$$

$$\frac{dC_{FFA}}{dt} = r_1 + r_2 + r_3 - r_4 - r_6 - r_7 - r_8 \quad (4.17)$$

$$\frac{dC_{FA}}{dt} = r_4 - r_5 - r_8 \quad (4.18)$$

$$\frac{dC_{ET}}{dt} = r_8 \tag{4.19}$$

$$\frac{dC_{C17HC}}{dt} = r_6 + r_7 \tag{4.20}$$

$$\frac{dC_{C18HC}}{dt} = r_5 \tag{4.21}$$

$$\frac{dC_{H2O}}{dt} = r_4 + r_5 + r_7 + r_8 \tag{4.22}$$

$$\frac{dC_{H2}}{dt} = -r_1 - r_2 - r_3 - 2r_4 - r_5 - r_7 \tag{4.23}$$

$$\frac{dC_{C3H8}}{dt} = r_3 \tag{4.24}$$

$$\frac{dC_{CO}}{dt} = r_7 \tag{4.25}$$

$$\frac{dC_{CO2}}{dt} = r_6 \tag{4.26}$$

4.2.4 Fluid flow

The flow of the incompressible fluid is governed by the Navier–Stokes and continuity equations. The continuity equation in cylindrical coordinates is given by

$$\frac{\partial \rho}{\partial t} + \rho\left(\frac{1}{r}\frac{\partial}{\partial r}(ru_r) + \frac{1}{r}\frac{\partial}{\partial \theta}(u_\theta) + \frac{\partial}{\partial z}(u_z)\right) = 0 \tag{4.27}$$

Navier–Stokes equations for incompressible flow of Newtonian fluids in cylindrical coordinates is given by

r-component

$$\rho[\frac{\partial u_r}{\partial t}+u_r\frac{\partial u_r}{\partial r}+\frac{u_\theta}{r}\frac{\partial u_r}{\partial \theta}+u_z\frac{\partial u_r}{\partial z}-\frac{u_\theta^2}{r}]=-\frac{\partial p}{\partial r}+\rho g_r+\mu\frac{\partial^2 u_r}{\partial r^2}+\frac{\mu}{r}\frac{\partial u_r}{\partial r}-\mu(\frac{u_r}{r^2})+\frac{\mu}{r^2}\frac{\partial^2 u_r}{\partial \theta^2}$$
$$-\frac{2\mu}{r^2}\frac{\partial u_\theta}{\partial \theta}+\mu\frac{\partial^2 u_r}{\partial z^2}$$

(4.28)

θ-component

$$\rho[\frac{\partial u_\theta}{\partial t}+u_r\frac{\partial u_\theta}{\partial r}+\frac{u_\theta}{r}\frac{\partial u_\theta}{\partial \theta}+u_z\frac{\partial u_\theta}{\partial z}+\frac{u_r u_\theta}{r}]=-\frac{1}{r}\frac{\partial p}{\partial \theta}+\rho g_\theta+\mu\frac{\partial^2 u_\theta}{\partial r^2}+\frac{\mu}{r}\frac{\partial u_\theta}{\partial r}-\mu\frac{u_\theta}{r^2}+\frac{\mu}{r^2}\frac{\partial^2 u_\theta}{\partial \theta^2}$$
$$+\frac{2\mu}{r^2}\frac{\partial u_r}{\partial \theta}+\mu\frac{\partial^2 u_\theta}{\partial z^2}$$

(4.29)

z-component

$$\rho[\frac{\partial u_z}{\partial t}+u_r\frac{\partial u_z}{\partial r}+\frac{u_\theta}{r}\frac{\partial u_z}{\partial \theta}+u_z\frac{\partial u_z}{\partial z}]=-\frac{\partial p}{\partial z}+\rho g_z+\mu\frac{\partial^2 u_z}{\partial r^2}+\frac{\mu}{r}\frac{\partial u_z}{\partial r}+\frac{\mu}{r^2}\frac{\partial^2 u_z}{\partial \theta^2}+\mu\frac{\partial^2 u_z}{\partial z^2}$$

(4.30)

The following relations $u_\theta = 0$ and $\partial/\partial\theta = 0$ were used to simplify above equations.

Then the differential equations are

$$\frac{\partial \rho}{\partial t}+\rho\left(\frac{1}{r}\frac{\partial}{\partial r}(ru_r)+\frac{\partial}{\partial z}(u_z)\right)=0 \qquad (4.31)$$

$$\rho\left[\frac{\partial u_z}{\partial t}+u_r\frac{\partial u_z}{\partial r}+u_z\frac{\partial u_z}{\partial z}\right]=-\frac{\partial p}{\partial z}+\mu\frac{\partial^2 u_z}{\partial r^2}+\frac{\mu}{r}\frac{\partial u_z}{\partial r}+\mu\frac{\partial^2 u_z}{\partial z^2} \qquad (4.32)$$

$$\rho\left[\frac{\partial u_r}{\partial t}+u_r\frac{\partial u_r}{\partial r}+u_z\frac{\partial u_r}{\partial z}\right]=-\frac{\partial p}{\partial r}+\mu\frac{\partial^2 u_r}{\partial r^2}+\frac{\mu}{r}\frac{\partial u_r}{\partial r}+\mu\frac{\partial u_r}{r^2}+\mu\frac{\partial^2 u_r}{\partial z^2} \qquad (4.33)$$

The boundary conditions are

- At t=0, $u_z = 0$ for $0 \le r \le R$
- At r = 0, $u_Z = finite$
- At r = R (wall), $u_Z = 0$

- Along the bubble surface, free slip boundary will be used, i.e. $\frac{du}{dn} = 0$, where du/dn is the velocity gradient component in the direction of the bubble surface and n is the unit normal vector pointing from liquid to the bubble surface [5].

4.2.5 Mass transfer

The governing equations are, convection–diffusion equation for the liquid phase mass transfer and diffusion equation for the gas phase mass transfer.

Liquid phase mass transfer equation in cylindrical coordinates is given by

$$D_i \frac{\partial^2 C_i}{\partial z^2} + \frac{D_i}{r} \frac{\partial\left(r \frac{\partial C_i}{\partial r}\right)}{\partial r} - u_z \frac{\partial C_i}{\partial z} = \frac{\partial C_i}{\partial t} \tag{4.34}$$

Where i represents one of the 13 species; TG, DG, MG, FFA, FA, ET, C17HC, C18HC, H_2O, C_3H_8, CO, CO_2 and H_2.

Rewriting above equation for each component

For TG:
$$D_{TG} \frac{\partial^2 C_{TG}}{\partial z^2} + \frac{D_{TG}}{r} \frac{\partial\left(r \frac{\partial C_{TG}}{\partial r}\right)}{\partial r} - u_z \frac{\partial C_{TG}}{\partial z} = \frac{\partial C_{TG}}{\partial t} \tag{4.35}$$

For DG:
$$D_{DG} \frac{\partial^2 C_{DG}}{\partial z^2} + \frac{D_{DG}}{r} \frac{\partial\left(r \frac{\partial C_{DG}}{\partial r}\right)}{\partial r} - u_z \frac{\partial C_{DG}}{\partial z} = \frac{\partial C_{DG}}{\partial t} \tag{4.36}$$

For MG:
$$D_{MG} \frac{\partial^2 C_{MG}}{\partial z^2} + \frac{D_{MG}}{r} \frac{\partial\left(r \frac{\partial C_{MG}}{\partial r}\right)}{\partial r} - u_z \frac{\partial C_{MG}}{\partial z} = \frac{\partial C_{MG}}{\partial t} \tag{4.37}$$

For FFA:
$$D_{FFA} \frac{\partial^2 C_{FFA}}{\partial z^2} + \frac{D_{FFA}}{r} \frac{\partial\left(r \frac{\partial C_{FFA}}{\partial r}\right)}{\partial r} - u_z \frac{\partial C_{FFA}}{\partial z} = \frac{\partial C_{FFA}}{\partial t} \tag{4.38}$$

For FA: $$D_{FA}\frac{\partial^2 C_{FA}}{\partial z^2}+\frac{D_{FA}}{r}\frac{\partial\left(r\frac{\partial C_{FA}}{\partial r}\right)}{\partial r}-u_z\frac{\partial C_{FA}}{\partial z}=\frac{\partial C_{FA}}{\partial t} \tag{4.39}$$

For C17HC: $$D_{C17HC}\frac{\partial^2 C_{C17HC}}{\partial z^2}+\frac{D_{C17HC}}{r}\frac{\partial\left(r\frac{\partial C_{C17HC}}{\partial r}\right)}{\partial r}-u_z\frac{\partial C_{C17HC}}{\partial z}=\frac{\partial C_{C17HC}}{\partial t} \tag{4.40}$$

For C18HC: $$D_{C18HC}\frac{\partial^2 C_{C18HC}}{\partial z^2}+\frac{D_{C18HC}}{r}\frac{\partial\left(r\frac{\partial C_{C18HC}}{\partial r}\right)}{\partial r}-u_z\frac{\partial C_{C18HC}}{\partial z}=\frac{\partial C_{C18HC}}{\partial t} \tag{4.41}$$

For ET: $$D_{ET}\frac{\partial^2 C_{ET}}{\partial z^2}+\frac{D_{ET}}{r}\frac{\partial\left(r\frac{\partial C_{ET}}{\partial r}\right)}{\partial r}-u_z\frac{\partial C_{ET}}{\partial z}=\frac{\partial C_{ET}}{\partial t} \tag{4.42}$$

For H_2O: $$D_{H2O}\frac{\partial^2 C_{H2O}}{\partial z^2}+\frac{D_{H2O}}{r}\frac{\partial\left(r\frac{\partial C_{H2O}}{\partial r}\right)}{\partial r}-u_z\frac{\partial C_{H2O}}{\partial z}=\frac{\partial C_{H2O}}{\partial t} \tag{4.43}$$

For C_3H_8: $$D_{C3H8}\frac{\partial^2 C_{C3H8}}{\partial z^2}+\frac{D_{C3H8}}{r}\frac{\partial\left(r\frac{\partial C_{C3H8}}{\partial r}\right)}{\partial r}-u_z\frac{\partial C_{C3H8}}{\partial z}=\frac{\partial C_{C3H8}}{\partial t} \tag{4.44}$$

For CO: $$D_{CO}\frac{\partial^2 C_{CO}}{\partial z^2}+\frac{D_{CO}}{r}\frac{\partial\left(r\frac{\partial C_{CO}}{\partial r}\right)}{\partial r}-u_z\frac{\partial C_{CO}}{\partial z}=\frac{\partial C_{CO}}{\partial t} \tag{4.45}$$

For CO_2: $$D_{CO2}\frac{\partial^2 C_{CO2}}{\partial z^2}+\frac{D_{CO2}}{r}\frac{\partial\left(r\frac{\partial C_{CO2}}{\partial r}\right)}{\partial r}-u_z\frac{\partial C_{CO2}}{\partial z}=\frac{\partial C_{CO2}}{\partial t} \tag{4.46}$$

For H_2: $$D_{H2}\frac{\partial^2 C_{H2}}{\partial z^2}+\frac{D_{H2}}{r}\frac{\partial\left(r\frac{\partial C_{H2}}{\partial r}\right)}{\partial r}-u_z\frac{\partial C_{H2}}{\partial z}=\frac{\partial C_{H2}}{\partial t} \tag{4.47}$$

Diffusion equation for gas phase mass transfer is as follows;

For $H_{2(g)}$:
$$D_{H2,G}\frac{\partial^2 C_{H2,G}}{\partial z^2}+\frac{D_{H2,G}}{r}\frac{\partial\left(r\frac{\partial C_{H2,G}}{\partial r}\right)}{\partial r}=\frac{\partial C_{H2,G}}{\partial t} \quad (4.48)$$

For $CO_{(g)}$:
$$D_{CO,G}\frac{\partial^2 C_{CO,G}}{\partial z^2}+\frac{D_{CO,G}}{r}\frac{\partial\left(r\frac{\partial C_{CO,G}}{\partial r}\right)}{\partial r}=\frac{\partial C_{CO,G}}{\partial t} \quad (4.49)$$

For $CO_{2(g)}$:
$$D_{CO2,G}\frac{\partial^2 C_{CO2,G}}{\partial z^2}+\frac{D_{CO2,G}}{r}\frac{\partial\left(r\frac{\partial C_{CO2,G}}{\partial r}\right)}{\partial r}=\frac{\partial C_{CO2,G}}{\partial t} \quad (4.50)$$

For $C_3H_{8(g)}$:
$$D_{C3H8,G}\frac{\partial^2 C_{C3H8,G}}{\partial z^2}+\frac{D_{C3H8,G}}{r}\frac{\partial\left(r\frac{\partial C_{C3H8,G}}{\partial r}\right)}{\partial r}=\frac{\partial C_{C3H8,G}}{\partial t} \quad (4.51)$$

For $H_2O_{(g)}$:
$$D_{H2O,G}\frac{\partial^2 C_{H2O,G}}{\partial z^2}+\frac{D_{H2O,G}}{r}\frac{\partial\left(r\frac{\partial C_{H2O,G}}{\partial r}\right)}{\partial r}=\frac{\partial C_{H2O,G}}{\partial t} \quad (4.52)$$

Boundary conditions

- At z = 0, $C_{H2}=0$
- At z = L, $\frac{\partial C_i}{\partial z}=0$
- At r = 0, $\frac{\partial C_i}{\partial r}=0$
- Consider a microreactor with the catalyst layer at the wall. Assuming the absence of any influence by internal mass transfer in the catalyst layer. All the reactant molecules transferred to the wall are consumed by the chemical reactions.

At r = R (wall), $$D_i \left.\frac{\partial C_i}{\partial r}\right|_{r=R} = \beta\, r_i \tag{4.53}$$

- Along the bubble surface Henry's law was used to take into account the discontinuous concentration of H_2 in the gas and liquid phases.

  $$C^*_{H_2(l)} = HeP_{H_2} \tag{4.54}$$

  Where C^*_{H2} is the equilibrium concentration of hydrogen at interface, P_{H2} is the partial pressure of hydrogen in gas phase and He is the equilibrium solubility of hydrogen in liquid phase.

4.2.6 COMSOL Multiphysics simulation

Momentum transfer and mass transfer equation were solved using Chemical reaction engineering module in COMSOL Multiphysics 4.1. Geometric parameter for gas bubble and liquid slug used in COMSOL modeling are shown in Table 4.4. Gas bubble and liquid slug length used in this simulation, were based on the numerical simulation with level set method. The gas bubble is formed in a micromixer at 50 °C and 500 psig, and then moves to a microreactor at a temperature range of 275-325 °C and 500 psig. Liquid slug was assumed to be long enough to support a stable liquid bridge between two consecutive gas bubbles and the gas bubbles do not interact with each other. The length of the gas bubble and the liquid slug at high temperature and pressure was calculated based on mass conservation equation. The thickness of the liquid film (δ) between the gas bubble and catalyst wall was estimated from Aussilous and Quere correlation [6].

$$\frac{\delta}{r} = \left[\frac{1.34\,Ca^{2/3}}{1+3.33\,Ca^{2/3}}\right] \tag{4.55}$$

A free mesh with triangular elements was used, while along the bubble interface the mesh was refined to capture the steep concentration gradient in that region.

Table 4.4 Geometric parameter for gas and liquid slug in COMSOL modeling (liquid flow rate = 0.1 ml/min, gas flow rate = 0.8 ml/min, system pressure = 500 psi, microchannel diameter = 500 μm).

Component	Temperature (°C)			
	50	**275**	**300**	**325**
5 wt% Oleic acid in dodecane/H_2 system				
Unit cell length, $L_{uc,}$ cm	7.07	11.64	12.17	12.71
Gas bubble length, L_g, cm	6.29	10.90	11.39	11.88
Liquid slug length, $L_{s,}$ cm	0.78	0.74	0.78	0.83
Liquid film thickness, δ, μm	-	3.4		
5 wt% Triolein in dodecane/H_2 system				
Unit cell length, $L_{uc,}$ cm	6.85	11.25	11.76	12.28
Gas bubble length, L_g, cm	6.19	10.62	11.1	11.58
Liquid slug length, $L_{s,}$ cm	0.66	0.63	0.66	0.70
Liquid film thickness, δ, μm	-	2.85		

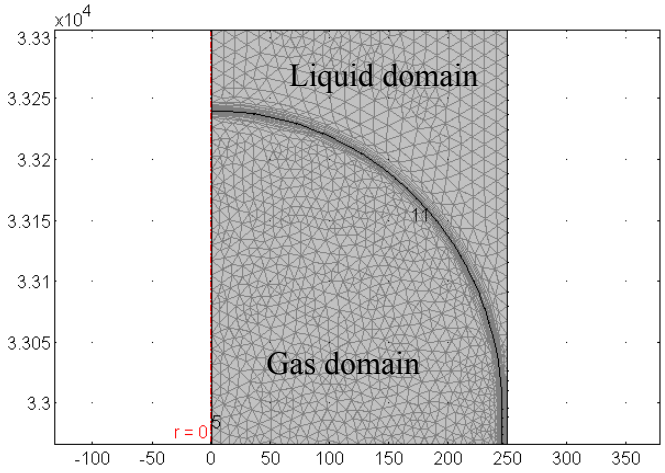

Figure 4.13 Mesh in gas domain, liquid domain and along the interface.

Simulation Conditions

There are two steps for solving the momentum transfer and mass transfer equations. Initially, the simulations were run in a steady-state mode to solve the continuity and incompressible Navier-Stokes equation in the liquid domain (Laminar flow node). The velocity field obtained from the first step was then used as a starting point to solve the convection-diffusion equation in the liquid and diffusion equation in the gas domains in transient mode simultaneously (Transport of diluted species node).

Boundary conditions

Boundary condition for flow field

For the flow field, the boundary conditions were assigned as follows. Gas bubble was kept stationary while the wall moved with the average velocity of fluids in the direction opposite to the flow. Axial symmetry was used at the central axis and free slip boundary was used along the bubble surface. The periodic boundary condition was used at the front and the back of the computational domain assuming that the inlet to the liquid slug is equal to the outlet.

Boundary condition for solving mass transport

For the mass transfer equations in the liquid domain, axial symmetry was used at the central axis and periodic boundary condition was used at the front and the back of the computational domain. Flux boundary condition was applied for mass transfer with chemical reaction at the reactor wall. For the mass transfer equations in gas domain, axial symmetry was used at the central axis. In addition, the concentration of reactant species were initialized at t=0 for gas and liquid domains. Along the bubble surface, we have continuity of the mass flux across the boundary but concentration is discontinuous. We must specify two separate concentrations, one in each region and then link the concentration together using equilibrium relationship. We also need to

force the flux to be continuous by declaring boundary conditions using the stiff-spring method [7]. The flux in the gas domain will be

$$-n \cdot N_i = -M\left(c_{H2,g} - \frac{c_{H2,l}}{He\,RT} \right) \tag{4.56}$$

The flux in the liquid domain would be

$$-n \cdot N_i = -M\left(\frac{c_{H2,l}}{He\,RT} - c_{H2,g} \right) \tag{4.57}$$

Where M is a large enough number to let the concentration differences in the brackets approach zero.

4.2.7 Residence time in microtube reactor

Residence time in the microtube reactor (5 m length) for 5 wt% of oleic acid in dodecane at 325 °C is estimated from the internal volume of the reactor (9.82×10^{-7} m^3) and the flow rate of gas and liquid phase at the reaction condition (500 psig, 325 °C).

The flow rate of H_2 gas at the reaction condition is calculated from that at the micromixer (0.8 ml/min at 50 °C and 500 psi). According to NIST database [8], density of H_2 is 2.5376 kg/m^3 at 50 °C and 500 psi and 1.3816 kg/m^3 at reaction condition. Thus the flow rate of H_2 at the reaction condition is 0.8 x 2.5376/1.3816 = 1.4694 ml/min.

The flow rate of liquid feed at the reaction condition is calculated from that at the pumping condition (0.1 ml/min at 50 °C). Density of liquid feed is 737.4 kg/m^3 at 50 °C and 500 psi and 502.7 kg/m^3 at reaction condition. Thus the liquid flow rate at reaction condition is 0.1 x 737.4/502.7 = 0.1467 ml/min.

The total flow rate of gas-liquid mixture at the reaction condition is 1.4694+0.1467 = 1.6161 ml/min (2.6935×10^{-8} m^3/s). The residence time in the reactor is the ratio of reactor volume and total flow rate of gas-liquid mixture at the reaction condition [9].

Consequently, the residence time in the reactor is 37 s. The residence time for oleic and triolein hydrotreating reactions are summarized in Table 4.5.

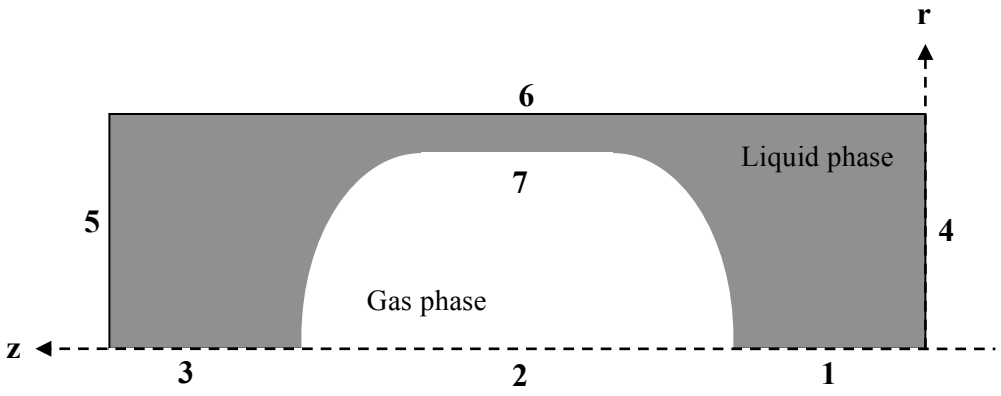

Boundary	Type	Equation
Boundary condition for flow field		
1,3	Axial symmetry	-
6	Moving wall	$u_Z = -u_{TP}$
4,5	Periodic flow	$u_{source} = u_{dest} \qquad p_{source} = p_{dest}$
7	Slip	$u \cdot n = 0$
Boundary condition for mass transport in liquid phase		
1,3	Axial symmetry	-
6	Flux	$-n \cdot N_i = r_i$
4,5	Periodic condition	$c_{i,source} = c_{i,dest}$
7	Flux	$-n \cdot N_i = -M\left(\frac{c_{H2,l}}{He\,RT} - c_{H2,g}\right)$
Boundary condition for mass transport in gas phase		
2	Axial symmetry	-
7	Flux	$-n \cdot N_i = -M\left(c_{H2,g} - \frac{c_{H2,l}}{He\,RT}\right)$

Figure 4.14. Boundaries for the modeled system.

Table 4.5 Residence time for oleic acid and triolein hydrotreating at 500 psi, total microtube length of 5 m.

	Temperature (°C)			
	50	**275**	**300**	**325**
Reactor volume (m^3)	9.8175×10^{-7}			
H_2 density (kg/m^3)	2.5376	1.5061	1.4412	1.3816
H_2 flow rate (ml/min)	0.8	1.3479	1.4086	1.4694
Oleic acid hydrotreating system				
Liquid density (kg/m^3)	737.4	557.2	531.3	502.7
Liquid flow rate (ml/min)	0.1	0.1323	0.1388	0.1467
Total flow rate (ml/min)	0.9	1.4802	1.5474	1.6161
Residence time (s)	-	40	38	37
Triolein hydrotreating system				
Liquid density (kg/m^3)	738	556.3	530.1	501.3
Liquid flow rate (ml/min)	0.1	0.1327	0.1392	0.1472
Total flow rate (ml/min)	0.9	1.4806	1.5478	1.6166
Residence time (s)	-	40	38	36

4.2.8 Numerical results for fluid flow and mass transfer without chemical reaction

Fluid flow

The flow field was solved under steady state and the simulated snapshot of steady state velocity profile in liquid slug is shown in Figure 4.15. The velocity field and streamline plot showed that the internal circulations formed inside liquid slug. The re-circulation was symmetrical to the channel center and the maximum velocity at the centerline.

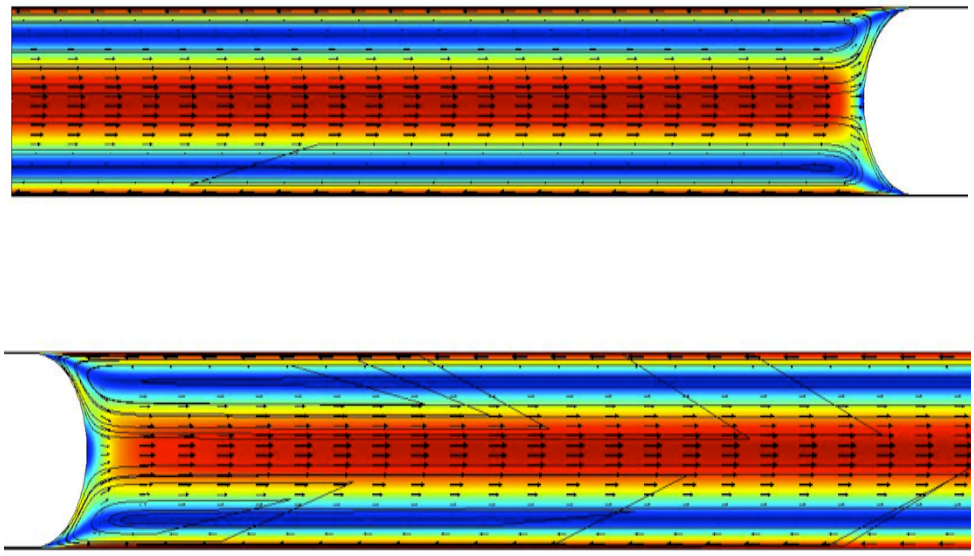

Figure 4.15 Velocity profile in liquid slug.

Mass transfer

Mass transfer by purely diffusion (no velocity field assumed) and by diffusion and convection (velocity field assumed) was studied. The concentration profiles were obtained by solving diffusion equation only and also the diffusion and convective equations. The results of concentration distribution (diffusion only) of H_2 in liquid phase is shown in dotted line in Figure 4.16. Solid line is concentration distribution of

H_2 in liquid phase with the mass transfer by diffusion and convection without chemical reaction. These results showed that rapid mixing is obtained when velocity is applied to the moving wall. H_2 is transported due to the diffusion across the interface and keeps on recirculating due to the formation of internal circulation within liquid slugs.

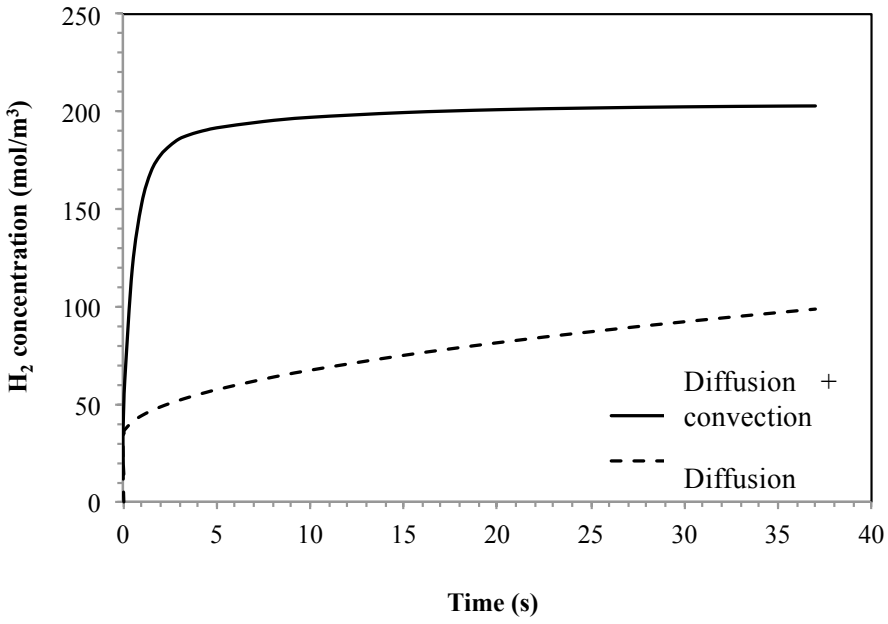

Figure 4.16 Effect of moving wall velocity on H_2 concentration in liquid phase.

4.3 References

[1] Ilnicki, F., Sobieszuk, P. and Pohorecki, R., 2009, Simulations of a two phase flow in a closed microchannel, Chemical and process engineering, 30, 205-216.

[2] McDevitt, M.R., Hitt, D.L. and McCabe, J.W., 2010, Study of Two-Phase Microslug Formation in a Microchannel Cross Junction, Proceedings of the COMSOL Conference 2010 Boston.

[3] Hubber G. W., Connor P. O and Corma A., 2007, Processing in conventional oil refineries: Production of high quality diesel by hydrotreating vegetable oils in heavy vacuum oil mixtures, Applied catalysis A: General, 329, 120-129.

[4] Kubicka D., Bejblova M. and Vlk J., 2010, Conversion of vegetable oils into hydrocarbons over CoMo/MCM-41 catalysts, Top Catal, 53, 168-178.

[5] Shao, N., Gavriilidis, A., Angeli, P., 2010, Mass transfer during Taylor flow in microchannels with and without chemical reaction, Chemical Engineering Journal, 160, 873-881.

[6] Aussillous, P. and Quere, D., 2000, Quick deposition of a fluid on the wall of a tube, Physics of Fluids, 12 (10), 2367-2371.

[7] Separation through dialysis solved with FEMLAB 3, COMSOL

[8] Thermophysical properties of fluid systems, NIST Chemistry WebBook, http://webbook.nist.gov./chemistry/fluid/.

[9] Takebayashi, Y., Sue, K., Yoda, S., Furuya, T., Mae, K., 2012, Direct carbonylation of nitrobenzene to phenylisocyanate using gas–liquid slug flow in microchannel, Chemical Engineering Journal, 180, 250–254.

CHAPTER 5

EXPERIMENTAL APPARATUS AND METHOD

This chapter presents the experimental apparatus and the operating procedure for a typical hydrotreating experiment. The objective of the experiments is to obtain oil conversion and product distribution from hydrotreating reactions at different experimental conditions. The experimental conditions were varied to achieve reasonable conversions in order to use the results for process kinetics parameter estimation. Oleic acid was used as a model compound for fatty acid hydrotreating reaction. Triolein was hydrotreated in order to model hydrotreating of normal vegetable oils as this molecule shares the main characteristics of the naturally occurring triglycerides.

5.1 Material

The chemicals and gases that were used are list in Table 5.1. All chemicals were used as received without further purification.

Table 5.1 Gases and chemicals.

Chemical	Supplier	Purity
Oleic acid	Alfa aesar	Technical grade with 90% purity
Triolein	TCI America	Min 80.0%
Jatropha oil	N/A	N/A
Dodecane	Acros organics	Mixture of isomers
Hydrogen	Air gas	ultra-high purity
Nitrogen	Air gas	ultra-high purity
Helium	Air gas	ultra-high purity
Argon	Air gas	ultra-high purity

5.2 Experimental apparatus

The main component of the experimental setup included gas and liquid delivery system, gas/liquid microchannel mixer, microreactor, heat exchanger and backpressure regulator. The schematic of the hydrotreating system is presented in Figure 5.1. The liquid delivery system consisted of HPLC (high performance liquid chromatography) pump (Series III pump, Chrom Tech, Inc., U.S.A.) that delivered liquid feed to the gas/liquid microchannel mixer. The gas delivery system consisted of a critical flow orifice with 3 μm hole that establish the required flow rate of H_2 gas to the system.

From the gas/liquid micromixer, the mixture of gas and liquid reactant flows through a high-pressure stainless steel line to a 316 stainless steel coil shaped continuous flow microreactor coated with the catalyst. The development and characterization of catalyst coating inside microreactor is previously described in Chapter 3. The reactor was heated with an electric heater. The effluent exiting the microreactor was cooled down in heat exchanger with water as the coolant. The outlet line was maintained at temperature above 60 °C to prevent any solidifying of the product in the line. The elevated temperature was provided with heat tape controlled by manual rheostats. The effluent was passed through an in-line filter to remove any large particles and then the pressure was decreased to ambient pressure by backpressure regulator. The liquid product was collected for further analysis.

System pressure was monitored at three different locations; at HPLC pump, before the gas/liquid micro mixer and before the backpressure regulator. The temperature reading was taken at heater plate below the reactor and at the reactor wall.

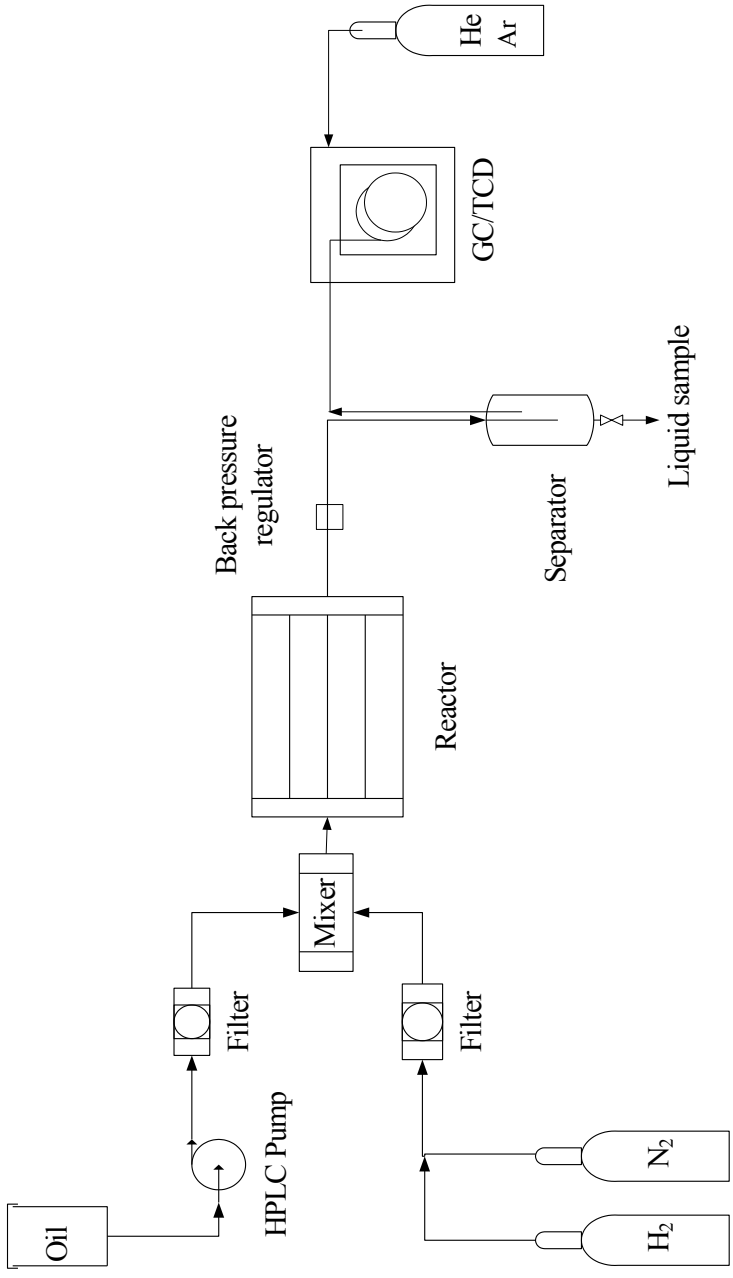

Figure 5.1 Schematic of the hydrotreating system.

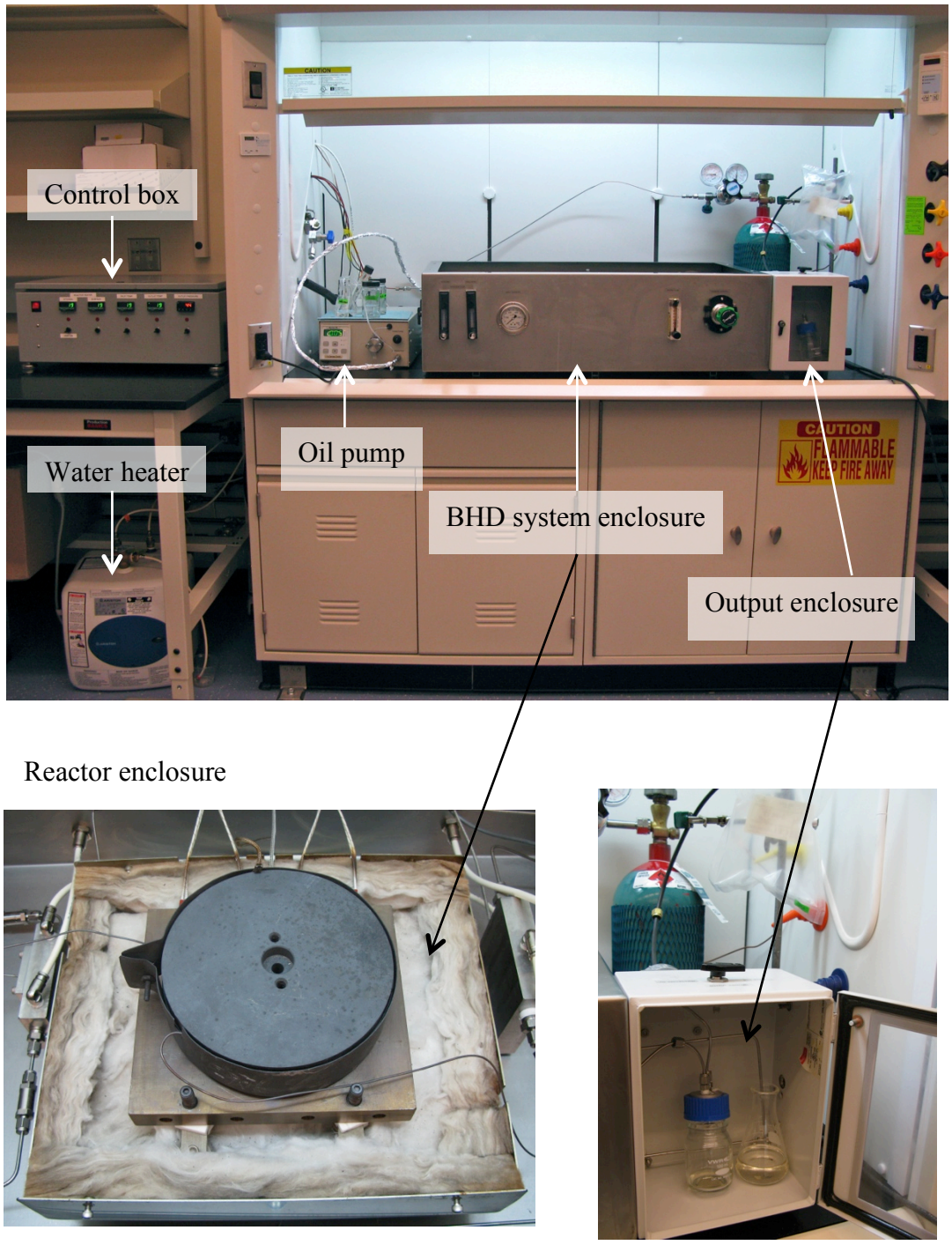

Figure 5.2 Photograph of experimental set-up for hydrotreating reaction.

Figure 5.2 shows a photograph of the experimental set-up. Oil feed pump can be seen in the center of the photograph, whereas the metallic box right of the feed pump contains the gas/liquid micromixer, microtubular reactor and process line. H_2 gas cylinder and output enclosure can be seen in the right part of the photograph. Control box and water heater can be seen in the left part of the photograph.

Following is a detailed description of the main components of the system.

5.2.1 Gas-liquid microchannel mixer

Gas liquid microchannel mixer was used to create gas-liquid segmented flow in the microchannels by using buoyancy force and surface tension to generate a gas bubble in the liquid. The mixer was made from 316 stainless steel plate with 50 mm x 50 mm in size and the design was shown in Figure 5.3.

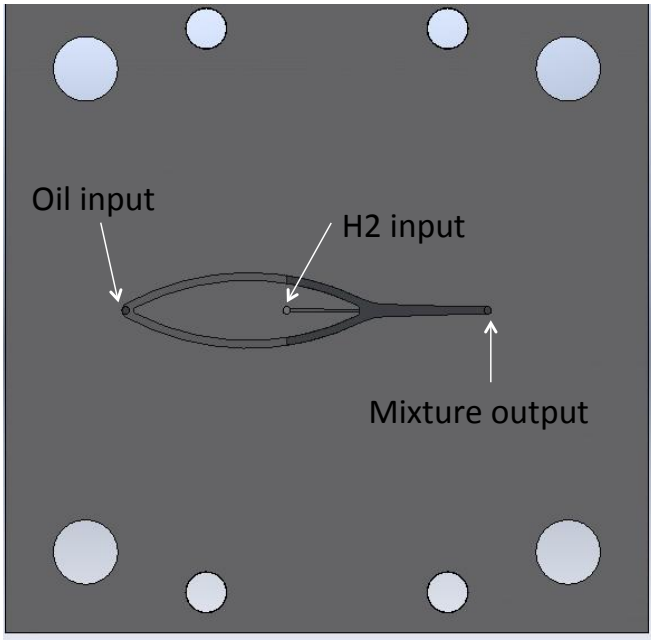

Figure 5.3 Geometry of gas/liquid microchannel mixer.

The liquid flow was split into two equal flows and then contacted with the gas flow through the micro orifice. The mixer then focuses the flow into 500 μm circular cross sectional tubing. It is heated to 50 °C using water to stabilize the temperature for bubble generation and to keep the liquid feed above the cloud point.

5.2.2 Microreactor

The experimental microreactor was a stainless steel microtubular reactor. The microreactor has an inner diameter of 500 μm, an outer diameter 1/16 inch and a total length of 1.5-5 m. This dimensions resulted in a total available reactor volume in the range of $2.95x10^{-7}$ - $9.82x10^{-7}$ m^3. The core of reactor block was made from stainless steel cylindrical block that had a diameter of 15 cm and 8 cm height. The stainless steel tubing was coiled around the reactor core and the outer stainless steel plate was cover around the tubing.

5.3 Experimental method

5.3.1 Startup procedure

The following procedure outlines the reactor start up for each experiment. First, the water heater for the heat exchanger was turned on and the temperature was set at 50 °C. Nitrogen was used to flow through the system during startup. The reactor heater system was turned on and the temperature adjusted to 100 °C. Once the system temperature had reached the set point, the liquid feed pump was turned on and the flow rate adjusted to 0.1 ml/min. The backpressure regulator was adjusted to the desired pressure. The pressure gauge before the backpressure regulator and the pressure gauge at the pump were compared to determine if clogging was present in the system. Once the system pressure reached the desired value, the reactor temperature was adjusted to desired experimental value and the liquid feed pump was set to desired experimental flow rate. N_2 was switched to H_2 and the system was allowed to stabilize for 2 h before the sample was collected for analysis.

5.3.2 Experimental condition

The reactions were performed using 5 % wt of oleic acid in dodecane, 5 % wt of triolein in dodecane, 5 wt% of jatropha oil in dodecane, pure oleic acid and jatropha oil by varying the temperature in the range of 275-325 °C and microtube length in the range of 1.5-5 m. The H_2 tank pressure was kept at 1200 psi (equivalent to volumetric H_2 gas flow rate of 0.8 ml/min). The liquid flow rate used was 0.1 ml/min (Table 5.2 and Table 5.3). The system pressure was kept constant at 500 psig.

The experiment was run for various lengths of time depending on the time that was required for study. Microtube reactor coated with fresh catalyst was prepared and used for each run.

Table 5.2 Experimental conditions for oleic acid hydrotreating.

Liquid Feed	Temperature (°C)	Microtube length (m)
5 wt% Oleic acid in dodecane	275	1.5, 3.5, 5
5 wt% Oleic acid in dodecane	300	1.5, 3.5, 5
5 wt% Oleic acid in dodecane	325	1.5, 3.5, 5
Oleic acid	325	5

Table 5.3 Experimental conditions for triolein and jatropha oil hydrotreating.

Liquid Feed	Temperature (°C)	Microtube length (m)
5 wt% Triolein in dodecane	275	5
5 wt% Triolein in dodecane	300	5
5 wt% Triolein in dodecane	325	1.5, 3.5, 5
5 wt% Jatropha oil in dodecane	325	5
Jatropha oil	325	5

5.3.3 Shut down procedure

At the end of experiment the reactor was shut down by the following procedure. First, the H_2 flow was switched to N_2 flow. The reactor heater system was turned off. Once the temperature decreased below 100 °C, the liquid feed pump was turned off and the system pressure was stepped down to ambient pressure by adjusting the backpressure regulator. Nitrogen flow and water flow was then turned off.

5.4 Product analysis

5.4.1 Liquid product analysis

The liquid product was collected, weighted and then analyzed by Gas Chromatograph (GC) for its composition of triglyceride, fatty acids, oxygenated intermediates and alkanes. The analyses were performed with Perkin Elmer Clarus 500, Gas chromatograph with autosampler and flame ionization detector (FID). Restek MXT biodiesel TG column with 100% dimethyl polysiloxane stationary phase was used for the analysis. The column has 14 m in length, with 0.53 mm internal diameter and 0.16 um film thickness. The unconverted triglyceride, oleic acid and intermediates were silylated by N-Methyl-N-(trimethylsilyl)trifluoroacetamide (MSTFA) before analysis. Silylation converts fatty acid to trimethylsilyl esters to make them sufficiently volatile for analysis. Tricaprin was used as an internal standard in order to quantify the concentration of reactants. A detailed procedure of this analysis is found in Appendix A.

The possible leaching of NiMoP metal catalyst in liquid product was determined by an inductively coupled plasma atomic emission spectroscopy (ICP-AES). Approximately 0.2 g of liquid sample, 5 ml of HNO_3 (65 wt% purity) and 1 ml of H_2O_2 (30 wt% purity) were added and heated. The samples were diluted to 100 ml and then analyzed using a Varian Vista Pro ICP-AES instrument.

5.4.2 Gaseous product analysis

In selected experiments, the gas samples from gas outlet stream of the reactor were qualitatively analyzed off-line using Agilent Micro-GC 3000. Channel A incorporates a molecular sieve capillary column (10 m) with thermal conductivity detector (TCD) and back flush injector. Argon is the carrier gas for this column. It can analyze H_2, CH_4 and CO. Channel B incorporates a Plot U capillary column (8 m) with thermal conductivity detector (TCD) and variable volume injector. Helium is the carrier gas for this column and it can analyze CO_2, CH_4, ethane and higher hydrocarbons. Channel C incorporates an OV1 column (8 m) with thermal conductivity detector (TCD) and fixed volume injector. Helium is the carrier gas for this column and it can analyze higher hydrocarbons.

5.5 Definition and calculation

As the main objective of this study is deoxygenation, saturation of double bonds in both triglyceride and fatty acid are not considered as their conversion. The total amount of saturated and unsaturated triglyceride and fatty acids were combined and considered as one component. Conversion (X) is calculated as the ratio of amount of consumed reactant to amount of initial reactant. Thus, complete conversion is achieved when no reactant is detected in a reaction mixture.

$$X = \frac{F_{i,0} - F_{i,t}}{F_{i,0}} \times 100\% \qquad (5.1)$$

Where F_0 and F_t is the molar flow rate at the inlet and outlet of the reactant, respectively.

Molar concentration of liquid product i was calculated from the analyzed liquid sample. It was the number of moles of product i divided by the total number of moles of all compounds in the product multiplied by 100%.

$$i-composition(\%)=\frac{C_i}{C_{all}}\times 100 \tag{5.2}$$

Alkanes and alkenes are summed together and referred as hydrocarbon products. The reaction products containing oxygen are referred as oxygenated products. Hydrodeoxygenation of triglyceride and fatty acid were defined as the fraction of the reactant converted to hydrocarbons. Thus, complete deoxygenation is achieved when compounds containing only hydrocarbons are present in reaction mixture.

$$HDO(\%)=\left[\frac{T_{feed}-T_{product}}{T_{feed}}\right]\times 100 \tag{5.3}$$

Where T_{feed} and $T_{product}$ were the composition of the total oxygenated compounds determined by gas chromatograph analysis of the feed and product streams respectively.

CHAPTER 6

EXPERIMENTAL RESULTS AND DISCUSSION

6.1 Oleic acid hydrotreating

6.1.1 Product composition and reaction pathway

The catalytic hydrotreating of 5wt.% oleic acid ($C_{17}H_{33}COOH$) in dodecane ($C_{12}H_{26}$) was studied in continuous flow microtubular reactor over washcoat $NiMoP/Al_2O_3$ catalyst at 500 psig, 37-40 s residence times, 275-325 °C reaction temperatures and 80 mol H_2/mol oleic acid feed ratio. The steady state composition of liquid product over time on stream is shown in Figure 6.1. At 325 °C, oleic acid deoxygenation proceeded well and the compositions of product were fairly constant during the first 10 h time on stream. The liquid product obtained was heterogeneous colorless liquid with fine white solid at room temperature. However, it became a clear homogeneous liquid at the temperature above 50 °C. The reaction product consisted of hydrocarbons and oxygenated compounds including saturated fatty acids, fatty alcohol and long chain fatty esters.

The presence of fatty alcohol was expected, as it is an intermediate of fatty acid hydrogenation reaction. Long chain fatty ester is the products of esterification reaction between fatty acids and fatty alcohols. The formation of fatty alcohol and long chain ester as the intermediates during vegetable oil hydrotreating was also reported by Kubicka et al [1], who studied the hydrotreating of vegetable oil over sulfide $NiMo/Al_2O_3$ catalyst.

As shown in Figure 6.1, the amount of fatty alcohol and long chain ester increased, while the concentration of hydrocarbon decreased with a decreasing temperature from 325 to 300 °C. This was due to the decreasing of hydrotreating reaction of oxygenated

compounds. Thus, large amount of oxygenated intermediate remained in the product. The increase was, however, followed by a decrease of fatty alcohol and long chain ester and decrease in concentration of hydrocarbon at 275 °C. This can be attributed to the hydrotreating reaction of fatty acid and fatty alcohol that did not proceed well. Less fatty alcohol was formed and consequently hydrocarbon could not be formed either. In addition, it was observed that most of the fatty acid found in liquid product in all experiments was stearic acid, which indicated that the saturation of double bond in oleic acid to give stearic acid was rapid in this study.

The Gibbs free energies at 300 °C for hydrodeoxygenation and decarboxylation of stearic acid are -86.1 and -83.5 kJ/mol respectively. While, the Gibbs free energy of decarbonylation is less negative with the value of -17 kJ/mol at 300 °C [2] These thermodynamics data support that these three reactions can occur at the reaction condition used in current work. However, the product distribution would be effected by type of catalyst as also suggested by Madsen et al. [3].

Table 6.1 Thermodynamics of hydrodeoxygenation, decarboxylation and decarbonylation of stearic acid at 300 °C [2].

Reaction	$\Delta G_{300^{\circ}C}$ **(kJ/mol)**
Hydrodeoxygenation: $C_{18}H_{36}O_2 + 3H_2 \longrightarrow 2H_2O + C_{18}H_{38}$	-86.1
Decarboxylation: $C_{18}H_{36}O_2 \longrightarrow CO_2 + C_{17}H_{36}$	-83.5
Decarbonylation: $C_{18}H_{36}O_2 \longrightarrow CO + H_2O + C_{17}H_{34}$	-17.0

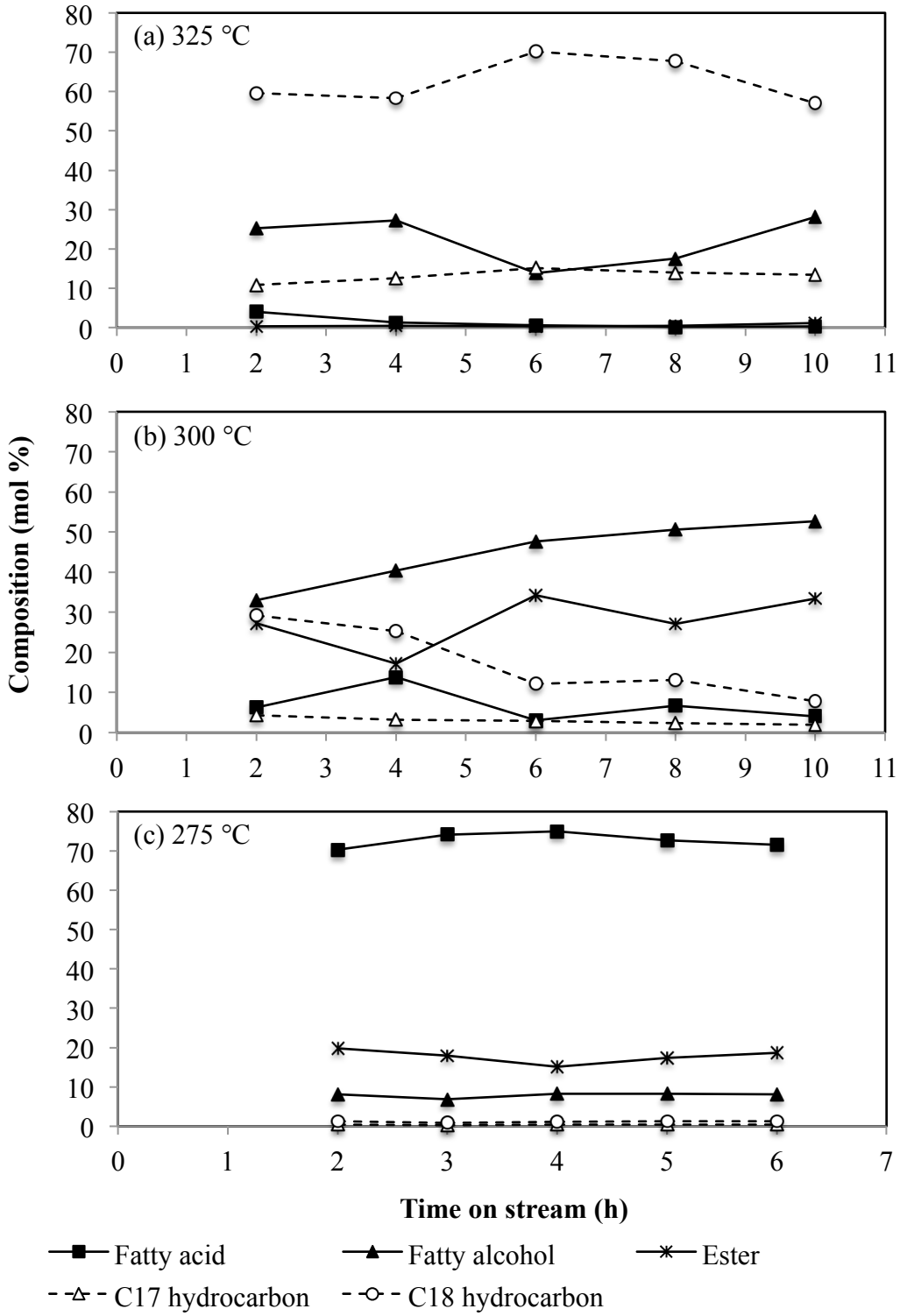

Figure 6.1 Reactant and product distribution profile of oleic acid hydrotreating at reaction temperature of (a) 325 °C, (b) 300 °C and (c) 275 °C. The reaction conditions: p=500 psig, $C_{fatty\ acid}$= 0.13 mol/l and residence time = 37-40 s.

The presence of fatty alcohol as an intermediate and C_{18} hydrocarbon as main hydrocarbon in liquid product suggesting that hydrodeoxygenation is the main reaction pathways in oleic acid hydrotreating over $NiMoP/Al_2O_3$ catalyst. The presence of heptadecane as a minor hydrocarbon in liquid product indicated that the decarbonylation and decarboxylation reaction of oleic acid also occurred but to a smaller extent. To investigate the selectivity of decarbonylation-decarboxylation to hydrodeoxygenation, the ratio of C_{17} hydrocarbon in the total amount of C_{17} and C_{18} hydrocarbon ($C_{17}/(C_{17}+C_{18})$) was calculated and the result is shown in Figure 6.2. The result indicated that $NiMoP/Al_2O_3$ catalyst favors the hydrodeoxygenation to C_{18} hydrocarbon.

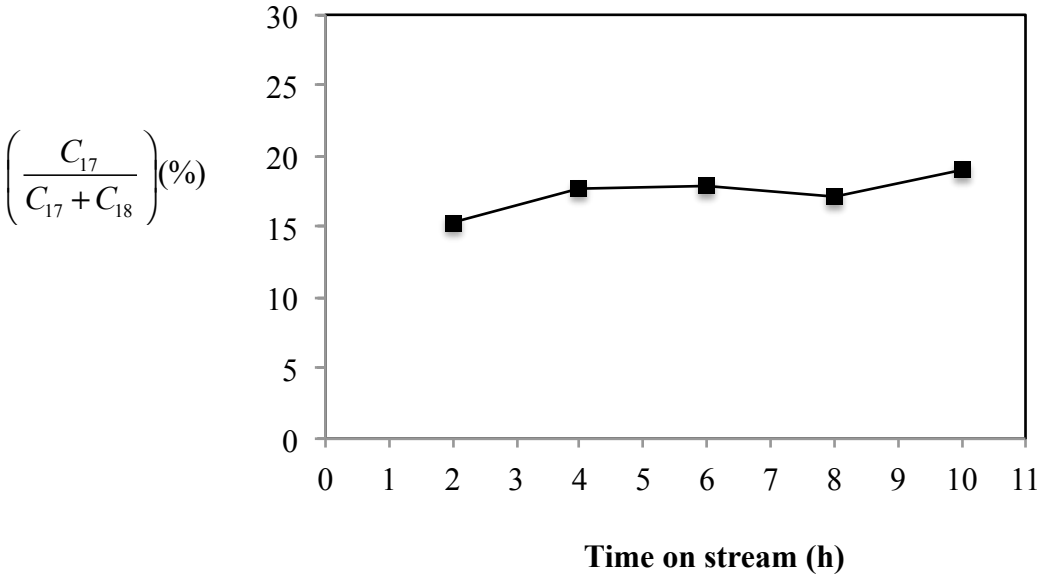

Figure 6.2 The ratio of $C_{17}/(C_{17}+C_{18})$ in liquid product for oleic hydrotreating. The reaction conditions: p=500 psig, $C_{fatty\ acid}$= 0.13 mol/l, T=325 °C and residence time = 37 s.

The off-line gaseous phase analysis showed that remaining hydrogen was the main component in gaseous sample, due to the large excess amount of hydrogen used in the

reaction. Carbon dioxide, carbon monoxide, methane, ethylene, ethane and propane were detected in the gaseous product. The presence of carbon dioxide and carbon monoxide confirmed that the decarbonylation and decarboxylation reaction of oleic acid occurred.

NiMo catalyst was also known to be active for water gas shift reaction [4]. It can thus be suspected that the presence of carbon dioxide could also be due to the water gas shift reaction (6.1), in which carbon monoxide and water are transformed into carbon dioxide and hydrogen. The presence of methane in gaseous product was probably due to the methanation reaction of both carbon monoxide (6.2) and carbon dioxide (6.3) with hydrogen at reaction condition used in this study, as also suggested by Madsen et al. [3]. The formation of short-chained hydrocarbons was probably due to a catalytic reaction that combines fragmented hydrocarbons from the C-C and C-O bond breaking and hydrogen on the catalyst surface.

Water gas shift reaction: $$CO + H_2O \longleftrightarrow CO_2 + H_2 \quad (6.1)$$

Methanation: $$CO + 3H_2 \longleftrightarrow CH_4 + H_2O \quad (6.2)$$

$$CO_2 + 4H_2 \longleftrightarrow CH_4 + 2H_2O \quad (6.3)$$

On the basis of the detected liquid and gaseous products, a simplified scheme showing how fatty acid was transformed to hydrocarbon was suggested and presented in Figure 6.3. The scheme showed that oleic acid was first hydrogenated to stearic acid, which was then converted into alkanes by two different pathways:

(1) Hydrodeoxygenation.

(2) Decarbonylation and decarboxylation.

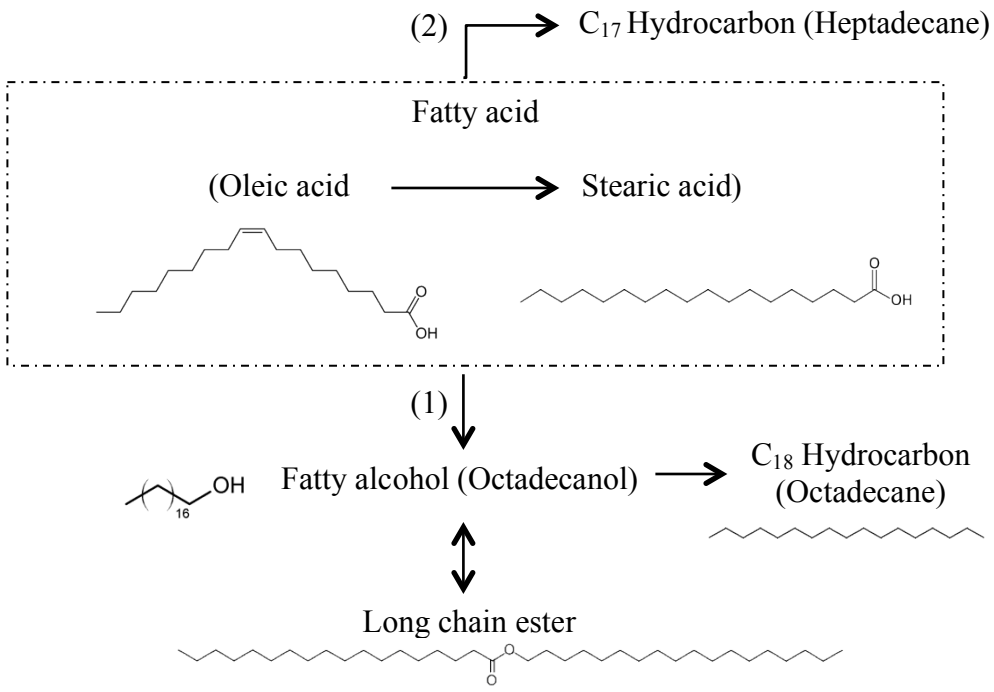

Figure 6.3 A reaction pathway for hydrotreating reaction of oleic acid.

6.1.2 Effect of reaction temperature

Figure 6.4 shows the effect of the reaction temperature on oleic acid hydrotreating in the temperature range of 275-325 °C. %Hydrodeoxygenation and fatty acid conversion increased with increasing temperature. At reaction temperature above 300 °C, the conversion of fatty acid exceeded 95%. However, %hydrodeoxygenation was lower, 20.47 and 75.79% at 300 and 325 °C respectively, due to the presence of oxygenated intermediate compounds in the liquid product. Lower fatty acid conversion (44.91%) was obtained at 275 °C.

The repeated experiment with 5 wt.% oleic acid at 325 °C showed that the experiments were well reproducible. Fatty acid conversion and %hydrodeoxygenation

values varied by 0.1 and 5% respectively. Carbon balance was calculated based on liquid product analyses and it was above 89% at 275 °C.

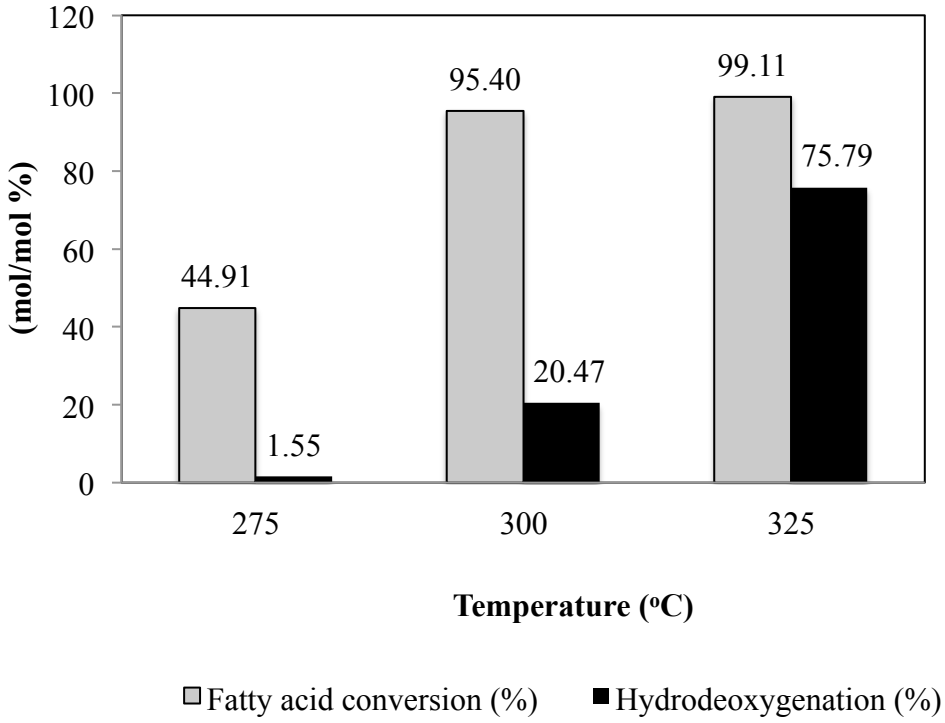

Figure 6.4 Fatty acid conversion and %hydrodeoxygenation of oleic acid hydrotreating. The reaction conditions: p=500 psig, $C_{fatty\ acid}$= 0.13 mol/l and residence time = 37-40 s.

6.1.3 Effect of residence time

Figure 6.5 shows the effect of the residence time on the composition of liquid product in the hydrotreating of oleic acid over NiMoP/Al_2O_3 catalyst at 325 °C during 10 h time on stream. The compositions of liquid product were almost constant during 10 h time on stream for each residence times in this study.

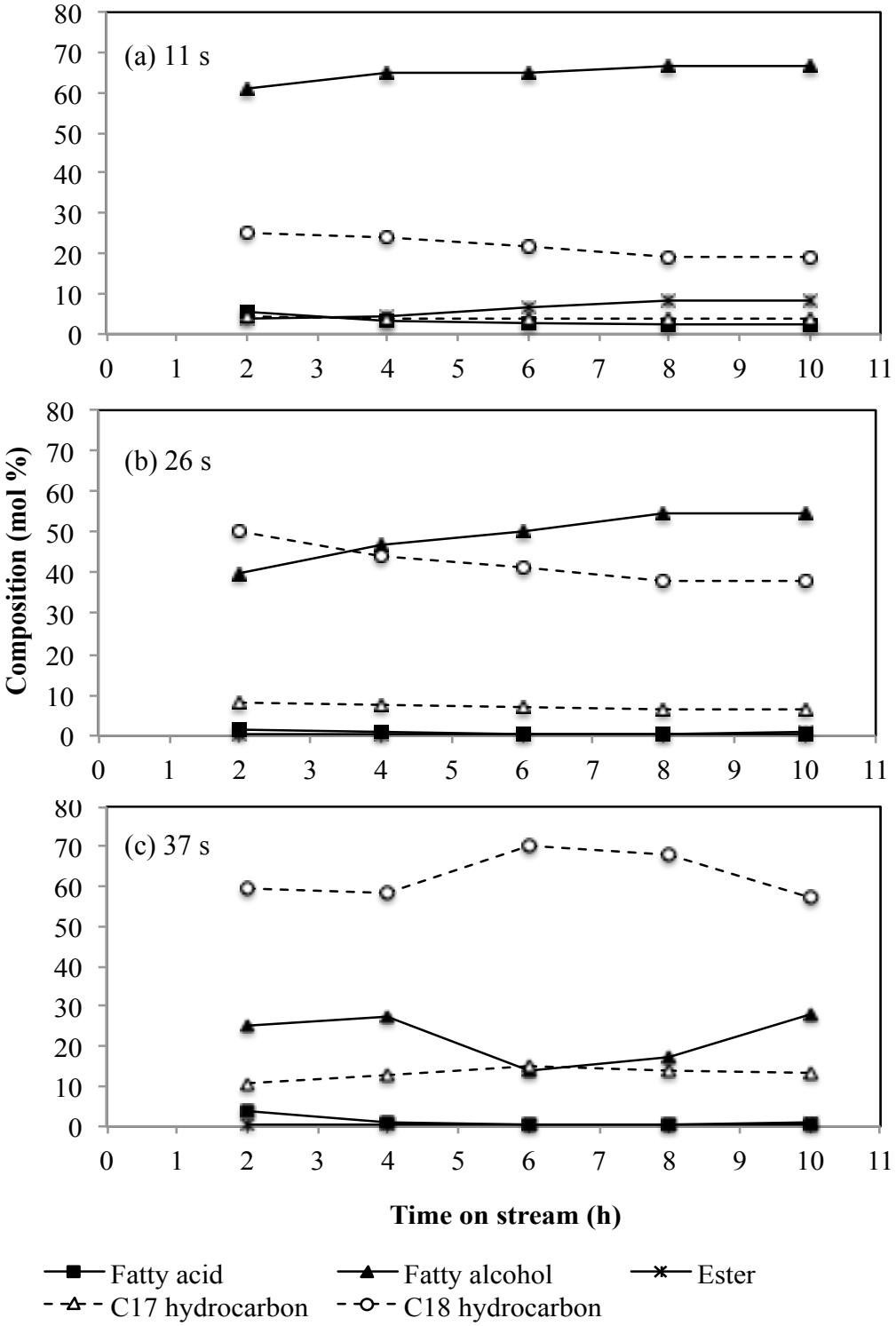

Figure 6.5 Reactant and product distribution profile of oleic acid hydrotreating at residence time of (a) 11 s (b) 26 s and (c) 37 s. The reaction conditions: T= 325 °C, p=500 psig and $C_{fatty\ acid}$= 0.13 mol/l.

Composition of liquid products changed as a function of residence time as shown in Figure 6.6. Most of fatty acid composition disappeared and fatty alcohol was the main liquid product from the hydrotreating reaction of oleic acid at 11 s residence times. The amount of C17 and C18 hydrocarbon increased, while the concentration of fatty alcohol decreased with an increasing residence time from 11 to 37 s. This was due to the increased hydrotreating reaction of the oxygenated compounds.

As seen in Figure 6.7 total fatty acid conversion reached 97% at 11 s residence times. While %hydrodeoxygenation was only 26.5% due to the presence of high amount of oxygenated intermediate compounds. %Hydrodeoxygenation increased with increasing residence time. It increased from 49.4 % to 75.8 % when the residence time increased from 26 to 37 s.

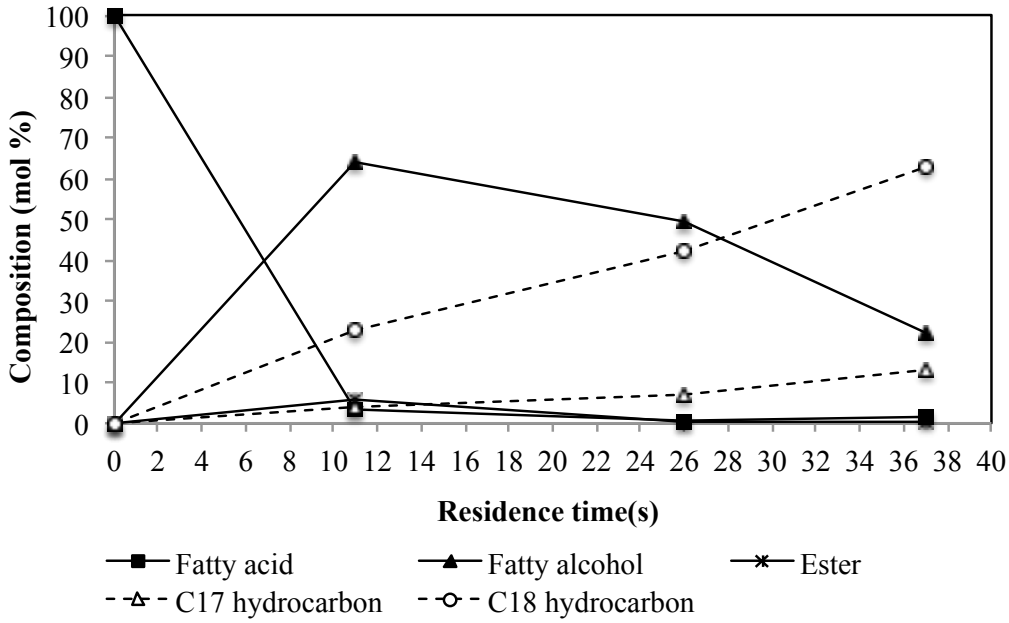

Figure 6.6 Effect of residence time on product distribution of oleic acid hydrotreating. The reaction conditions: T= 325 °C, p=500 psig and $C_{fatty\ acid}$= 0.13 mol/l.

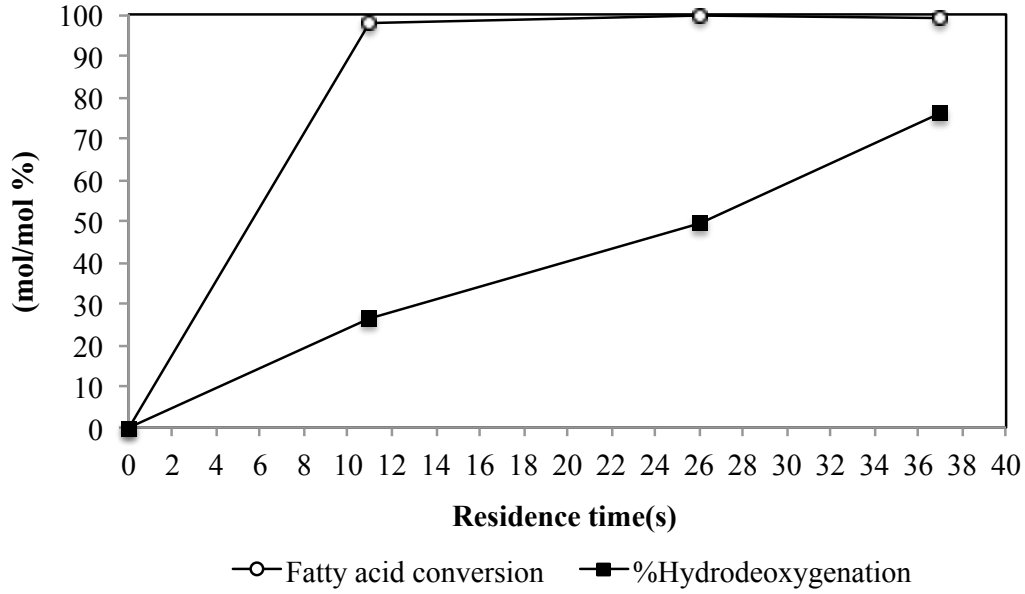

Figure 6.7 Effect of residence time on fatty acid conversion and %hydrodeoxygenation of oleic acid hydrotreating. The reaction conditions: T = 325 °C, p=500 psig and $C_{fatty\ acid}$= 0.13 mol/l.

6.1.4 Catalyst stability

Long duration performance test was done for oleic acid hydrotreating over washcoat $NiMoP/Al_2O_3$ catalyst at 500 psig pressure, 37 s residence times, 325 °C reaction temperatures and 80 mol H_2/mol oleic acid feed ratio. As the time-on-stream increased, the concentration of fatty alcohol slightly increased first and large amount of long chain ester was observed (Figure 6.8). At longer time on stream, the concentration of fatty alcohol decreased, concentration of hydrocarbon product decreased and the fatty acid was the main component in the reaction product. The changes in intermediates reflect the gradual deterioration of catalyst activity. Fatty acid conversion dropped from 99% at time on stream of 16 h to 23 % at time on stream of 26 h as shown in Figure 6.9.

Catalyst deactivation within a short time on stream is common for fatty acid deoxygenation reaction. A severe catalyst deactivation within the first 20-30 min time on stream was observed by Maki-Arvela et al. [5], when performing the continuous deoxygenating of diluted lauric acid over a microporous commercial Pd/C catalyst in fixed bed reactor.

When fatty acid is hydrotreated on a $NiMoP/Al_2O_3$ catalyst, the loss in the performance of the catalyst could be occurring for a number of reasons, for example:

(1) Catalyst leaching

(2) Catalyst fouling from the formation of coke and formation of high molecular weight deposits from the oxygen-containing molecules

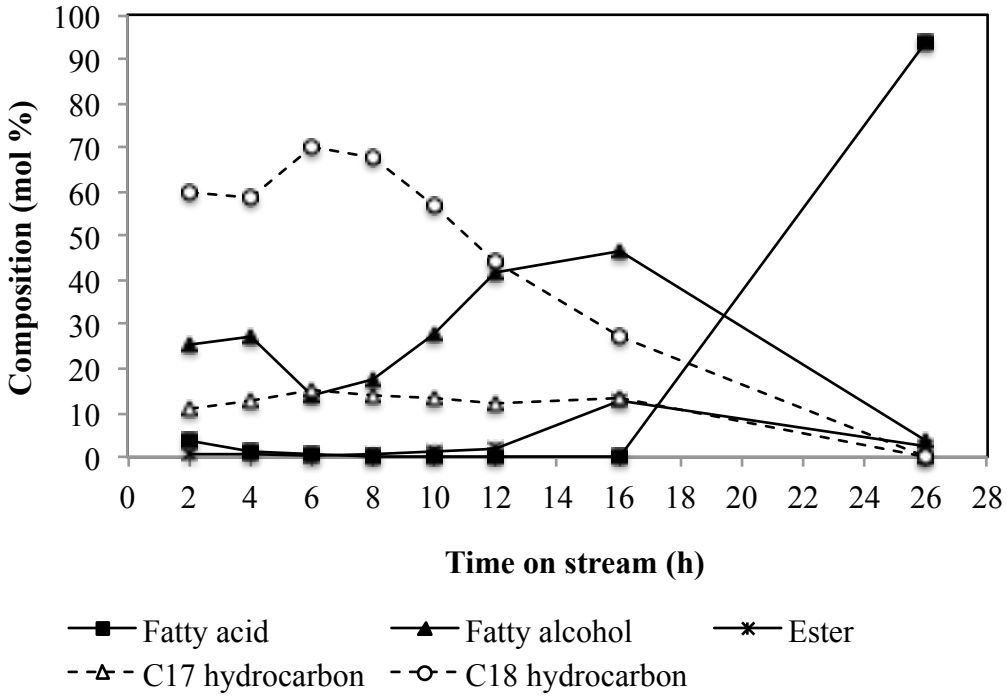

Figure 6.8 Reactant and product distribution profile of oleic acid hydrotreating at long duration time. The reaction conditions: T= 325 °C, p=500 psig, $C_{fatty\ acid}$= 0.13 mol/l and residence time = 37 s.

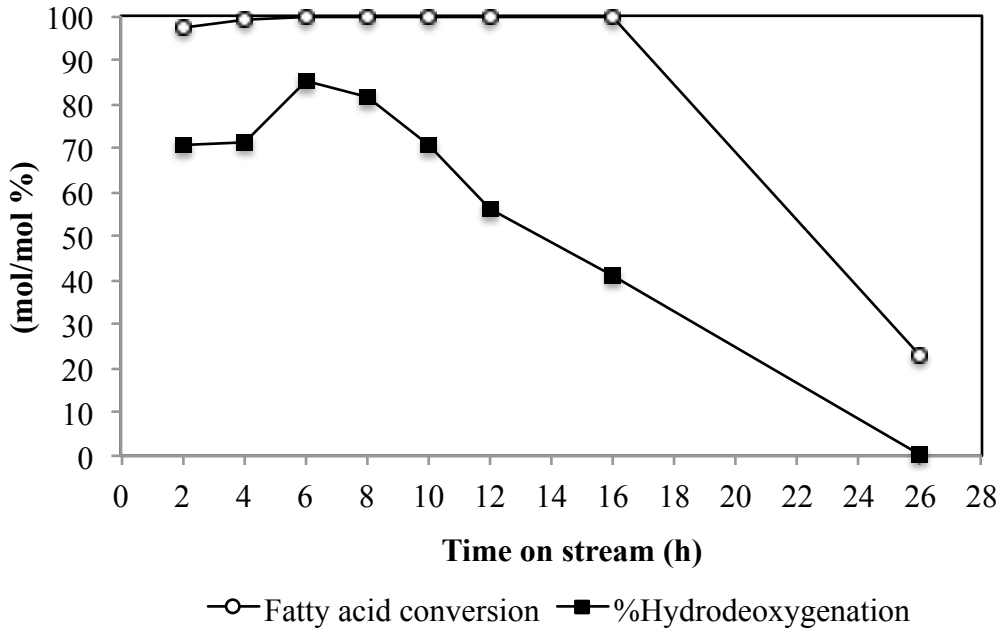

Figure 6.9 Fatty acid conversion and %hydrodeoxygenation of oleic acid hydrotreating at long duration time. The reaction conditions: T= 325 °C, p=500 psig, $C_{fatty\ acid}$= 0.13 mol/l and residence time = 37 s.

The possibility of metal catalyst leaching from washcoat catalyst layer was investigated by analyzing liquid product by inductively coupled plasma atomic emission spectroscopy (ICP-AES). The results showed that there was no significant amount of Ni, Mo, Fe and Al component detected in liquid product. These results confirmed that metal leaching from washcoat catalyst was negligible during the continuous hydrotreating of oleic acid at reaction conditions used in current work. Thus, the cause of catalyst deactivation was suggested to be coking.

6.1.5 Effect of hydrogen

Comparison of oleic acid hydrotreating at different reaction gas atmosphere was performed at 325 °C reaction temperature, 0.1 ml/min liquid flow rate and 0.8 ml/min

H_2 gas flow rate. Fatty acid was almost completely convert to hydrocarbon and intermediate under H_2 atmosphere. While no fatty acid conversion was observed when running the experiment under N_2 atmosphere. These results demonstrated that H_2 was necessary for oleic acid hydrotreating with $NiMoP/Al_2O_3$ catalyst.

Table 6.2 Effect of hydrogen on oleic acid hydrotreating at 325 °C.

Liquid	**Gas**	**Fatty acid conversion (%)**	**Hydrodeoxygenation (%)**
5 wt% Oleic acid in dodecane	N_2	0	0
5 wt% Oleic acid in dodecane (80 mol H_2/mol oleic acid)	H_2	99	76
Technical grade oleic acid (4 mol H_2/mol oleic acid)	H_2	3	0

Reaction condition: 0.1 ml/min liquid flow rate and 0.8 ml/min gas flow rate.

The effect of hydrogen to oleic acid molar ratio was investigated by using 5wt% oleic acid in dodecane and technical grade oleic acid. The reactions were performed at 325 °C, 0.1 ml/min liquid flow rate and 0.8 ml/min H_2 gas flow rate which is equivalent to 80 and 4 mol H_2/mol oleic acid feed ratio respectively. The results showed that hydrotreating reaction of fatty acid depended strongly on the amount of hydrogen. At 4 mol H_2/oleic acid which is at the stoichiometric needs of hydrogen for hydrodeoxygenation of oleic acid, most of the fatty acid remained in the liquid product in the form of steric acid and oleic acid. In contrast, fatty acid hydrotreating reaction was almost complete when using hydrogen in large excess amount (80 mol H_2/ mol oleic acid).

6.1.6 Effect of stainless steel and alumina support on oleic acid hydrotreating (Control experiment)

Control experiments were performed to investigate if the internal reactor surface and alumina layer support exhibited any form of catalytic activity on the hydrotreating reaction of oleic acid in the absence of NiMoP catalyst. Table 6.3 shows activity of reactor materials in term of product distribution, conversion of fatty acid and % hydrodeoxygenation. The blank test, carried out using non-heat treated stainless steel microtube reactor, revealed the formation of fatty alcohol that was formed by hydrogenation of fatty acid. A conversion of less than 10 % was observed in the blank test. Fatty alcohol and long chain ester were detected when using non-heat treated stainless steel microtube reactor coated with washcoat alumina support layer. Fatty acid conversion of 35% was achieved, however, no desired alkane product was formed. Consequently, a low hydrotreating performance of bare stainless steel tube and alumina support was concluded.

Reaction experiments with heat-treated stainless steel microtube and heat-treated stainless steel microtube coated with alumina support layer showed that they exhibited significant catalytic activity for oleic acid hydrotreating at 325 °C. This was an interesting finding and the presence of metal oxide on the top of stainless steel surface could have been responsible. Considerable quantity of C17 and C18 hydrocarbon, fatty alcohol and long chain ester were formed. However, compared to result obtained when using NiMoP/Al_2O_3 catalyst washcoat microtube, % hydrodeoxygenations were lower.

Table 6.3 Effect of stainless steel and alumina support on oleic acid hydrotreating.

	Non-heat treated stainless steel	Non-heat treated stainless steel + Al_2O_3 support	Heat treated stainless steel	Heat treated stainless steel + Al_2O_3 support	Heat treated stainless steel + Al_2O_3 support + NiMoP
Liquid product composition (wt%)					
C17 hydrocarbon	0	0	2.5	9.5	13.2
C18 hydrocarbon	0	0	15.7	41.0	62.6
Fatty alcohol	12.0	21.7	65.6	46.9	22.4
Fatty acid	88.0	75.8	3.4	1.8	1.3
Long chain ester	0	2.6	12.8	0.8	0.6
Fatty acid conversion (%)	9.2	35.0	97.8	98.6	99.1
% Hydrodeoxygenation	0	0	18.2	50.5	75.8

The reaction conditions: T= 325 °C, p=500 psig, $C_{fatty\ acid}$= 0.13 mol/l and residence time = 37 s

6.2 Triolein hydrotreating

The catalytic hydrotreating of triolein in dodecane was studied in continuous flow microtubular reactor over washcoat $NiMoP/Al_2O_3$ catalyst at 275-325 °C, 500 psig, 36-40 s residence time and 188 mol H_2/mol triolein feed ratio.

At 325 °C, the performance of the system was fairly stable within the first 2-3.5 h time on stream (Figure 6.10 (a)). Triolein was almost completely converted to other compounds and the concentration of unreacted triglyceride was below 0.5%. The main components in the liquid product were fatty alcohol (53%), C18 hydrocarbon (23%), long chain ester (12%) and C17 hydrocarbon (3.5%). Trace amount of diglyceride and monoglyceride were detected in the liquid product. This indicates that the rate of triglyceride conversion is faster than the rate of fatty alcohol conversion and fatty alcohol tends to accumulate in the liquid product. Thus, the hydrotreating of fatty alcohol can be considered as the rate-determining step in the conversion of triglyceride into hydrocarbons at this reaction condition. At time on stream longer than 4 h, the concentration of fatty acid sharply increased and it was the main component in the reaction product. The concentration of fatty alcohol decreased, concentration of hydrocarbon product decreased and concentration of triglyceride increased.

The changes in intermediates concentration reflected the deterioration of catalyst activity. Catalyst deactivation when using triolein as a feedstock was relatively extensive compared to when using oleic acid as a feedstock. The origin for catalyst deactivation is probably due to the formation of coke that covers the catalyst surface, since metal leaching was confirmed to be negligible. In addition, the qualitative analysis of gas outlet stream showed the presence of carbon dioxide, carbon monoxide, methane, ethylene, ethane and propane. Propane formation is believed to be mainly due to the cracking of the carboxylic chains of triglycerides, with consequent transformation of the glycerol backbone into propane.

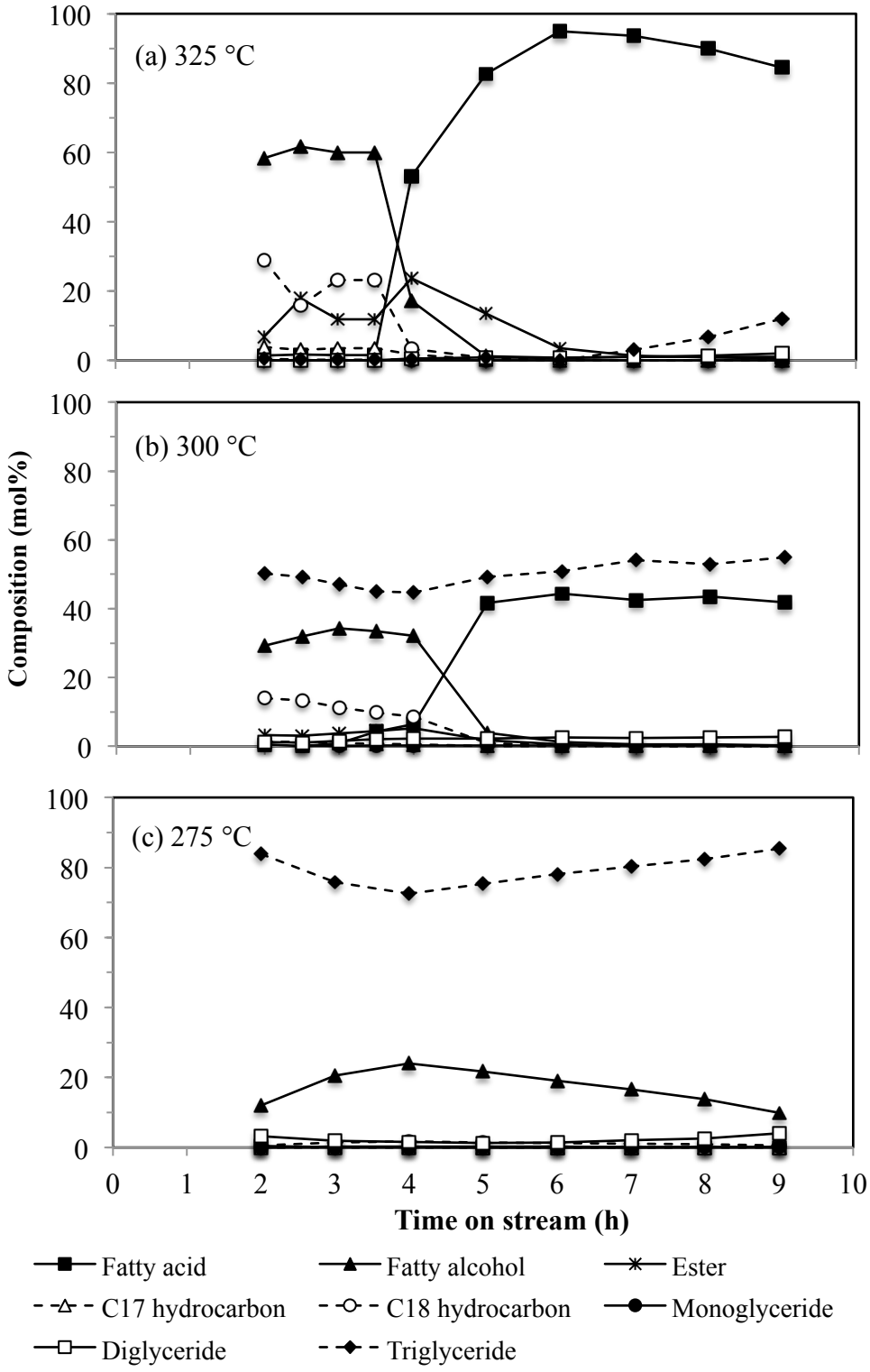

Figure 6.10 Reactant and product distribution profile of triolein hydrotreating Reaction conditions: T= 275-325 °C, p=500 psig, $C_{triolein}$= 0.06 mol/l and residence time = 36-40 s.

Hydrotreating of triolein depends strongly on the temperature. The formation of hydrocarbon at 300 °C, was moderately low as shown in Figure 6.10 (b). The liquid product analysis revealed the presence of unreacted triglyceride and fatty alcohol as main components. Catalyst deactivation was also observed after 4 h time on stream. The reaction was much slower at 275 °C (Figure 6.10(c)). More than 70 mol% of unreacted triglyceride remained in liquid product. The conversion of triglyceride was 28.7% at 275 °C, while the conversion was 47.9% at 300 °C and 99.7% at 325 °C (Figure 6.11).

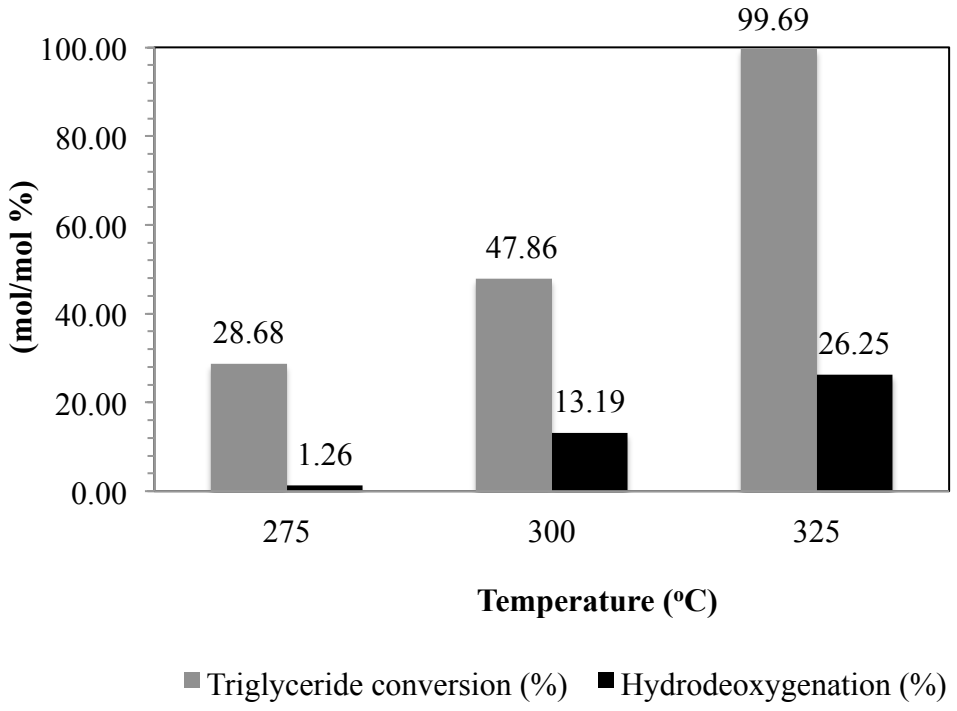

Figure 6.11 Triglyceride conversion and %hydrodeoxygenation of triolein hydrotreating. The reaction conditions: p=500 psig, $C_{triolein}$= 0.06 mol/l and residence time = 36-40 s.

The composition of liquid product changes as a function of residence time. This is shown in Figure 6.12. The amount of fatty acid increased with increasing residence time from 11 s to 26 s and decreased when triolein conversion was almost completed.

Unreacted triolein almost disappeared within the 36 s residence time. Concentration of fatty alcohol, C18 hydrocarbon and C17 hydrocarbon increased with residence time.

Base on liquid and gas product analysis, the hydrotreating of triglyceride proceeded via the hydrocracking of triglyceride into diglyceride, monoglyceride and fatty acid (Figure 6.13). Then fatty acid was subsequently deoxygenation to hydrocarbon via similar pathways as previous described in oleic acid hydrotreating.

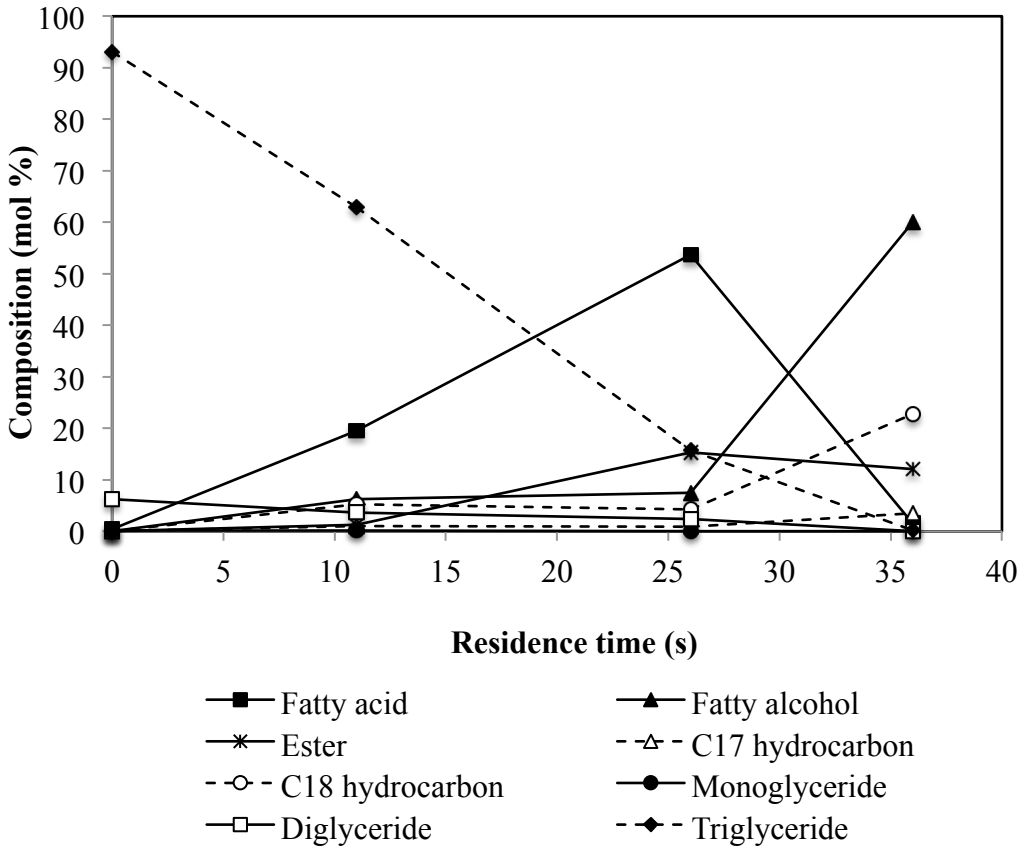

Figure 6.12 Reactant and product distribution profile of triolein hydrotreating as a function of residence time. The reaction conditions: T= 325 °C, $C_{triolein}$= 0.06 mol/l and p=500 psig.

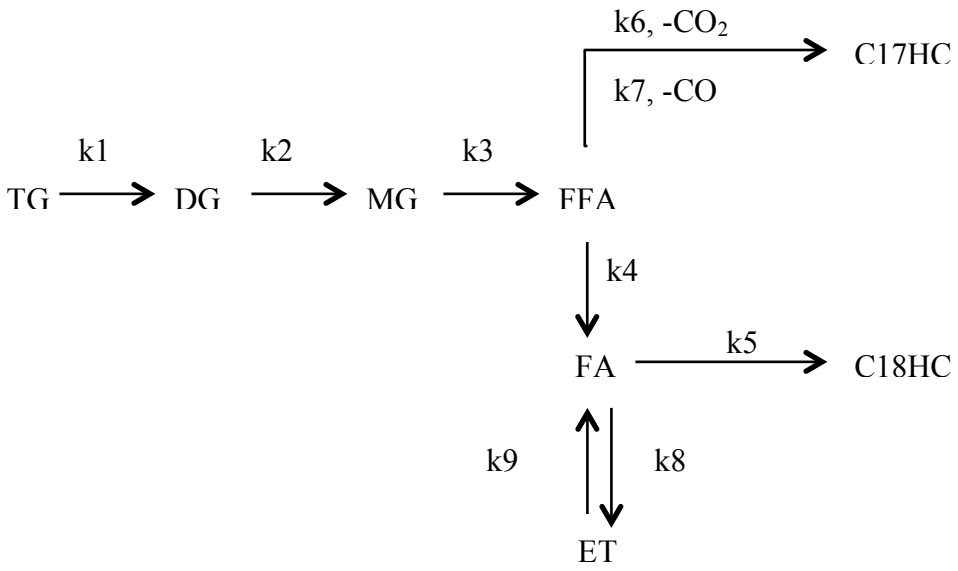

Figure 6.13 A reaction pathway for hydrotreating reaction of triglyceride.

6.3 Jatropha oil hydrotreating

Jatropha oil is a non-food vegetable oil, which has potential to be a feedstock for biofuel production. Jatropha oil, used as a feed for this experiment, contained 90 wt.% of triglycerides, 3.5 wt.% of free fatty acids, 5.4 wt.% of diglycerides and 0.2 wt.% of monoglycerides. Jatropha oil hydrotreating was more complex than triolein hydrotreating since it consists of many triglycerides ranging from C16 to C18:2. Figure 6.14 shows GC analysis of jatropha oil and liquid product from 7 wt.% jatropha oil in dodecane hydrotreating using NiMoP/Al_2O_3 catalyst at 325 °C, 500 psig and residence time of 36 s. GC analysis shows almost complete disappearance of triglycerides in the product mixture. Triglyceride conversion was 97.5% and %hydrodeoxygenation was 68.6. The main components in the liquid product were hydrocarbon ranging from C15-C18 (68.6%) and fatty alcohol (29.4%). Small amount of monoglyceride, diglyceride, triglyceride and long chain ester were detected in the liquid product.

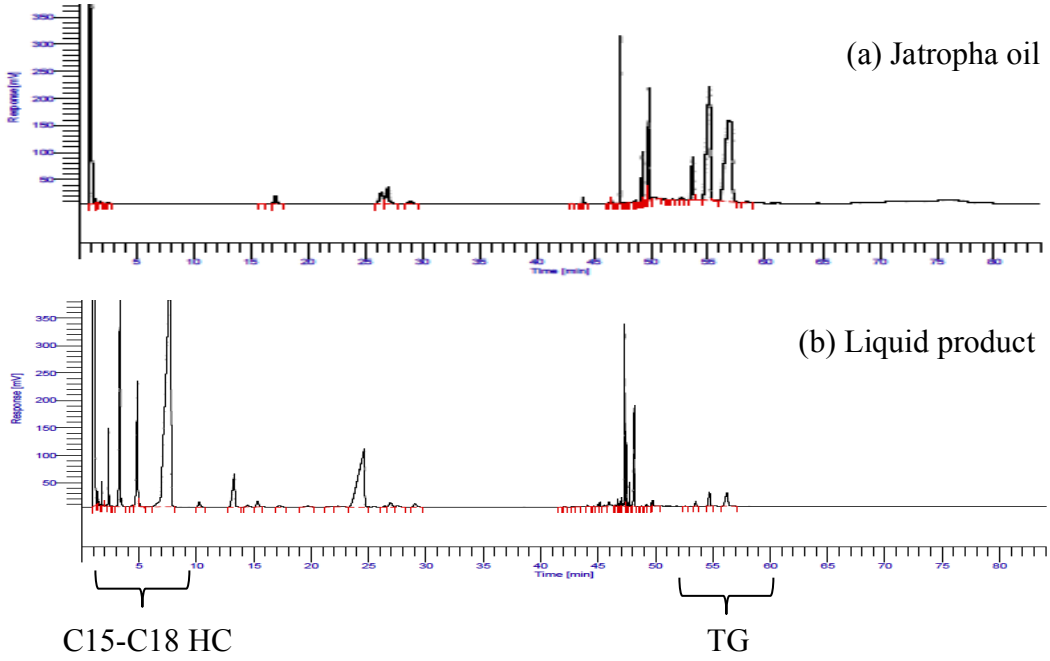

Figure 6.14 GC Chromatogram of (a) jatropha oil and (b) liquid product from jatropha oil hydrotreating using NiMoP/Al_2O_3 catalyst at 325 °C, 500 psi and residence time of 36 s.

6.4 Intrinsic kinetic and parameter optimization

6.4.1 Intrinsic kinetic and parameter optimization of oleic acid hydrotreating

In the present study, a kinetic model for hydrotreating of fatty acid was developed. The kinetic model focuses on the kinetics describing the formation of major liquid products and intermediates. This was the first reported investigation for kinetics of hydrotreating reaction of fatty acid performed in continuous flow microchannel reactor. Although this reaction has previously been studied in both batch and fixed bed reactor [6, 7]. Modeling of the kinetic data from the microreactor was performed to find the best model in order to get a better understanding of the reaction mechanism on one hand and on the other hand to find a rate equation for proper reactor design.

From the experimental concentration data of reactants, products and reaction intermediates at the outlet of microtubular reactor, the rate constants were estimated at a certain temperature. COMSOL and MATLAB optimization routine was used for determining the rate constants of the reaction. A MATLAB optimization subroutine 'fminsearch', which is based on simplex search method was used for optimization. The simulation program read the initial values of the rate constants, which were determined by the trial and error method. The rate equations, a system of simultaneous differential equations, of the reaction were solved to get the analytical concentration of the reactant at the outlet of microtubular reactor. The simulation results were compared with experimental results at each measured point. All deviations between experimental and calculated values were squared and summed up to form an objective function, F.

$$F = \sum_{i=1}^{n} \left(m_i(k_i) - m_{i,\exp} \right)^2 \tag{6.4}$$

This function was fed into an optimization routine to find the optimal rate constants. New values of objective function were calculated for each set of the rate constants. The iteration proceeds until the absolute difference between two successive objective functions is less than a predefined tolerance ε. The final k value obtained was the optimal rate constants as shown the Figure 6.15. Reaction rate constants for oleic acid hydrotreating, obtained by minimizing the objective function at each temperature are tabulated in Table 6.4. All reaction rate constants increase with increasing temperature. The pre-exponential factors (k_0) and activation energies (E_a) are determined from the rate constants at various temperatures by Arrhenius law (Eq. 6.5).

$$k = k_0 \exp(-E_a / RT) \tag{6.5}$$

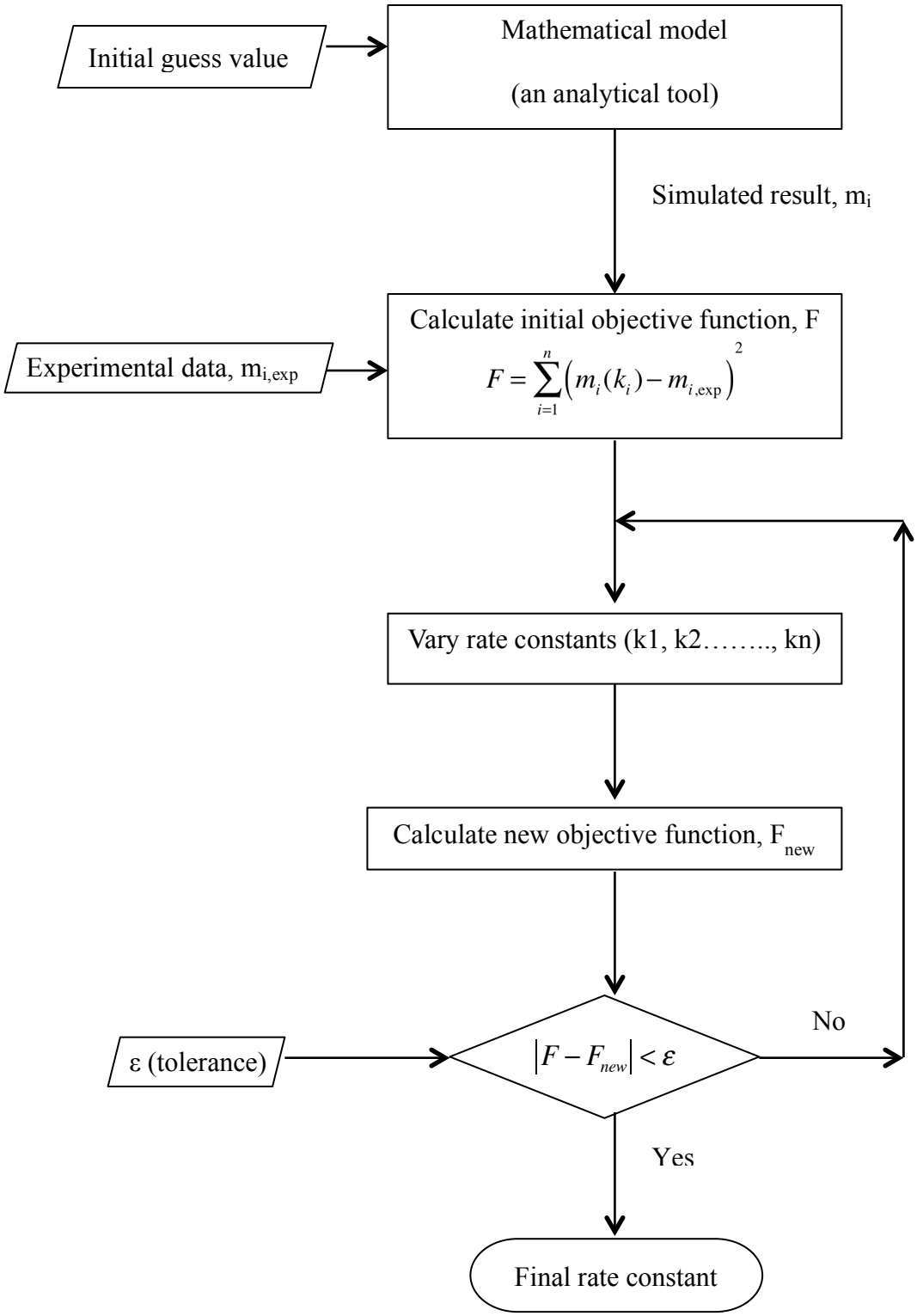

Figure 6.15 Flowchart for the parameter fitting procedure.

The values are listed in Table 6.5 and shown in Figure 6.16. The simulation and experimental concentration profile of reactants and liquid products in oleic acid hydrotreating at different temperature (275-325°C) are shown in Figure 6.17-6.19. Modeling of temperature dependence of oleic acid hydrotreating demonstrated an excellent fit to the experimental data.

Table 6.4 Optimization results for reaction rate constants of oleic acid hydrotreating.

Rate Constant	**Temperature (°C)**		
	275	**300**	**325**
k4 [s^{-1}]	5.80×10^{-4}	2.75×10^{-2}	3.85×10^{-1}
k5 [s^{-1}]	2.60×10^{-4}	1.17×10^{-3}	2.78×10^{-3}
k6 [s^{-1}]	4.36×10^{-7}	1.01×10^{-6}	1.98×10^{-6}
k7 [s^{-1}]	4.54×10^{-6}	3.86×10^{-4}	3.50×10^{-2}
k8 [$m^3\ mol^{-1}\ s^{-1}$]	6.74×10^{-5}	2.22×10^{-4}	2.40×10^{-4}
k9 [$m^3\ mol^{-1}\ s^{-1}$]	1.53×10^{-7}	3.35×10^{-7}	4.15×10^{-6}

Table 6.5 Pre-exponential factors (k_0) and activation energies (E_a) for oleic acid hydrotreating.

	k_0	**E_a (kJ/mol)**
k4	4.56×10^{30}	354.9
k5	6.14×10^{8}	129.4
k6	32.48	82.5
k7	1.21×10^{41}	487.4
k8	377.4	70.0
k9	1.18×10^{10}	178.5

The liquid product composition for a longer residence time were calculated and presented in Figure 6.20 in order to get a better idea how residence time may affect the hydrotreating reaction of oleic acid in microchannel reactor. Fatty acid was completely reacted in 10 s and most of liquid intermediate were converted into hydrocarbon at 240 s (Figure 6.21). The microchannel reactor offers considerable improvement compared to previous studies. The timescale for complete hydrotreating reaction in the microchannel was on the scale of minutes compared to hour reaction time reported in the literature [6].

The values are listed in Table 6.5 and shown in Figure 6.16. The simulation and experimental concentration profile of reactants and liquid products in oleic acid hydrotreating at different temperature (275-325°C) are shown in Figure 6.17-6.19. Modeling of temperature dependence of oleic acid hydrotreating demonstrated an excellent fit to the experimental data.

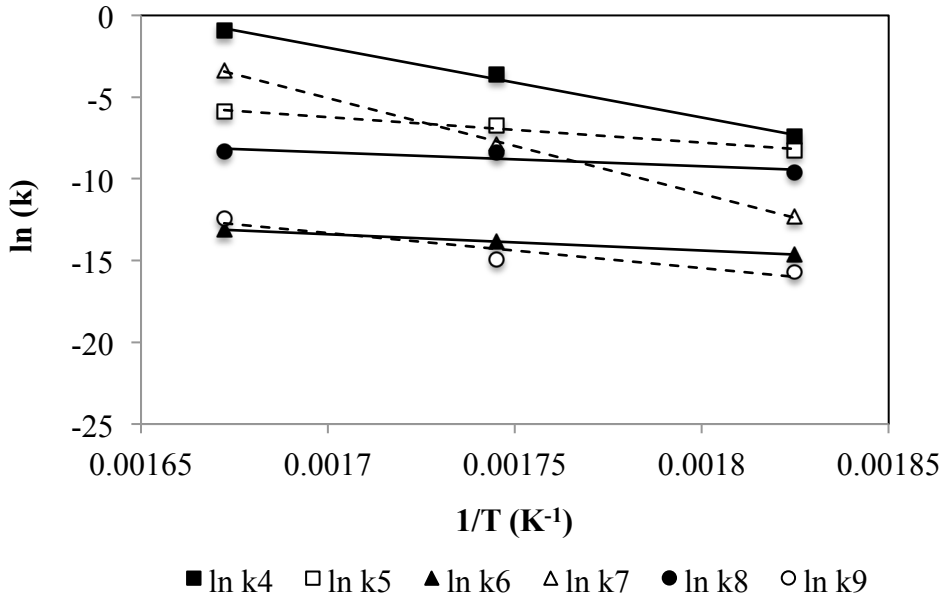

Figure 6.16 Temperature dependence of process kinetic parameters of oleic acid hydrotreating.

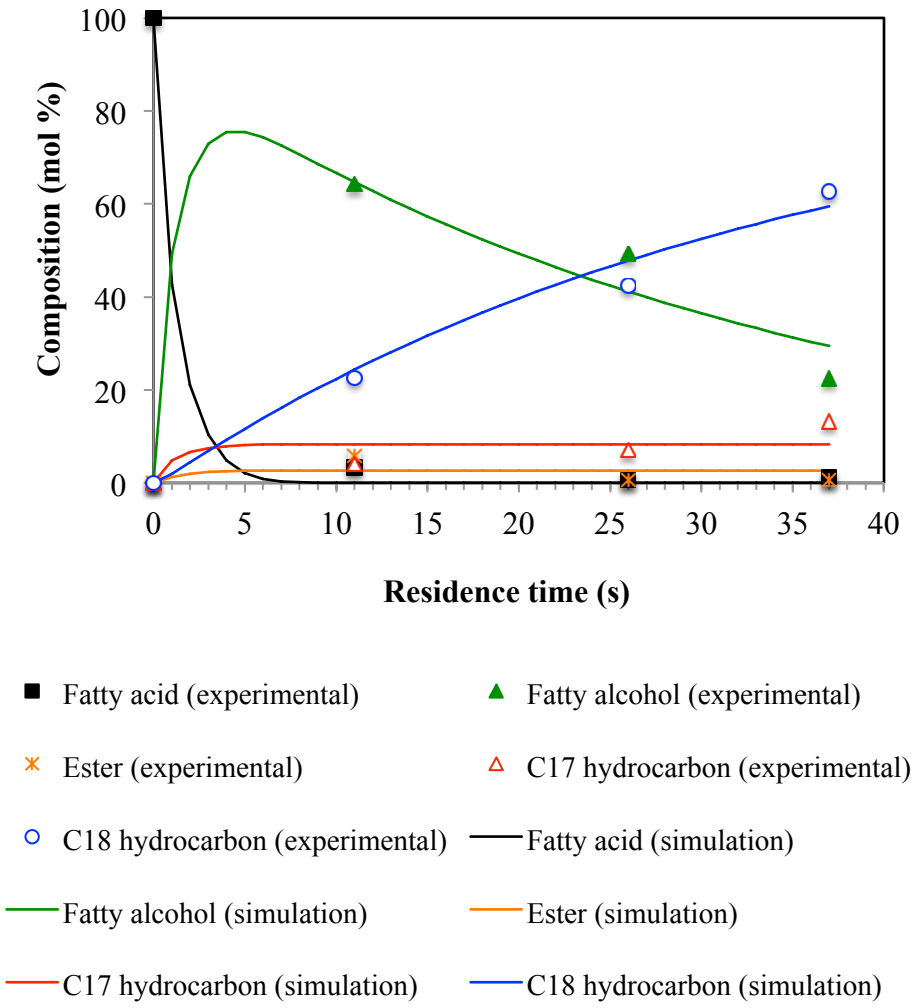

Figure 6.17 Simulation and experimental concentration profile of liquid product in oleic acid hydrotreating at various residence times. The reaction conditions: T=325 °C, p=500 psig, $C_{fatty\ acid}$= 0.13 mol/l.

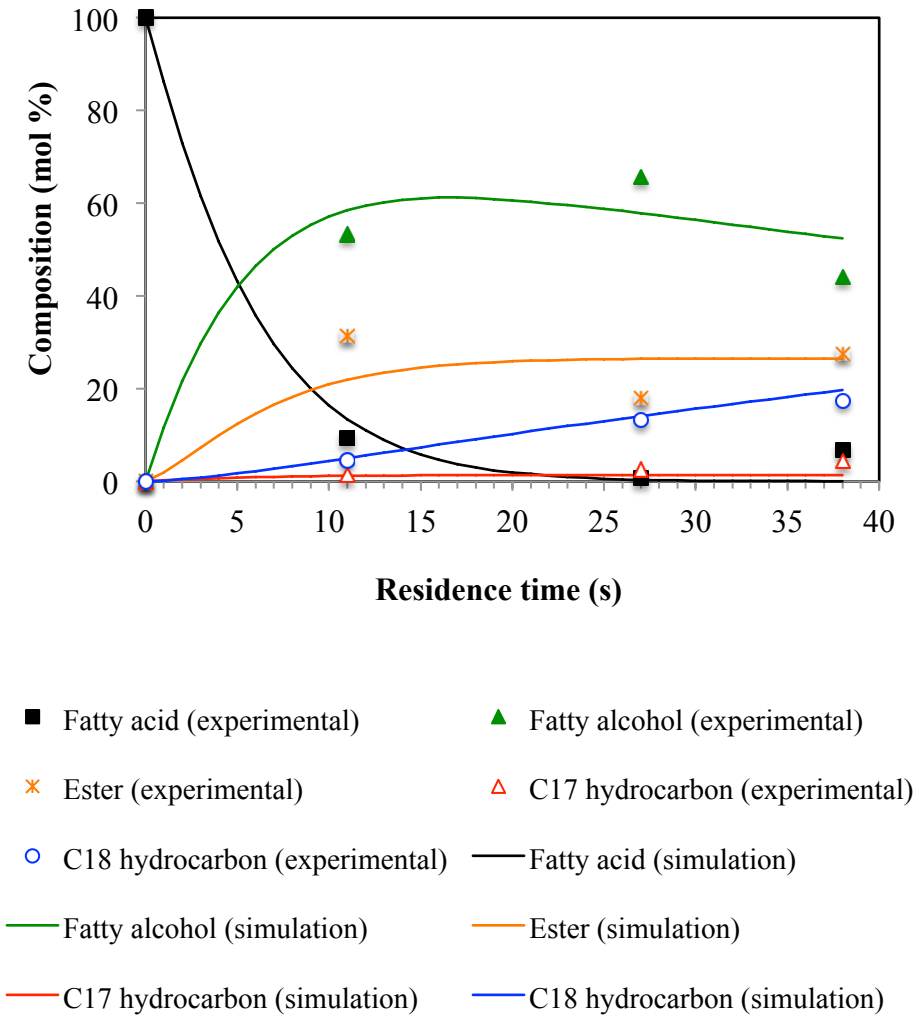

Figure 6.18 Simulation and experimental concentration profile of liquid product in oleic acid hydrotreating at various residence times. The reaction conditions: T=300 °C, p=500 psig, $C_{fatty\ acid}$= 0.13 mol/l.

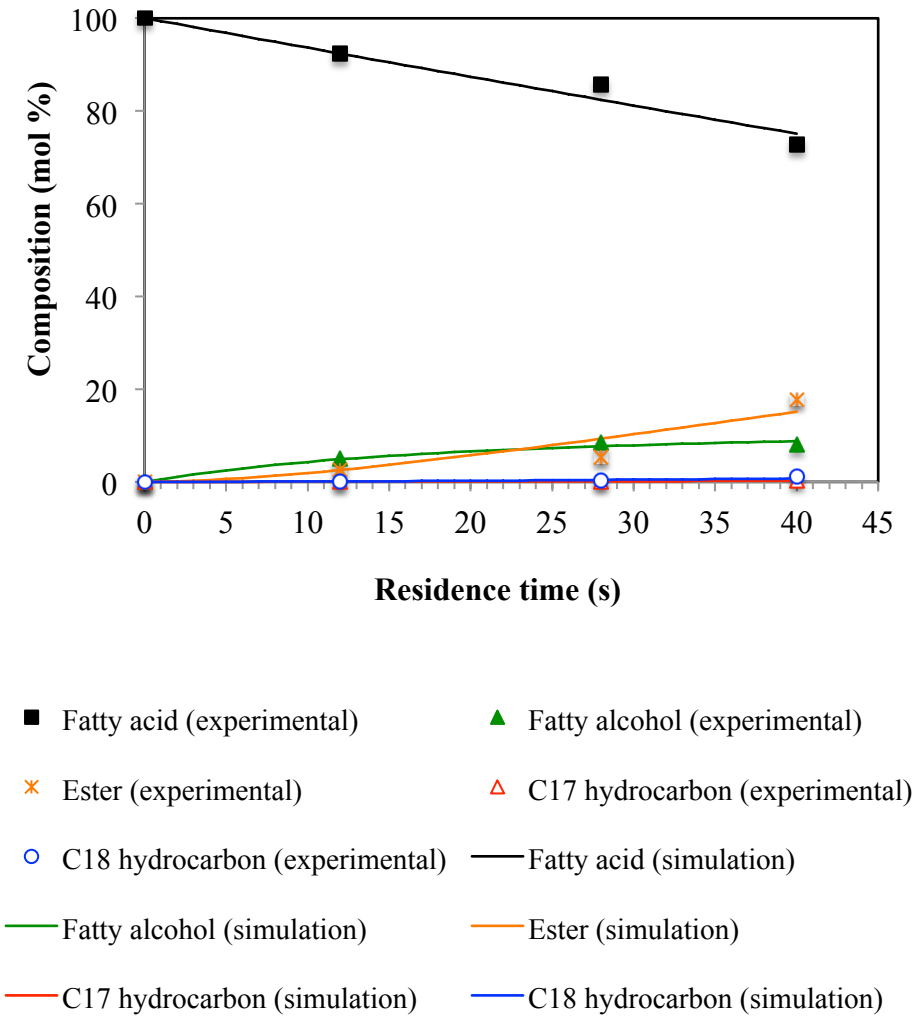

Figure 6.19 Simulation and experimental concentration profile of liquid product in oleic acid hydrotreating at various residence times. The reaction conditions: T=275 °C, p=500 psig, $C_{fatty\ acid}$= 0.13 mol/l.

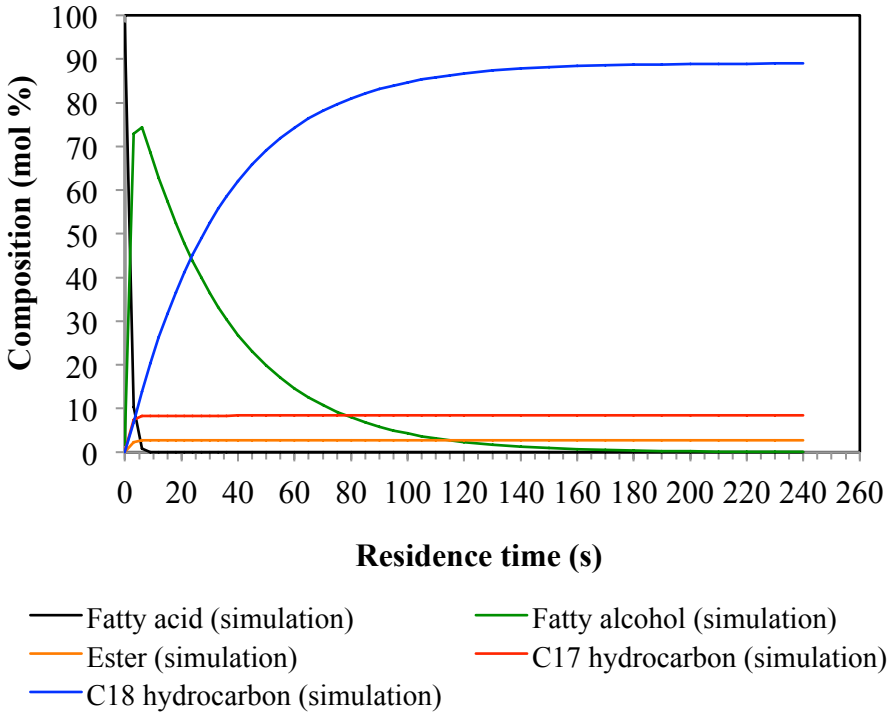

Figure 6.20 Simulation concentration profile of liquid product in oleic acid hydrotreating. The reaction conditions: T=325 °C, p=500 psig, $C_{fatty\ acid}$= 0.13 mol/l.

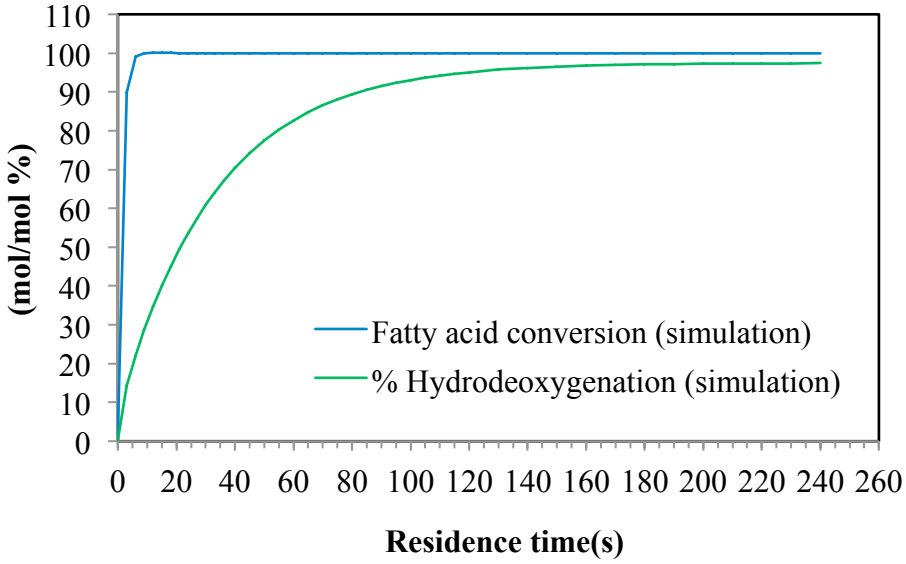

Figure 6.21 Predicted fatty acid conversions and % hydrodeoxygenation for oleic acid hydrotreating. The reaction conditions: T=325 °C, p=500 psig, $C_{fatty\ acid}$= 0.13 mol/l.

6.4.2 Intrinsic kinetics and parameter optimization of triglyceride hydrotreating

The propose model for triglyceride hydrotreating is rather complex as shown in Figure 6.13. Therefore, the kinetic parameters obtained from fatty acid hydrotreating, which is an intermediate product in triglyceride hydrotreating, were used as fixed values in triglyceride hydrotreating parameter optimization.

Reaction rate constants for triolein hydrotreating, obtained by minimizing the objective function are tabulated in Table 6.6. The simulation and experimental triglyceride conversion and % hydrodeoxygenation in triolein hydrotreating at 325°C are shown in Figure 6.22.

Table 6.6 Estimate rate constants for triolein hydrotreating at 325 °C.

	Rate Constant
k1 [s^{-1}]	2.76×10^{-3}
k2 [s^{-1}]	1.38×10^{-2}
k3 [s^{-1}]	1.22×10^{-2}
k4 [s^{-1}]*	3.85×10^{-1}
k5 [s^{-1}]*	2.78×10^{-3}
k6 [s^{-1}]*	1.98×10^{-6}
k7 [s^{-1}]*	3.50×10^{-2}
k8 [$m^3\ mol^{-1}\ s^{-1}$]*	2.40×10^{-4}
k9 [$m^3\ mol^{-1}\ s^{-1}$]*	4.15×10^{-6}

* Fixed value based on modeling of fatty acid hydrotreating

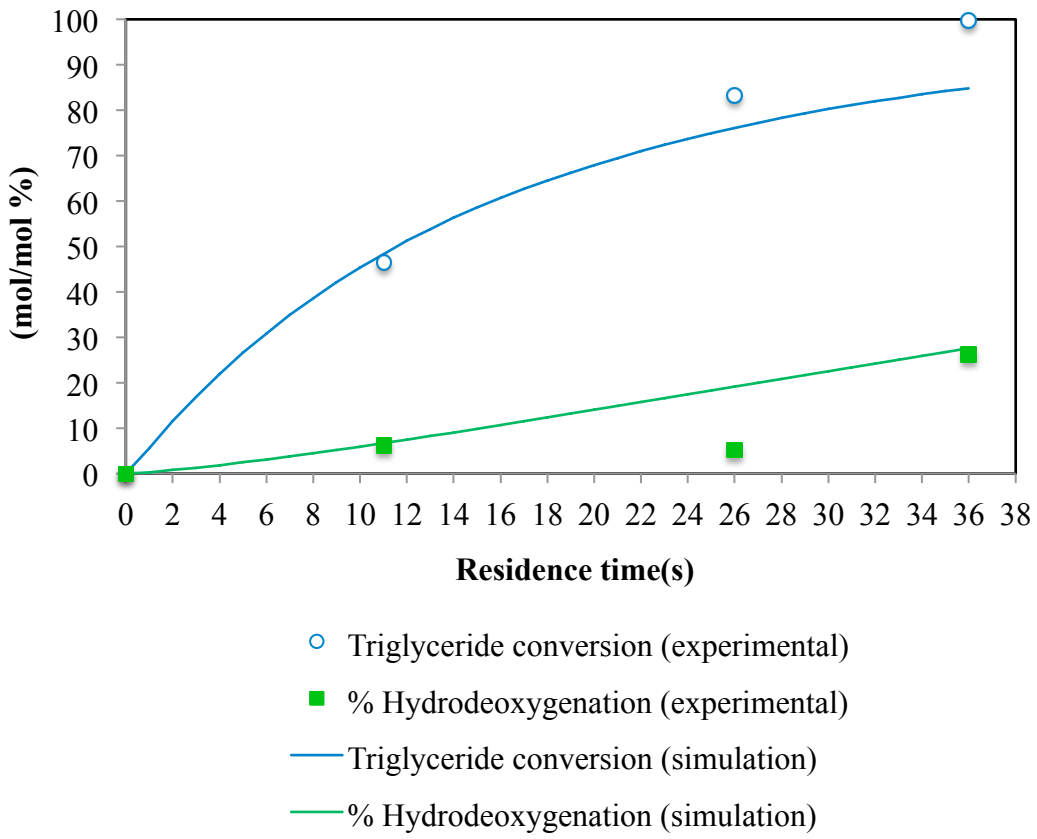

Figure 6.22 Simulation and experimental triglyceride conversion and % hydrodeoxygenation in triolein hydrotreating at 325°C.

6.5 Effectiveness of the catalyst

The use of microreactor as kinetic device has a clear advantage that the thin catalyst film allows the determination of the intrinsic kinetics without the effect of mass transfer limitation. The washcoat catalyst used in this study is a thin porous catalyst layer. Thus, the reactants diffuse into the pore and the reactions take place at the wall of the pore. The effective factor (ξ), which defined as the ratio of actual mean reaction rate within pore and rate if not slowed by pore diffusion, was used to determine whether mass transfer limitations in the catalyst layer were significant for these experiments.

For first-order reaction, rate is proportional to the concentration. So the effectiveness factor for first order reaction is given by

$$\xi = C_A / C_{AS} \tag{6.6}$$

Effectiveness factor can be re-write in term of dimensionless parameter, Thiele modulus (φ). When Thiele modulus, was defined as

$$\varphi = L\sqrt{\frac{k}{D_{eff}}} \tag{6.7}$$

Where L is catalyst layer thickness, k is reaction rate constant and D_{eff} is effective diffusion coefficient in the catalyst layer. The effective diffusion coefficient is given by

$$D_{eff} = \frac{D\varepsilon_{coating}}{\tau} \tag{6.8}$$

The tortuosity τ is not known, but is assumed to be 1.7, which is a typical value for random pore structure [8]. The effectiveness factor for first-order reaction ($\xi_{first\text{-}order}$) is given by

$$\xi_{first-order} = \frac{\tanh\varphi}{\varphi} \tag{6.9}$$

When the Thiele modulus is large, internal diffusion limits the overall rate of reaction. When Thiele modulus is small, the surface reaction is rate –limiting.

For oleic hydrotreating at 325 °C, minimum and maximum first order reaction rate constant in the system are $1.98\text{x}10^{-6}$ and $3.85\text{x}10^{-1}$ 1/s, respectively. Minimum and maximum diffusion coefficient in liquid phase are $1.55\text{x}10^{-8}$ and $1.74\text{x}10^{-7}$ m^2/s, respectively. Catalyst layer thickness evaluated by SEM was 1.52 μm. Thus, the calculated Thiele modulus was in the range of $9.45\text{x}10^{-6}$ – $1.4\text{x}10^{-2}$.

The small value of Thiele modulus means a short pore, slow reaction or rapid diffusion, all three factors tending to lower the resistance to diffusion. Calculated Thiele modulus values were smaller than 0.4, resulted in the effectiveness factor value approached to 1. This result implied that the reactant concentration does not drop appreciably within the pore. The mass transfer limitation in the catalyst was not significant in this experiment and the obtained reaction rate constants are the intrinsic values. The effectiveness factors of this system as a function of catalyst layer thickness were calculated and shown in Figure 6.23. The value of effectiveness factor approaches to 1 when the catalyst layer thickness is less than 20 μm. Thus, mass transfer limitation is not significant up to this point.

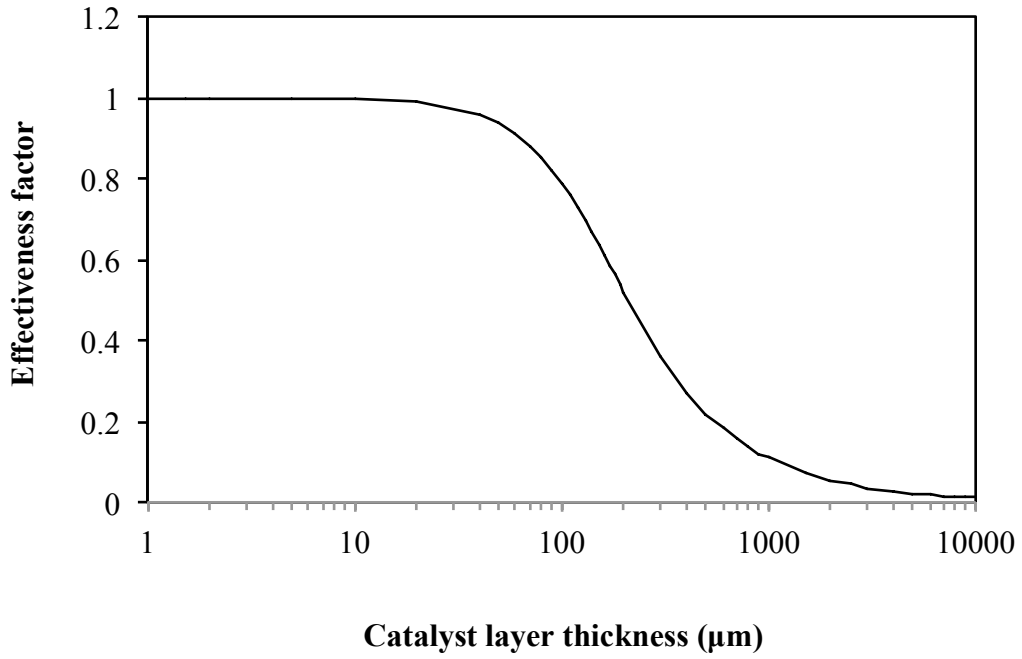

Figure 6.23 Effectiveness factor as a function of catalyst layer thickness.

6.6 References

[1] Kubicka D., Bejblova M. and Vlk J., 2010, Conversion of vegetable oils into hydrocarbons over CoMo/MCM-41 catalysts, Top Catal, 53, 168-178.

[2] Santillan-Jimenez, E., Crocker, M., 2012, Catalytic deoxygenation of fatty acids and derivatives to hydrocarbon fuels via decarboxylation/decarbonylation, J Chem Technol Biotechnol.

[3] Madsen, A.D., Ahmed, E.D., Christensen, C.H., Fehrmann, R. and Riisager, A., 2011, Hydrodeoxygenation of waste fat for diesel production: Study on model feed with Pt/alumina catalyst, Fuel, 90 (11), 3433-3438.

[4] Nikolova, D., Edreva-Kardjieva, 2011, Water-gas shift of K-promoted (Ni)Mo/Al2O3 system in sulfur-containing feed, Reac Kinet Mech Cat, 103, 71-86.

[5] Maki-Arvela, P., Snare, M., Eranen, K., Myllyoja, J., Murzin, D.Y., 2008, Continuous decarboxylation of lauric acid over Pd/C catalyst, Fuel, 87, 3543-3549.

[6] Lestari, S., Maki-Arvela, P., Eranen, K., Beltramini, J., Max Lu, G.Q., Murzin, D.Y., 2010, Diesel-like hydrocarbons from catalytic deoxygenation of stearic acid over supported Pd nanoparticles on SBA-15 catalyst, Catal Lett, 134, 250-257.

[7] Snare, M., Kubickova, I., Maki-Arvela, P., Eranen, K., Murzin, D.Y., 2008, Catalytic deoxygenation of unsaturated renewable feedstocks for production of diesel fuel hydrocarbons, Fuel, 87, 933-945.

[8] Froment, G.F., Bischoff, K.B., Chemical Reactor Analysis and Design, John Wiley & Sons, New York, 2nd, 1990.

CHAPTER 7

CONCLUSIONS AND RECOMMENDATIONS

Conclusions

In this study, a microtubular reactor containing NiMoP/Al_2O_3 washcoat catalyst was developed. The catalyst was prepared and deposited inside a 500 μm diameter, 316 stainless steel microtube by the sol–gel process of establishing alumina support, followed by impregnation of the active metal. Thermal pretreatment of the microreactor creates a surface with grainy morphology, which is beneficial for the adhesion of alumina coating. Both axial and radial uniformity of alumina coating in the microtube was obtained, with an average thickness of 1.52±0.39 μm.

The kinetics of hydrotreating vegetable oil with model compounds for diesel fuel production was studied over NiMoP/Al_2O_3 catalyst in a microtubular reactor. Oleic acid and triolein were used as model compounds for fatty acid and triglycerides, respectively. The main advantage of a microreactor for kinetic studies is the use of a very thin catalyst layer that minimizes internal diffusion limitations and makes it possible to measure intrinsic kinetics. The reaction was performed in the slug flow regime and the hydrotreating results showed that the microchannel reactor was suitable for the hydrotreating process. Complete conversion of the fatty acid and triglyceride hydrotreating reactions were achieved in less than 40 s of residence time at 500 psig pressure and a reaction temperature of 325 °C.

Hydrotreating of fatty acids occurred primarily via hydrodeoxygenation and the main liquid products were octadecane and heptadecane. Fatty alcohol, fatty acid and long chain esters were formed as reaction intermediates. Hydrotreating of triglycerides proceeded via the hydrocracking of triglyceride into diglycerides, monoglycerides and fatty acids. Fatty acids were subsequently deoxygenated to hydrocarbons. The

conversion of fatty acids and triglycerides increased with increasing temperatures and decreasing feed concentrations.

A catalyst deactivation in fatty acid and triglyceride hydrotreating was observed during a long duration performance test. Catalyst deactivation when using triolein as a feedstock was extensive compared to when using oleic acid as a feedstock. The origin of catalyst deactivation is probably due to the formation of coke that covers the catalyst surface, since metal leaching was confirmed to be negligible.

A detailed mathematical model was developed to represent this two-phase chemical reaction process. The mathematical model is entirely based on first principles, i.e. no adjustable or correlation parameters were used. This model can be used as an analytical tool for kinetic parameter estimation and as a tool for optimal hydrotreating reactor design. Successful kinetic modeling and parameter estimation was performed based on the proposed reaction mechanism of fatty acid and triglyceride hydrotreating. The predicted results were in good agreement with experimental results.

Recommendations

A potential area of future work for continued research on hydrotreating of bio-oils in microtubular reactors should include an investigation on the effect of catalyst types in an attempt to increase conversion, decrease side reactions (i.e. esterification) and increase the life time of catalyst.

Another potential area of future work for continuation of this research is a new design for a microchannel reactor that can provide larger residence time and better contact between gas, liquid and solid catalyst surface.

The modeling of multiphase chemical reaction flow in a microchannel to solve a complete gas-liquid slug formation with chemical reaction at the reactor wall is another potential area of future work.

Appendix A. Liquid product analysis

The liquid products were analyzed by gas chromatograph for its composition of triglycerides, diglycerides, monoglycerides, fatty acid, fatty alcohol, long chain ester and alkanes. The analyses were performed with Perkin Elmer Clarus 500, Gas chromatograph with autosampler and flame ionization detector (FID). Restek MXT biodiesel TG column with 100% dimethyl polysiloxane stationay phase was used for the analysis. The column has 14 m in length, with 0.53 mm internal diameter and 0.16 um film thickness. The operating conditions are as follow;

Table A.1 GC operating conditions.

Injector	
Sample size	1 μL
Injector temperature program	
Initial temperature	280 °C, Hold 65 min
Rate 1	15 °C /min to 355 °C, Hold 14 min at 355 °C
Column temperature program	
Initial temperature	130 °C
Rate 1	1 °C /min to 169 °C
Rate 2	15 °C /min to 350 °C, Hold 33 min at 350 °C
Detector	
Type	Flame ionization
Temperature	350 °C
Carrier gas	
Type	Helium
Flow rate	3 ml/min

Standard preparation

Monoolein, diolein, triolein, oleic acid, strearyl alcohol, stearyl stearate, tricaprin and n-C18 were used as the standards for this analysis. GC calibration standards were prepared by mixing the individual stock standards. After mixing, 100 µL of the derivatization agent, N-Methyl-N-(trimethylsilyl)trifluoroacetamide (MSTFA) was added to each calibration standard. After 20 minutes at room temperature, 2 mL of n-heptane was added to each calibration standard. These final reaction mixtures were then directly injected into the gas chromatograph.

Sample preparation

Approximately 20 mg of liquid sample was accurately weighed into 15 ml vial. 100 µl of tricaprin internal standard and 100 µl of MSTFA were added to sample vial by microsyringe. Vortex the vial and allow setting for 20 minutes at room temperature. Add approximately 2 ml of n-heptane to the vial and shake.

Calculation

Peak identification for each compound was made using the relative retention times. The amount of n-alkane, fatty alcohol, fatty acid, long chain ester, monoglycerides, diglycerides and triglycerides in each sample were calculated with the calibration functions derived from the n-C18, stearyl alcohol, oleic acid, stearyl stearate, monoolein, diolein, and triolein calibration functions, respectively. Individual compound content can be calculated by;

$$G_i = \left(\left(a_i \, x \, \frac{A_i}{A_{is}} \right) + b_i \right) \frac{W_{is}}{W} x \, 100$$

Where G_i mass percentage of individual compound in sample

A_i peak area of individual compound

A_{is} peak area of internal standard

W_{is} weight of internal standard, mg

W weight of sample, mg

a_i slope of calibration function

b_i intercept of calibration function

Appendix B. Critical orifice flow calculation

A critical flow orifice with 3 μm hole is used to establish the required flow rate of H_2 gas. The gas mass flow rate (G, kg/m^{2}s) is dependent of upstream pressure.

$$G = P_0 \left[\frac{Mw*k}{R\,T_0} \left(\frac{2}{1+k} \right)^{(k+1)/(k-1)} \right]^{1/2}$$

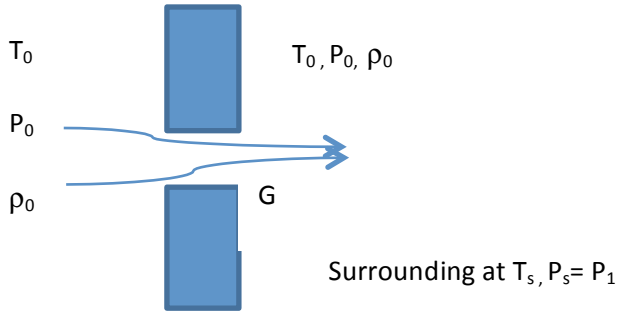

$$Flow\ rate\ at\ STP, ml/min = \left(\frac{G * \left(\frac{\pi d^2}{4} \right)}{Mw} \right) (Molar\ volume\ at\ STP)$$

Gas	Hydrogen	
Molecular weight, Mw	0.00201588	kg/mol
Molar volume at STP	0.0224	m^3/mol
Gas constant, R	8.314	m^3 Pa/K mol
Temperature, T_0	50	°C
Heat capacity ratio, k	1.407	
Orifice diameter,d	3	μm
Pressure, P_0	1000-1700	psi

Theoretical analysis of hydrogen gas flow rate through 3 μm orifice at various gas inlet pressure are shown in Table B.1 and Figure B.1.

Table B.1 Hydrogen flow rate at various gas inlet pressure.

Inlet pressure, P_0(psi)	Flow rate at STP (ml/min)	Flow rate at 500 psi 50 °C (ml/min)
1000	19.31	0.67
1100	21.24	0.74
1200	23.17	0.80
1300	25.10	0.87
1400	27.03	0.94
1500	28.96	1.01
1600	30.90	1.07
1700	32.83	1.14

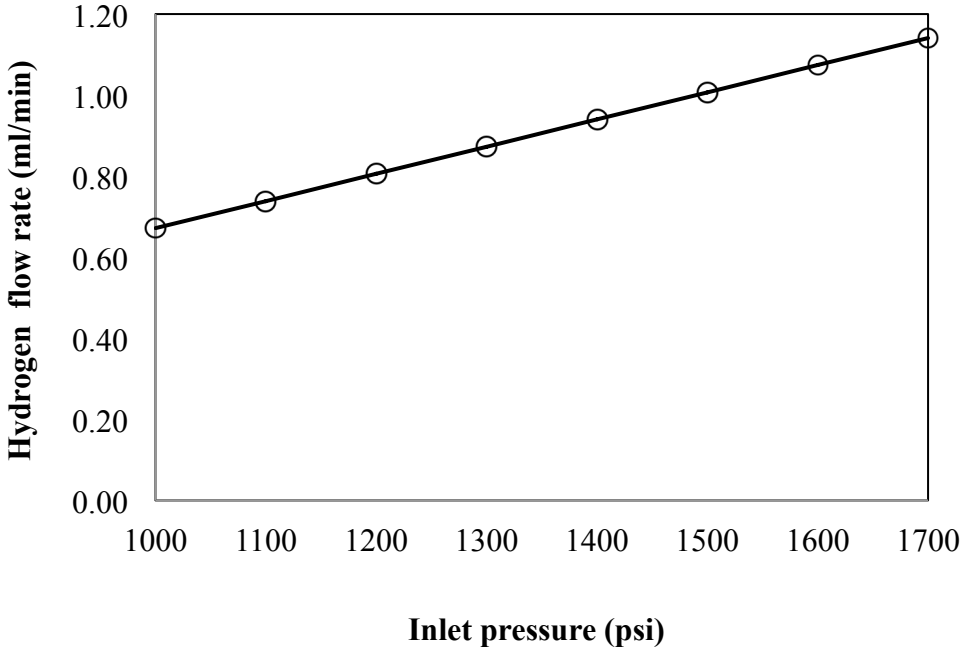

Figure B.1 Hydrogen flow rate at various gas inlet pressure.

Appendix C. COMSOL-MATLAB code for kinetic parameters estimation and optimization

A MATLAB program link with COMSOL was used to find the optimized values of reaction rate constant. The example of MATLAB program is as follow:

C1. Driver MATLAB program

```
clear all;
% Initial value
k0 = [1e-1 1e-3 1e-2 1e-2 1e-4 1e-4 ];
options=optimset('Display','iter','PlotFcns',@optimplotfval,'TolX',1e-6,'TolFun',1e-6);
[k,fval,exitflag,output]=fminsearch('OA3251ST',k0,options)
```

C2. Slave Error function

```
function f = OA3251ST(k)
import com.comsol.model.*
import com.comsol.model.util.*
model = ModelUtil.create('Model');
model.modelPath('Z:\Windows.Documents\Desktop\P Tuk');
model.name('OA3251ST.mph');
k11=k(1);
k12=k(2);
k13=k(3);
k14=k(4);
```

```
k15=k(5);

k16=k(6);

model.param.set('k4', k11);

model.param.set('k7', k12);

model.param.set('k6', k13);

model.param.set('k7', k14);

model.param.set('k8', k15);

model.param.set('k9', k16);

figure(4),plot(k11,'o')

hold on

figure(5),plot(k12,'gd')

hold on

figure(6),plot(k13,'rd')

hold on

figure(7),plot(k14,'bd')

hold on

figure(8),plot(k15,'o')

hold on

figure(9),plot(k16,'o')

hold on

model.param.set('Tsys', '325+273 [K]');

model.param.set('u0', '0', 'm/s');

model.param.set('ub', '0.1374 [m/s]', 'm/s');

model.param.set('mw_TG', '0.8854 [kg/mol]', 'Molecular weight of Triolein, kg/mol');

model.param.set('Area_liq', '2.505 [mm^2]', 'Area of lquid slug, m2');

model.param.set('Area_gas', '29.27  [mm^2]');

model.param.set('Rg', '8.205746*(10^-5)', 'Gas constant, m3 atm/K mol');

model.param.set('Pg', '34.5', 'System pressure, atm');
```

```
model.param.set('M', '1');

model.param.set('rho_liq', '502.7 [kg/m^3]');

model.param.set('visc_liq', '0.0002 [Pa*s]');

model.param.set('wtfrac', '0.05');

model.param.set('mw_FFA', '282.5 [g/mol]');

model.param.set('xexp1', '0.9664');

model.param.set('xexp2', '0.9779');

model.param.set('xexp3', '0.9894');

model.param.set('xexp4', '0.9923');

model.param.set('xexp5', '0.9951');

model.modelNode.create('mod1');

model.geom.create('geom1', 2);

model.geom('geom1').axisymmetric(true);

model.geom('geom1').lengthUnit('mm');

model.geom('geom1').feature.create('r1', 'Rectangle');

model.geom('geom1').feature.create('r2', 'Rectangle');

model.geom('geom1').feature.create('c1', 'Circle');

model.geom('geom1').feature.create('c2', 'Circle');

model.geom('geom1').feature.create('uni1', 'Union');

model.geom('geom1').feature.create('r3', 'Rectangle');

model.geom('geom1').feature.create('int1', 'Intersection');

model.geom('geom1').feature('r1').set('size', {'0.25' '127.1'});

model.geom('geom1').feature('r2').set('pos', {'0' '4.15+0.2466'});

model.geom('geom1').feature('r2').set('size', {'0.2466' '118.8-(0.2466*2)'});

model.geom('geom1').feature('c1').set('pos', {'0' '0.2466+4.15'});

model.geom('geom1').feature('c1').set('r', '0.2466');

model.geom('geom1').feature('c2').set('pos', {'0' '4.15+118.8-0.2466'});

model.geom('geom1').feature('c2').set('r', '0.2466');
```

```
model.geom('geom1').feature('uni1').set('intbnd', false);

model.geom('geom1').feature('uni1').set('edge', 'all');

model.geom('geom1').feature('uni1').selection('input').set({'c1' 'c2' 'r2'});

model.geom('geom1').feature('r3').set('pos', {'0' '0'});

model.geom('geom1').feature('r3').set('size', {'0.30' '200'});

model.geom('geom1').feature('int1').set('intbnd', false);

model.geom('geom1').feature('int1').set('edge', 'all');

model.geom('geom1').feature('int1').selection('input').set({'r3' 'uni1'});

model.geom('geom1').run;

model.selection.create('spf_dst_pfc1', 'Explicit');

model.selection.create('chds2_dst_pc1', 'Explicit');

model.selection('spf_dst_pfc1').name('Selection 1');

model.selection('chds2_dst_pc1').name('Selection 1a');

model.variable.create('var1');

model.variable('var1').set('rho_fattyacid', '(1000*(0.90941-(6.9820e-4)*(Tsys-273)))/(1-((3447378.5-101352.9)/(10^9)))
[K/kg*m^3]', 'Oleic acid density, kg/m3');

model.variable('var1').set('visc_fattyacid', 'rho_fattyacid*(10^-6)*(exp(-22.540759+(5635.462033/Tsys)+(0.023952*Tsys)))',
'Oleic acid viscosity, Pa s');

model.variable('var1').set('mol_H2_in', 'Pg/Rg/Tsys', 'initial concentration of hydrogen in gas phase, mol/m3 300 c 35 atm');

model.variable('var1').set('D_H2_g', '6.78673e-9*(Tsys^1.75)/Pg', 'F-S-G  H2 diffusivity, m2/s');

model.variable('var1').set('D_H2O_g', '6.78673e-9*(Tsys^1.75)/Pg');

model.variable('var1').set('D_H2_l', '(1.87848E-11)*Tsys/(visc_liq/(10^-3))', 'Wilke-chang, H2 diffusivity in oil, m2/s');

model.variable('var1').set('D_hydrocarbon', '(1.38*(10^-13))*Tsys/(6*3.1416)/visc_liq/(5.949/2)', 'Stoke-Einstein, R =5.949/2 A');

model.variable('var1').set('D_H2O_l', '(1.38*(10^-13))*Tsys/(6*3.1416)/visc_liq/(2.641/2)', 'Stoke-Einstein, R =2.641/2 A');

model.variable('var1').set('D_fattyacid', '(1.38*(10^-13))*Tsys/(6*3.1416)/visc_liq/(5.949/2)', 'assume = alkane');

model.variable('var1').set('D_intermediate', '(1.38*(10^-13))*Tsys/(6*3.1416)/visc_liq/(5.949/2)');

model.variable('var1').set('K_H2', '(-1.342+(0.012*Tsys))*(10^-2)*(0.10325)*1000', 'Herry"s law constant with varies T ,
Andersson 1974, mol/m3 atm');

model.variable('var1').set('mol_H2_interface', 'K_H2*Pg', 'Equilibrium hydrogen concentration at liquid interface, mol/m3');

model.variable('var1').set('factor1', '(500e-6) [m] /4');
```

```
model.variable('var1').set('mol_fattyacid_in', '88.5');

model.variable('var1').set('c_FFA', 'mod1.aveop1(c_fattyacid)');

model.variable('var1').set('c_FA', 'mod1.aveop1(c_fattyalcohol)');

model.variable('var1').set('c_ET', 'mod1.aveop1(c_ester)');

model.variable('var1').set('c_C18HC', 'mod1.aveop1(c_C18hydrocarbon)');

model.variable('var1').set('c_C17HC', 'mod1.aveop1(c_C17hydrocarbon)');

model.variable('var1').set('c_H2_L', 'mod1.aveop1(c_H2_l)');

model.variable('var1').set('c_H2O', 'mod1.aveop1(c_H2O_l)');

model.variable('var1').set('c_CO_L', 'mod1.aveop1(c_CO_l)');

model.variable('var1').set('c_CO2_L', 'mod1.aveop1(c_CO2_l)');

model.variable('var1').set('X', '(mol_fattyacid_in-c_FFA)/mol_fattyacid_in');

model.variable('var1').set('c_TOTAL', 'c_FFA+c_FA+c_ET+c_C18HC+c_C17HC');

model.variable('var1').set('m_FFA', 'c_FFA/c_TOTAL');

model.variable('var1').set('m_FA', 'c_FA/c_TOTAL');

model.variable('var1').set('m_ET', 'c_ET/c_TOTAL');

model.variable('var1').set('m_C18HC', 'c_C18HC/c_TOTAL');

model.variable('var1').set('m_C17HC', 'c_C17HC/c_TOTAL');

model.variable('var1').set('AA', 'wtfrac*rho_fattyacid/mw_FFA');

model.variable.create('var2');

model.variable('var2').model('mod1');

model.variable('var2').set('r4', 'k4*factor1*max(eps^2,c_fattyacid)');

model.variable('var2').set('r5', 'k5*factor1*max(eps^2,c_fattyalcohol)');

model.variable('var2').set('r6', 'k6*factor1*max(eps^2,c_fattyacid)');

model.variable('var2').set('r7', 'k7*factor1*max(eps^2,c_fattyacid)');

model.variable('var2').set('r8', '(k8*factor1*max(eps^2,c_fattyacid)*max(eps^2,c_fattyalcohol))-
(k9*factor1*max(eps^2,c_ester)*max(eps^2,c_H2O_l))');

model.variable('var2').selection.geom('geom1', 2);

model.variable('var2').selection.set([1]);

model.view.create('view2', 2);
```

```
model.view.create('view3', 3);

model.view.create('view4', 3);

model.material.create('mat1');

model.material('mat1').propertyGroup('def').func.create('eta', 'Piecewise');

model.material('mat1').propertyGroup('def').func.create('Cp', 'Piecewise');

model.material('mat1').propertyGroup('def').func.create('rho', 'Analytic');

model.material('mat1').propertyGroup('def').func.create('k', 'Piecewise');

model.physics.create('spf', 'LaminarFlow', 'geom1');

model.physics('spf').selection.set([1]);

model.physics('spf').feature.create('wall2', 'Wall', 1);

model.physics('spf').feature('wall2').selection.set([9]);

model.physics('spf').feature.create('pfc1', 'PeriodicFlowCondition', 1);

model.physics('spf').feature('pfc1').selection.set([2 7]);

model.physics('spf').feature('pfc1').feature.create('dd1', 'DestinationDomains', 1);

model.physics('spf').feature('pfc1').feature('dd1').selection.set([2]);

model.physics.create('chds', 'DilutedSpecies', 'geom1');

model.physics('chds').selection.set([2]);

model.physics('chds').feature.create('flux1', 'Flux', 1);

model.physics('chds').feature('flux1').selection.set([8 10 11]);

model.physics.create('chds2', 'DilutedSpecies', 'geom1');

model.physics('chds2').selection.set([1]);

model.physics('chds2').feature.create('flux1', 'Flux', 1);

model.physics('chds2').feature('flux1').selection.set([9]);

model.physics('chds2').feature.create('pc1', 'PeriodicCondition', 1);

model.physics('chds2').feature('pc1').selection.set([2 7]);

model.physics('chds2').feature('pc1').feature.create('dd1', 'DestinationDomains', 1);

model.physics('chds2').feature('pc1').feature('dd1').selection.set([2]);

model.physics('chds2').feature.create('flux2', 'Flux', 1);
```

```
model.physics('chds2').feature('flux2').selection.set([8 10 11]);

model.mesh.create('mesh1', 'geom1');

model.mesh('mesh1').feature.create('ftri1', 'FreeTri');

model.mesh('mesh1').feature('ftri1').selection.geom('geom1', 2);

model.mesh('mesh1').feature('ftri1').selection.set([1]);

model.mesh('mesh1').feature('ftri1').feature.create('size1', 'Size');

model.mesh('mesh1').feature.create('ftri3', 'FreeTri');

model.mesh('mesh1').feature('ftri3').selection.geom('geom1', 2);

model.mesh('mesh1').feature('ftri3').selection.set([2]);

model.mesh('mesh1').feature('ftri3').feature.create('size1', 'Size');

model.cpl.create('aveop1', 'Average', 'geom1');

model.cpl('aveop1').selection.set([1]);

model.result.table.create('tbl1', 'Table');

model.result.table.create('evl2', 'Table');

model.result.table.create('tbl2', 'Table');

model.variable('var1').name('Variables 1a');


model.view('view1').set('showlabels', true);

model.view('view1').axis.set('xmin', '-2.032799243927002');

model.view('view1').axis.set('xmax', '2.733503818511963');

model.view('view1').axis.set('ymin', '2.6722283363342285');

model.view('view1').axis.set('ymax', '10.207192420959473');

model.view('view1').axis.set('xextra', {});

model.view('view1').axis.set('yextra', {});

model.view('view2').set('showlabels', true);

model.view('view2').axis.set('xmin', '-1.4190696477890015');

model.view('view2').axis.set('xmax', '1.586586833000183');

model.view('view2').axis.set('ymin', '2.326307773590088');
```

```
model.view('view2').axis.set('ymax', '5.271549224853516');

model.view('view2').axis.set('xextra', {});

model.view('view2').axis.set('yextra', {});

model.material('mat1').name('Hydrogen');

model.material('mat1').propertyGroup('def').func('eta').set('arg', 'T');

model.material('mat1').propertyGroup('def').func('eta').set('pieces', {'200.0' '1300.0' '2.14524642E-6+2.54245E-8*T^1-
1.0235587E-11*T^2+2.80895021E-15*T^3'});

model.material('mat1').propertyGroup('def').func('Cp').set('arg', 'T');

model.material('mat1').propertyGroup('def').func('Cp').set('pieces', {'200.0' '1300.0' '10808.501+21.5799904*T^1-
0.0444720318*T^2+3.85401176E-5*T^3-1.14979447E-8*T^4'});

model.material('mat1').propertyGroup('def').func('rho').set('expr', 'pA*0.002016/8.314/T');

model.material('mat1').propertyGroup('def').func('rho').set('args', {'pA' 'T'});

model.material('mat1').propertyGroup('def').func('rho').set('dermethod', 'manual');

model.material('mat1').propertyGroup('def').func('rho').set('argders', {'pA' 'd(pA*0.002016/8.314/T,pA)'; 'T'
'd(pA*0.002016/8.314/T,T)'});

model.material('mat1').propertyGroup('def').func('rho').set('plotargs', {'pA' '' ''; 'T' '' ''});

model.material('mat1').propertyGroup('def').func('k').set('arg', 'T');

model.material('mat1').propertyGroup('def').func('k').set('pieces', {'200.0' '1300.0' '0.00517975922+6.72778E-4*T^1-3.0388973E-
7*T^2+6.58874687E-11*T^3'});

model.material('mat1').propertyGroup('def').set('dynamicviscosity', 'eta(T[1/K])[Pa*s]');

model.material('mat1').propertyGroup('def').set('ratioofspecificheat', '1.41');

model.material('mat1').propertyGroup('def').set('heatcapacity', 'Cp(T[1/K])[J/(kg*K)]');

model.material('mat1').propertyGroup('def').set('density', 'rho(pA[1/Pa],T[1/K])[kg/m^3]');

model.material('mat1').propertyGroup('def').set('thermalconductivity', {'k(T[1/K])[W/(m*K)]' '0' '0' '0' 'k(T[1/K])[W/(m*K)]' '0' '0'
'0' 'k(T[1/K])[W/(m*K)]'});

model.material('mat1').propertyGroup('def').addInput('temperature');

model.material('mat1').propertyGroup('def').addInput('pressure');

model.physics('spf').prop('Stabilization').set('ck', '0.5');

model.physics('spf').prop('TurbulenceProperty').set('kappav', '0.42');

model.physics('spf').feature('fp1').set('rho_mat', 'userdef');

model.physics('spf').feature('fp1').set('rho', 'rho_liq');
```

```
model.physics('spf').feature('fp1').set('mu_mat', 'userdef');

model.physics('spf').feature('fp1').set('mu', 'visc_liq');

model.physics('spf').feature('fp1').set('minput_pressure_src', 'userdef');

model.physics('spf').feature('wall1').set('BoundaryCondition', 'Slip');

model.physics('spf').feature('init1').set('u', {'0'; '0'; 'u0'});

model.physics('spf').feature('init1').set('p', '101325*Pg');

model.physics('spf').feature('wall2').set('BoundaryCondition', 'MovingWall');

model.physics('spf').feature('wall2').set('uwall', {'0'; '0'; '-ub'});

model.physics('chds').field('concentration').component({'c_H2_g' 'c_H2O_g' 'c_C3H8_g' 'c_CO_g' 'c_CO2_g'});

model.physics('chds').prop('Convection').set('Convection', '0');

model.physics('chds').feature('cdm1').set('um', {'1e-13'; '1e-13'; '1e-13'; '1e-13[s*mol/kg]'; '1e-13[s*mol/kg]'});

model.physics('chds').feature('cdm1').set('minput_concentration_src', 'root.mod1.c_C3H8_g');

model.physics('chds').feature('cdm1').set('D_0', {'D_H2_g'; '0'; '0'; '0'; 'D_H2_g'; '0'; '0'; '0'; 'D_H2_g'});

model.physics('chds').feature('cdm1').set('D_1', {'D_H2_g'; '0'; '0'; '0'; 'D_H2_g'; '0'; '0'; '0'; 'D_H2_g'});

model.physics('chds').feature('cdm1').set('D_2', {'D_H2_g'; '0'; '0'; '0'; 'D_H2_g'; '0'; '0'; '0'; 'D_H2_g'});

model.physics('chds').feature('cdm1').set('D_3', {'D_H2_g'; '0'; '0'; '0'; 'D_H2_g'; '0'; '0'; '0'; 'D_H2_g'});

model.physics('chds').feature('cdm1').set('D_4', {'D_H2_g'; '0'; '0'; '0'; 'D_H2_g'; '0'; '0'; '0'; 'D_H2_g'});

model.physics('chds').feature('init1').set('c_H2_g', 'mol_H2_in');

model.physics('chds').feature('flux1').set('species', {'1'; '1'; '1'; '1'; '1'});

model.physics('chds').feature('flux1').set('N0', {'-M*(c_H2_g-(c_H2_l/K_H2/Rg/Tsys))'; '-M*(c_H2O_g-
(c_H2O_l/K_H2/Rg/Tsys))'; '-M*(c_C3H8_g-(c_C3H8_l/K_H2/Rg/Tsys))'; '-M*(c_CO_g-(c_CO_l/K_H2/Rg/Tsys))'; '-
M*(c_CO2_g-(c_CO2_l/K_H2/Rg/Tsys))'});

model.physics('chds2').field('concentration').component({'c_fattyacid' 'c_fattyalcohol' 'c_C18hydrocarbon' 'c_H2O_l' 'c_H2_l'
'c_ester' 'c_TG' 'c_C3H8_l' 'c_C17hydrocarbon' 'c_CO_l' 'c_CO2_l'});

model.physics('chds2').feature('cdm1').set('u_src', 'root.mod1.u');

model.physics('chds2').feature('cdm1').set('um', {'1e-13'; '1e-13'; '1e-13'; '1e-13'; '1e-13'; '1e-13'; '1e-13'; '1e-13'; '1e-
13[s*mol/kg]'; '1e-13[s*mol/kg]'; '1e-13[s*mol/kg]'});

model.physics('chds2').feature('cdm1').set('D_0', {'D_fattyacid'; '0'; '0'; '0'; 'D_fattyacid'; '0'; '0'; '0'; 'D_fattyacid'});

model.physics('chds2').feature('cdm1').set('D_1', {'D_intermediate'; '0'; '0'; '0'; 'D_intermediate'; '0'; '0'; '0'; 'D_intermediate'});

model.physics('chds2').feature('cdm1').set('D_2', {'D_hydrocarbon'; '0'; '0'; '0'; 'D_hydrocarbon'; '0'; '0'; '0'; 'D_hydrocarbon'});

model.physics('chds2').feature('cdm1').set('D_3', {'D_H2O_l'; '0'; '0'; '0'; 'D_H2O_l'; '0'; '0'; '0'; 'D_H2O_l'});
```

```
model.physics('chds2').feature('cdm1').set('D_4', {'D_H2_l'; '0'; '0'; '0'; 'D_H2_l'; '0'; '0'; '0'; 'D_H2_l'});

model.physics('chds2').feature('cdm1').set('D_5', {'D_intermediate'; '0'; '0'; '0'; 'D_intermediate'; '0'; '0'; '0'; 'D_intermediate'});

model.physics('chds2').feature('cdm1').set('D_6', {'D_fattyacid'; '0'; '0'; '0'; 'D_fattyacid'; '0'; '0'; '0'; 'D_fattyacid'});

model.physics('chds2').feature('cdm1').set('D_7', {'D_H2_l'; '0'; '0'; '0'; 'D_H2_l'; '0'; '0'; '0'; 'D_H2_l'});

model.physics('chds2').feature('cdm1').set('D_8', {'D_hydrocarbon'; '0'; '0'; '0'; 'D_hydrocarbon'; '0'; '0'; '0'; 'D_hydrocarbon'});

model.physics('chds2').feature('cdm1').set('D_9', {'D_H2_l'; '0'; '0'; '0'; 'D_H2_l'; '0'; '0'; '0'; 'D_H2_l'});

model.physics('chds2').feature('cdm1').set('D_10', {'D_H2_l'; '0'; '0'; '0'; 'D_H2_l'; '0'; '0'; '0'; 'D_H2_l'});

model.physics('chds2').feature('init1').set('c_fattyacid', 'mol_fattyacid_in');

model.physics('chds2').feature('flux1').set('species', {'1'; '1'; '1'; '1'; '1'; '1'; '0'; '0'; '1'; '1'; '1'});

model.physics('chds2').feature('flux1').set('N0', {'-r4-r6-r7-r8'; 'r4-r5-r8'; 'r5'; 'r4+r5+r7+r8'; '-(2*r4)-r5-r7'; 'r8'; '-rxn2'; 'rxn2';
'r6+r7'; 'r7'; 'r6'});

model.physics('chds2').feature('flux2').set('species', {'0'; '0'; '0'; '1'; '1'; '0'; '0'; '1'; '0'; '1'; '1'});

model.physics('chds2').feature('flux2').set('N0', {'0'; '0'; '0'; '-M*((c_H2O_l/K_H2/Rg/Tsys)-c_H2O_g)'; '-
M*((c_H2_l/K_H2/Rg/Tsys)-c_H2_g)'; '0'; '0'; '-M*((c_C3H8_l/K_H2/Rg/Tsys)-c_C3H8_g)'; '0'; '-M*((c_CO_l/K_H2/Rg/Tsys)-
c_CO_g)'; '-M*((c_CO2_l/K_H2/Rg/Tsys)-c_CO2_g)'});

model.mesh('mesh1').feature('size').set('hauto', 9);

model.mesh('mesh1').feature('ftri1').feature('size1').set('table', 'cfd');

model.mesh('mesh1').feature('ftri1').feature('size1').set('hauto', 2);

model.mesh('mesh1').feature('ftri3').feature('size1').set('table', 'cfd');

model.mesh('mesh1').feature('ftri3').feature('size1').set('hauto', 9);

model.mesh('mesh1').run;

model.result.table('tbl1').comments('Surface Integration 1 (c_H2_l)');

model.result.table('evl2').name('Evaluation 2D');

model.result.table('evl2').comments('Interactive 2D values');

model.result.table('tbl2').name('Table 2');

model.result.table('tbl2').comments('Surface Integration 1 (c_fattyacid)');

model.study.create('std3');

model.study('std3').feature.create('stat', 'Stationary');

model.study('std3').feature.create('time', 'Transient');

model.sol.create('sol1');
```

```
model.sol('sol1').study('std3');

model.sol('sol1').attach('std3');

model.sol('sol1').feature.create('st1', 'StudyStep');

model.sol('sol1').feature.create('v1', 'Variables');

model.sol('sol1').feature.create('s1', 'Stationary');

model.sol('sol1').feature('s1').feature.create('fc1', 'FullyCoupled');

model.sol('sol1').feature('s1').feature.create('d1', 'Direct');

model.sol('sol1').feature('s1').feature.remove('fcDef');

model.sol('sol1').feature.create('su1', 'StoreSolution');

model.sol('sol1').feature.create('st2', 'StudyStep');

model.sol('sol1').feature.create('v2', 'Variables');

model.sol('sol1').feature.create('t1', 'Time');

model.sol('sol1').feature('t1').feature.create('fc1', 'FullyCoupled');

model.sol('sol1').feature('t1').feature.create('d1', 'Direct');

model.sol('sol1').feature('t1').feature.remove('fcDef');

model.result.dataset.create('rev1', 'Revolve2D');

model.result.dataset.remove('dset3');

model.result.create('pg1', 'PlotGroup2D');

model.result('pg1').feature.create('surf1', 'Surface');

model.result.create('pg4', 'PlotGroup2D');

model.result('pg4').feature.create('surf1', 'Surface');

model.result.create('pg6', 'PlotGroup2D');

model.result('pg6').feature.create('surf1', 'Surface');

model.result.create('pg7', 'PlotGroup1D');

model.result('pg7').set('probetag', 'none');

model.result('pg7').feature.create('glob1', 'Global');

model.result.create('pg8', 'PlotGroup1D');

model.result('pg8').set('probetag', 'none');
```

```
model.result('pg8').feature.create('glob1', 'Global');

model.result.create('pg9', 'PlotGroup1D');

model.result('pg9').set('probetag', 'none');

model.result('pg9').feature.create('glob1', 'Global');

model.result.export.create('plot1', 'Plot');

model.study('std3').name('Study 1');

model.study('std3').feature('stat').set('activate', {'spf' 'on' 'chds' 'off' 'chds2' 'off'});

model.study('std3').feature('time').set('activate', {'spf' 'off' 'chds' 'on' 'chds2' 'on'});

model.study('std3').feature('time').set('tlist', 'range(0,1,37)');

model.sol('sol1').feature('st1').name('Compile Equations: Stationary');

model.sol('sol1').feature('st1').set('studystep', 'stat');

model.sol('sol1').feature('v1').feature('mod1_c_H2_g').set('solvefor', false);

model.sol('sol1').feature('v1').feature('mod1_c_fattyalcohol').set('solvefor', false);

model.sol('sol1').feature('v1').feature('mod1_c_fattyacid').set('solvefor', false);

model.sol('sol1').feature('v1').feature('mod1_c_ester').set('solvefor', false);

model.sol('sol1').feature('v1').feature('mod1_c_H2O_g').set('solvefor', false);

model.sol('sol1').feature('v1').feature('mod1_c_C3H8_g').set('solvefor', false);

model.sol('sol1').feature('v1').feature('mod1_c_C18hydrocarbon').set('solvefor', false);

model.sol('sol1').feature('v1').feature('mod1_c_C18hydrocarbon').set('variables', 'mod1_c_hydrocarbon');

model.sol('sol1').feature('v1').feature('mod1_c_TG').set('solvefor', false);

model.sol('sol1').feature('v1').feature('mod1_c_H2_l').set('solvefor', false);

model.sol('sol1').feature('v1').feature('mod1_c_H2O_l').set('solvefor', false);

model.sol('sol1').feature('v1').feature('mod1_c_C3H8_l').set('solvefor', false);

model.sol('sol1').feature('v1').feature('mod1_c_C17hydrocarbon').set('solvefor', false);

model.sol('sol1').feature('v1').feature('mod1_c_C17hydrocarbon').set('variables', 'mod1_c_fattyacid9');

model.sol('sol1').feature('v1').feature('mod1_c_CO_l').set('solvefor', false);

model.sol('sol1').feature('v1').feature('mod1_c_CO_l').set('variables', 'mod1_c_fattyacid10');

model.sol('sol1').feature('v1').feature('mod1_c_CO_g').set('solvefor', false);
```

```
model.sol('sol1').feature('v1').feature('mod1_c_CO_g').set('variables', 'mod1_c_H2_g4');

model.sol('sol1').feature('v1').feature('mod1_c_CO2_g').set('solvefor', false);

model.sol('sol1').feature('v1').feature('mod1_c_CO2_g').set('variables', 'mod1_c_H2_g5');

model.sol('sol1').feature('v1').feature('mod1_c_CO2_l').set('solvefor', false);

model.sol('sol1').feature('v1').feature('mod1_c_CO2_l').set('variables', 'mod1_c_fattyacid11');

model.sol('sol1').feature('s1').set('control', 'stat');

model.sol('sol1').feature('s1').feature('fc1').set('initstep', '0.01');

model.sol('sol1').feature('s1').feature('fc1').set('minstep', '1.0E-6');

model.sol('sol1').feature('s1').feature('d1').set('linsolver', 'pardiso');

model.sol('sol1').feature('su1').name('Store Solution 2');

model.sol('sol1').feature('su1').set('sol', 'sol2');

model.sol('sol1').feature('st2').name('Compile Equations: Time Dependent (2)');

model.sol('sol1').feature('st2').set('studystep', 'time');

model.sol('sol1').feature('v2').set('initmethod', 'sol');

model.sol('sol1').feature('v2').set('initsol', 'sol1');

model.sol('sol1').feature('v2').set('notsolmethod', 'sol');

model.sol('sol1').feature('v2').set('notsol', 'sol1');

model.sol('sol1').feature('v2').feature('mod1_u').set('solvefor', false);

model.sol('sol1').feature('v2').feature('mod1_p').set('solvefor', false);

model.sol('sol1').feature('v2').feature('mod1_c_C18hydrocarbon').set('variables', 'mod1_c_hydrocarbon');

model.sol('sol1').feature('v2').feature('mod1_c_C17hydrocarbon').set('variables', 'mod1_c_fattyacid9');

model.sol('sol1').feature('v2').feature('mod1_c_CO_l').set('variables', 'mod1_c_fattyacid10');

model.sol('sol1').feature('v2').feature('mod1_c_CO_g').set('variables', 'mod1_c_H2_g4');

model.sol('sol1').feature('v2').feature('mod1_c_CO2_g').set('variables', 'mod1_c_H2_g5');

model.sol('sol1').feature('v2').feature('mod1_c_CO2_l').set('variables', 'mod1_c_fattyacid11');

model.sol('sol1').feature('t1').set('control', 'time');

model.sol('sol1').feature('t1').set('tlist', 'range(0,1,37)');

model.sol('sol1').feature('t1').set('atolmethod', {'mod1_u' 'global' 'mod1_p' 'global' 'mod1_c_H2_g' 'global' 'mod1_c_fattyalcohol'
'global' 'mod1_c_fattyacid' 'global' 'mod1_c_ester' 'global' 'mod1_c_H2O_g' 'global' 'mod1_c_C3H8_g' 'global'
```

```
'mod1_c_C18hydrocarbon' 'global' 'mod1_c_TG' 'global' 'mod1_c_H2_l' 'global' 'mod1_c_H2O_l' 'global' 'mod1_c_C3H8_l'
'global' 'mod1_c_C17hydrocarbon' 'global' 'mod1_c_CO_l' 'global' 'mod1_c_CO_g' 'global' 'mod1_c_CO2_g' 'global'
'mod1_c_CO2_l' 'global'});

model.sol('sol1').feature('t1').set('atol', {'mod1_u' '1e-3' 'mod1_p' '1e-3' 'mod1_c_H2_g' '1e-3' 'mod1_c_fattyalcohol' '1e-3'
'mod1_c_fattyacid' '1e-3' 'mod1_c_ester' '1e-3' 'mod1_c_H2O_g' '1e-3' 'mod1_c_C3H8_g' '1e-3' 'mod1_c_C18hydrocarbon' '1e-3'
'mod1_c_TG' '1e-3' 'mod1_c_H2_l' '1e-3' 'mod1_c_H2O_l' '1e-3' 'mod1_c_C3H8_l' '1e-3' 'mod1_c_C17hydrocarbon' '1e-3'
'mod1_c_CO_l' '1e-3' 'mod1_c_CO_g' '1e-3' 'mod1_c_CO2_g' '1e-3' 'mod1_c_CO2_l' '1e-3'});

model.sol('sol1').feature('t1').set('atoludot', {'mod1_u' '1e-3' 'mod1_p' '1e-3' 'mod1_c_H2_g' '1e-3' 'mod1_c_fattyalcohol' '1e-3'
'mod1_c_fattyacid' '1e-3' 'mod1_c_ester' '1e-3' 'mod1_c_H2O_g' '1e-3' 'mod1_c_C3H8_g' '1e-3' 'mod1_c_C18hydrocarbon' '1e-3'
'mod1_c_TG' '1e-3' 'mod1_c_H2_l' '1e-3' 'mod1_c_H2O_l' '1e-3' 'mod1_c_C3H8_l' '1e-3' 'mod1_c_C17hydrocarbon' '1e-3'
'mod1_c_CO_l' '1e-3' 'mod1_c_CO_g' '1e-3' 'mod1_c_CO2_g' '1e-3' 'mod1_c_CO2_l' '1e-3'});

model.sol('sol1').feature('t1').set('atoludotactive', {'mod1_u' 'off' 'mod1_p' 'off' 'mod1_c_H2_g' 'off' 'mod1_c_fattyalcohol' 'off'
'mod1_c_fattyacid' 'off' 'mod1_c_ester' 'off' 'mod1_c_H2O_g' 'off' 'mod1_c_C3H8_g' 'off' 'mod1_c_C18hydrocarbon' 'off'
'mod1_c_TG' 'off' 'mod1_c_H2_l' 'off' 'mod1_c_H2O_l' 'off' 'mod1_c_C3H8_l' 'off' 'mod1_c_C17hydrocarbon' 'off'
'mod1_c_CO_l' 'off' 'mod1_c_CO_g' 'off' 'mod1_c_CO2_g' 'off' 'mod1_c_CO2_l' 'off'});

model.sol('sol1').feature('t1').set('maxorder', '2');

model.sol('sol1').feature('t1').feature('fc1').set('maxiter', '5');

model.sol('sol1').feature('t1').feature('fc1').set('jtech', 'once');

model.sol('sol1').feature('t1').feature('d1').set('linsolver', 'pardiso');

model.sol('sol1').runAll;

model.result.dataset('rev1').set('startangle', '-90');

model.result.dataset('rev1').set('revangle', '225');

model.result('pg1').name('Velocity (spf)');

model.result('pg1').set('title', 'Time=37 Surface: Velocity magnitude (m/s) ');

model.result('pg1').set('frametype', 'spatial');

model.result('pg1').set('titleactive', false);

model.result('pg4').name('Concentration (chds)');

model.result('pg4').set('title', 'Time=37 Surface: Concentration (mol/m<sup>3</sup>) ');

model.result('pg4').set('titleactive', false);

model.result('pg4').feature('surf1').set('expr', 'c_H2_g');

model.result('pg4').feature('surf1').set('unit', 'mol/m^3');

model.result('pg4').feature('surf1').set('descr', 'Concentration');

model.result('pg6').name('Concentration (chds2)');

model.result('pg6').set('title', 'Time=37 Surface:  (1) ');

model.result('pg6').set('titleactive', false);
```

```
model.result('pg6').feature('surf1').set('expr', 'm_C18HC');

model.result('pg6').feature('surf1').set('unit', '1');

model.result('pg6').feature('surf1').set('descr', '');

model.result('pg6').feature('surf1').set('colortablerev', true);

model.result('pg7').name('Conversion');

model.result('pg7').set('titleactive', true);

model.result('pg7').set('xlabel', 'Time (s)');

model.result('pg7').set('xlabelactive', true);

model.result('pg7').set('ylabel', 'Conversion');

model.result('pg7').set('ylabelactive', true);

model.result('pg7').set('legendpos', 'upperleft');

model.result('pg7').feature('glob1').set('expr', {'X'});

model.result('pg7').feature('glob1').set('unit', {''});

model.result('pg7').feature('glob1').set('descr', {''});

model.result('pg7').feature('glob1').set('legendmethod', 'manual');

model.result('pg7').feature('glob1').set('legends', {'conversion'});

model.result('pg8').name('Concentration');

model.result('pg8').set('title', ' ');

model.result('pg8').set('titleactive', true);

model.result('pg8').set('xlabel', 'Time (s)');

model.result('pg8').set('xlabelactive', true);

model.result('pg8').set('ylabel', 'Concentration (mol/m3)');

model.result('pg8').set('ylabelactive', true);

model.result('pg8').set('legendpos', 'upperleft');

model.result('pg8').feature('glob1').set('expr', {'c_FFA' 'c_FA' 'c_ET' 'c_C18HC' 'c_H2_L' 'c_H2O' 'c_C17HC' 'c_CO_L'
'c_CO2_L'});

model.result('pg8').feature('glob1').set('unit', {'mol/m^3' 'mol/m^3' 'mol/m^3' 'mol/m^3' 'mol/m^3' 'mol/m^3' 'mol/m^3' 'mol/m^3'
'mol/m^3'});

model.result('pg8').feature('glob1').set('descr', {'' '' '' '' '' '' '' ''});
```

```
model.result('pg8').feature('glob1').set('xdata', 'expr');

model.result('pg8').feature('glob1').set('xdataexpr', 't');

model.result('pg8').feature('glob1').set('xdataunit', 's');

model.result('pg8').feature('glob1').set('xdatadescr', 'Time');

model.result('pg8').feature('glob1').set('legendmethod', 'manual');

model.result('pg8').feature('glob1').set('legends', {'FFA' 'FA' 'ET' 'C18HC' 'H2' 'H2O' 'C17HC' 'CO' 'CO2'});

model.result('pg9').name('Mole fraction');

model.result('pg9').set('title', ' ');

model.result('pg9').set('titleactive', true);

model.result('pg9').set('xlabel', 'Time (s)');

model.result('pg9').set('xlabelactive', true);

model.result('pg9').set('ylabel', 'Mole fraction');

model.result('pg9').set('ylabelactive', true);

model.result('pg9').set('legendpos', 'upperleft');

model.result('pg9').feature('glob1').set('expr', {'m_FFA' 'm_FA' 'm_ET' 'm_C18HC' 'm_C17HC'});

model.result('pg9').feature('glob1').set('unit', {'1' '1' '1' '1' '1'});

model.result('pg9').feature('glob1').set('descr', {'' '' '' '' ''});

model.result('pg9').feature('glob1').set('legendmethod', 'manual');

model.result('pg9').feature('glob1').set('legends', {'FFA' 'FA' 'ET' 'C18HC' 'C17HC'});

model.result.export('plot1').set('plotgroup', 'pg9');

model.result.export('plot1').set('plot', 'glob1');

model.result.export('plot1').set('filename', 'Z:\Windows.Documents\Desktop\P Tuk\tt.txt');

%Numerical data at point a, t=11s

M_FFA_a=mphglobal(model,'m_FFA','t',11);

M_FA_a=mphglobal(model,'m_FA','t',11);

M_ET_a=mphglobal(model,'m_ET','t',11);

M_C18HC_a=mphglobal(model,'m_C18HC','t',11);

M_C17HC_a=mphglobal(model,'m_C17HC','t',11);
```

```
%Numerical data at point b, t=26s

M_FFA_b=mphglobal(model,'m_FFA','t',26);

M_FA_b=mphglobal(model,'m_FA','t',26);

M_ET_b=mphglobal(model,'m_ET','t',26);

M_C18HC_b=mphglobal(model,'m_C18HC','t',26);

M_C17HC_b=mphglobal(model,'m_C17HC','t',26);

%Numerical data at point c, t=37s

M_FFA_c=mphglobal(model,'m_FFA','t',37);

M_FA_c=mphglobal(model,'m_FA','t',37);

M_ET_c=mphglobal(model,'m_ET','t',37);

M_C18HC_c=mphglobal(model,'m_C18HC','t',37);

M_C17HC_c=mphglobal(model,'m_C17HC','t',37);

%Experimetal data point a, t=11 s

MEXP_FFA_a=0.0340 ;

MEXP_FA_a=0.6427;

MEXP_ET_a=0.0583;

MEXP_C18HC_a=0.2254;

MEXP_C17HC_a=0.0396;

%Experimetal data point b, t=26 s

MEXP_FFA_b=0.0063 ;

MEXP_FA_b=0.4935;

MEXP_ET_b=0.0064;

MEXP_C18HC_b=0.4236;

MEXP_C17HC_b=0.0702;

%Experimetal data point c, t=37 s

MEXP_FFA_c=0.0126 ;

MEXP_FA_c=0.2240;

MEXP_ET_c=0.0055;
```

```
MEXP_C18HC_c=0.6259;

MEXP_C17HC_c=0.1320;


%objective function

f=((1*((M_FFA_a-MEXP_FFA_a)^2))+(1*((M_FA_a-MEXP_FA_a)^2))...
   +(1*((M_ET_a-MEXP_ET_a)^2))+(1*((M_C17HC_a-MEXP_C17HC_a)^2))...
   +(1*((M_C18HC_a-MEXP_C18HC_a)^2)))+((1*((M_FFA_b-MEXP_FFA_b)^2))...
   +(1*((M_FA_b-MEXP_FA_b)^2))+(1*((M_ET_b-MEXP_ET_b)^2))...
   +(1*((M_C17HC_b-MEXP_C17HC_b)^2))+(1*((M_C18HC_b-MEXP_C18HC_b)^2)))...
   +((1*((M_FFA_c-MEXP_FFA_c)^2))+(1*((M_FA_c-MEXP_FA_c)^2))...
   +(1*((M_ET_c-MEXP_ET_c)^2))+(1*((M_C17HC_c-MEXP_C17HC_c)^2))...
   +(1*((M_C18HC_c-MEXP_C18HC_c)^2)));
```

C3. Simplex search optimization of objective function for oleic acid hydrotreating

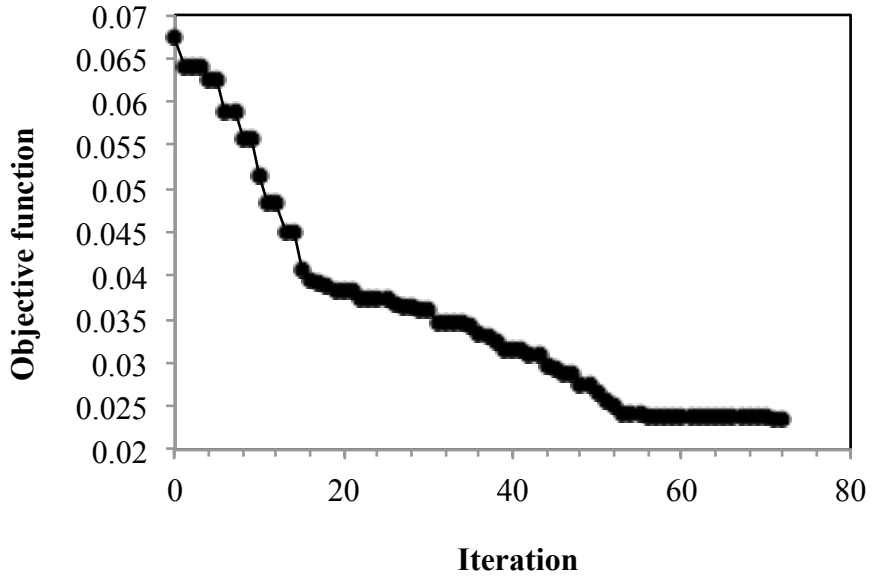

Figure C.1 Simplex search optimization of objective function for oleic acid hydrotreating at 325 °C.

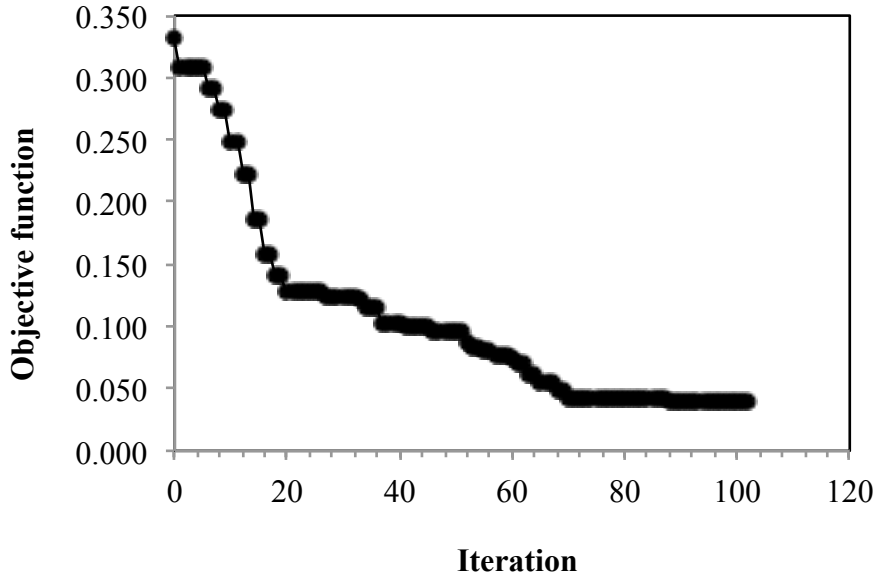

Figure C.2 Simplex search optimization of objective function for oleic acid hydrotreating at 300 °C.

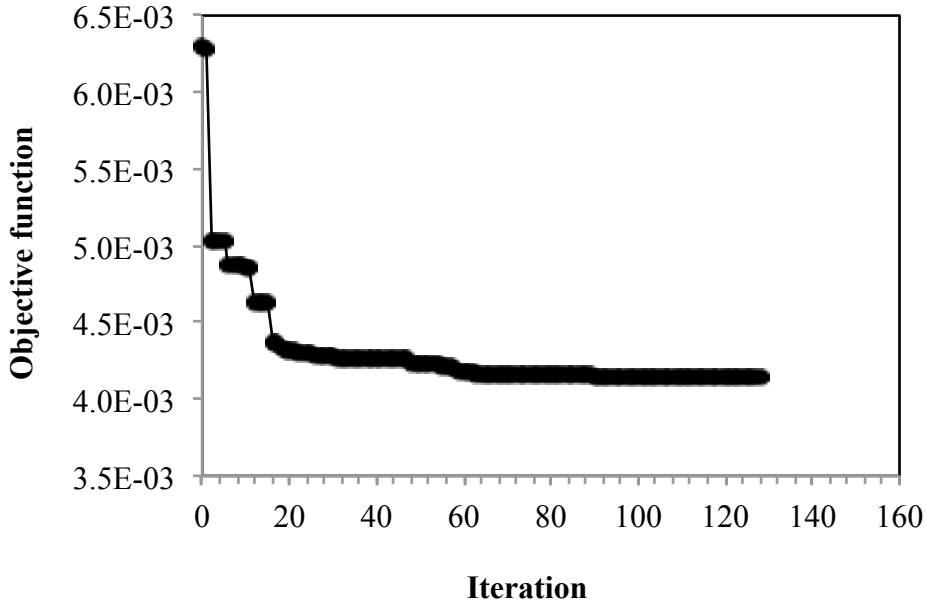

Figure C.3 Simplex search optimization of objective function for oleic acid hydrotreating at 275 °C.

Appendix D. Calculation

D1. Catalyst mass and catalyst surface area

Microtube Length (m)	Catalyst mass (mg)	Catalyst surface area/Reactor volume (m^2/m^3)
1.5	2.8	$1.6 * 10^6$
3.5	6.4	$1.6 * 10^6$
5	9	$1.6 * 10^6$

* Surface area = 200 m^2/g

D2. Carbon balance calculation

D2.1 Oleic acid hydrotreating at 275 ˚C, Time on stream = 2 h					
INPUT					
Oleic acid molar flow rate (mol/min)			0.000013		
mol C/min			0.000234		
OUTPUT					
Total liquid mass flow rate (g/min)			0.0729		
	C	mw (g/mol)	Component mass flow rate (g/min)	mol/min	mol C/min
Oleic acid	18	282.4600	0.001901907	6.73337E-06	1.2120E-04
Stearyl alcohol	18	270.4900	0.000211323	7.8126E-07	1.4063E-05
Octadecyl octadecanoate	36	536.9600	0.00102018	1.89992E-06	6.8397E-05
Octadecane	18	254.5000	0.000029148	1.1453E-07	2.0615E-06
Heptadecane	17	240.4700	0.000007287	3.03032E-08	5.1515E-07
Total				9.55938E-06	2.0624E-04
Carbon balance (%)					88.14
D2.2 Oleic acid hydrotreating at 275 ˚C, Time on stream = 4 h					
INPUT					
Oleic acid molar flow rate (mol/min)			0.000013		
mol C/min			0.000234		
OUTPUT					
Total liquid mass flow rate (g/min)			0.0749		
	C	mw (g/mol)	Component mass flow rate (g/min)	mol/min	mol C/min
Oleic acid	18	282.4600	0.00216461	7.66342E-06	1.3794E-04
Stearyl alcohol	18	270.4900	0.0002247	8.30715E-07	1.4953E-05
Octadecyl octadecanoate	36	536.9600	0.00083139	1.54833E-06	5.5740E-05
Octadecane	18	254.5000	0.00002996	1.17721E-07	2.1190E-06
Heptadecane	17	240.4700	0.00001498	6.22947E-08	1.0590E-06
Total				1.02225E-05	2.1181E-04
Carbon balance (%)					90.52